Robust Scheduling Control of Aeroelasticity

Zebb D. Prime

School of Mechanical Engineering
The University of Adelaide
South Australia 5005
Australia

Typeset by the author using LaTeX.
Printed in Australia.

Summary

Aeroelasticity is a broad term describing the often complex interactions between structural mechanics and aerodynamics. Aeroelastic phenomena such as divergence and flutter are potentially destructive, and thus must be avoided. Passive methods to avoid undesirable aeroelastic phenomena often involve the addition of mass and/or limiting the achievable performance of the aircraft. However, active control methods allow both for the suppression of undesirable aeroelastic phenomena, and for utilisation of desirable aeroelastic phenomena using actuators, thus increasing performance without the associated weight penalty of passive systems.

The work presented in this thesis involves the design, implementation and experimental validation of novel active controllers to suppress undesirable aeroelastic phenomena over a range of airspeeds. The controllers are constructed using a Linear Parameter Varying (LPV) framework, where the plant and controllers can be represented as linear systems which are functions of a parameter, in this case airspeed. The LPV controllers are constructed using Linear Matrix Inequalities (LMIs), which are convex optimisation problems that can be used to represent many linear control objectives. Using LMIs, these LPV controllers can be constructed such that they self-schedule with airspeed and provide upper performance bounds during the design process.

The aeroelastic phenomena being suppressed by these controllers are Limit-Cycle Oscillations (LCOs), which are a form of flutter with the aeroelastic instability bounded by a structural nonlinearity in the aeroelastic system. In this work, the aeroelastic system used is the Nonlinear Aeroelastic Test Apparatus (NATA), an experimental aeroelastic test platform located at Texas A&M University.

Three and four degree-of-freedom dynamic models were derived for the NATA, which include second-order servo motor dynamics. These

servo motor dynamics are often neglected in literature but are sufficiently slow that their dynamics are significant to the controlled response of the NATA. The dynamic model also incorporates quasi-steady aerodynamics, which are accurate for low Strouhal numbers calculated from the oscillation frequency of the wing. Is it shown how the dynamics of the NATA can be represented in LPV form, with a quadratic dependence on airspeed and linear dependence on torsional stiffness.

Using a variety of techniques the parameters of the NATA are identified, and shown through nonlinear simulation to provide excellent agreement with experimental results. It is also argued that structural nonlinearity, in the way of a nonlinear torsional spring connecting the wing section to the base, generally improves stability due to its largely quadratic stiffness function, and hence in many instances it is safe to linearise this nonlinearity when designing a controller.

Using a $\mathcal{H}_2$ generalised control problem representation of a Linear Quadratic Regulator (LQR) state-feedback controller, LPV synthesis LMIs are constructed using a standard transformation which render the LMIs affine in the transformed controller and Lyapunov matrices. These matrices have the same quadratic dependence on airspeed as the NATA model. To reduce conservatism the parameter space of airspeed versus airspeed squared is gridded into triangular convex hulls over the true parameter curve, and the LMIs are numerically optimised to give an upper bound on the $\mathcal{H}_2$ norm across the design airspeed. The resulting state-feedback controller is constructed from the transformed controller and Lyapunov matrices, and can be solved symbolically as a function of airspeed, however it forms a high-order rational function of airspeed, hence it is quicker to solve for the controller gains numerically on-line.

The controller is analysed for the classical measures of robustness, namely gain and phase margins, and maximum sensitivity. While not providing the guarantees of these measures that a conventional LQR controller provides, the controller is shown to be sufficiently robust across the airspeed design range.

Experimental results for this controller were performed, and the results show excellent LCO suppression and disturbance rejection, the results from which are published in Prime et al. (2010).

Following the above work based on a scalar performance index, the upper bound on the $\mathcal{H}_2$ norm is allowed to vary with airspeed using

the same quadratic dependence on airspeed as the NATA model, and the transformed controller and Lyapunov matrices. A simple method of solving the LMIs is shown such that the LPV $\mathcal{H}_2$ upper bound is as close to optimal as possible, and using this method a new controller is synthesised.

This new controller is compared against the LPV LQR controller with the scalar performance index, and is shown to be closer to optimal across the airspeed design range. Nonlinear simulations of the controlled NATA using this new controller are then presented.

Based on Prime et al. (2008), a Linear Fractional Transformation (LFT) is applied to the NATA model to render the dynamics dependent upon the feedback of the linear value of airspeed. This allows the LMIs to be constructed at only two points, the extreme values of the linear design airspeed, rather than gridding over the parameter space as was performed above.

An output-feedback controller that itself depends upon the feedback of a function that is linearly dependent upon airspeed is constructed using an induced $\mathcal{L}_2$ loop-shaping framework. The induced $\mathcal{L}_2$ performance objective is based upon a Glover-McFarlane $\mathcal{H}_\infty$ loop-shaping process where the NATA singular values are shaped using pre- and post-filters, and minimising the induced $\mathcal{L}_2$ norm from both the input and output to both the input and output.

An LFT controller is synthesised, and simulations are performed showing the suppression of LCOs.

Declarations

Originality

This work contains no material which has been accepted for the award of any other degree of diploma in any university or other tertiary institution. To the best of my knowledge and belief, this work contains no material previously published or written by another person, except where due reference has been made in the text.

Permissions

I give consent to this copy of my thesis, when deposited in the University Library, being made available for loan and photocopying, subject to the provisions of the Copyright Act 1968.

I also give permission for the digital version of my thesis to be made available on the web, via the University s digital research repository, the Library catalogue, the Australasian Digital Theses Program (ADTP) and also through web search engines, unless permission has been granted by the University to restrict access for a period of time.

Zebb D. Prime

Acknowledgements

First and foremost, I would like the thank my academic supervisors, Associate Professor Ben Cazzolato and Dr Con Doolan. Their support and encouragement has been invaluable in helping me reach this point. They have also been understanding of my side projects, such as my pet Matlab project, `matlabfrag`.

I would also like to extend my gratitude to Professor Thomas Strganac at Texas A&M University for his hospitality and support during my research visit to use the NATA. Furthermore, this research visit would not have been possible without the financial support from the Sir Ross & Sir Keith Smith Fund.

For all my friends, unfortunately I can t thank you individually, with the exception of my office mates over the years: Will Robertson, Rohin Wood, Dick Petersen, and Steve Harding. Will has been a constant source of typesetting and style knowledge, and has spent countless hours sel essly helping me with LaTeX, for which I am grateful. Rohin and Dick were both strong role-models for research, proving how much can be achieved in three years. Finally Steve has been a constant source of entertainment in the office.

During my study I have spent a lot of time living with my siblings, Joel, Rhiannon and Zoe. Thanks for putting up with me and my mess.

I would also like to thank my partner, Amanda Teague, for her support during this long and tedious journey.

Finally, I would like to thank my parents, David and Roxanne Prime, for the continued support during my education. Over the years they have provided continued encouragement, patience, financial support and a place I can always return to and call home.

Contents

List of Figures

List of Tables

1 Introduction

Throughout human aviation history, aeroelasticity, a term describing the interactions between structural mechanics and aerodynamics, has been a topic of primary interest. In fact, the Wright brother s Flyer, the first aircraft to achieve controlled, powered and sustainable ight, utilised aeroelasticity for roll control by warping a exible wing. Furthermore, it is thought that aeroelasticity may have played a role in the failure of Langley s ying machine a few weeks earlier by either divergence, when the static aerodynamic load causes structural failure, or possibly dynamic load failure (Mukhopadhyay 2003).

The most feared aeroelastic phenomena is utter. Flutter is a dynamic instability, which involves the oscillation of a body in an airstream causing the aerodynamic forces to feed back into the oscillation. Hence energy from the airstream is transferred into the oscillations, causing them to increase in amplitude. At its worst, utter oscillations will grow until catastrophic structural failure, but even if the oscillations are bounded the vibration can lead to ride discomfort and fatigue failure.

These aeroelastic phenomena are not just limited to aerospace applications, as they can be exhibited in any body in an airstream. For example, the failure of the first Tacoma Narrows suspension bridge in 1940 has been attributed to wind induced oscillations (Mukhopadhyay 2003).

For many years the traditional method for addressing aeroelasticity has been to design the airframe such that the destructive phenomena, such as utter and divergence, do not occur inside the ight envelope. This can be achieved through changing the stiffness or mass properties of the airframe, often adding to the overall mass of the airframe, or reducing the ight envelope, thus reducing performance. Through the use of active-control techniques, these phenomena can be suppressed or utilised, which can lead to a reduction in weight and an increase in performance.

1

As an example, and a throwback to the Wright brother s Flyer, the Active Aeroelastic Wing (AAW) research project is attempting to utilise the warping of aircraft wings for manoeuvring and increasing performance (Pendleton et al. 2000). The AAW modified F/A-18A aircraft is shown in Figure 1.1.

There has been much research into actively controlling aeroelasticity, and a historical summary of much of this work can be found in the article by Mukhopadhyay (2003). Over the years this research has progressed from classical control, through the modern control, robust control and nonlinear control design eras, such that a significant amount of the research published on aeroelasticity control over the last decade has been based on Lyapunov backstepping schemes. However, many of these backstepping based controllers exhibit high gain, which when used experimentally, especially in the presence of unmodelled dynamics, can lead to poor closed-loop performance and unreasonable actuator demands. These backstepping based controllers are also at odds with the way control theory is used in practical aerospace applications, which are often based on optimal control schemes, and are required to show high levels of robustness across the operating ranges.

The maturing of Linear Parameter Varying (LPV) control theory provides a bridge between the fields of nonlinear and practical aerospace control. LPV control involves the representation of a system as linear with respect to some varying parameter. The controller is then synthesised as a series of Linear Matrix Inequalities (LMIs), which are convex optimisation

Figure 1.1: Active Aeroelastic Wing modified F/A-18A. Image courtesy of NASA, www.nasaimages.org.

problems that can be easily solved. The benefit of LPV controllers is that they are able to provide a systematic method of designing scheduling controllers based on many of the mature linear control methodologies which are well accepted amongst control engineers in the aerospace industry, while also providing a performance or robustness guarantee across the design range.

A review of the recent Aeroelasticity control literature presented in Section 3.2.1 of this thesis shows that while there has been much research into nonlinear control of two degree-of-freedom aeroelasticity, there has been little research into scheduled aeroelasticity control with robustness and performance guarantees.

The motivation for this work is an intentionally exible wing system for use on a novel style of high-speed yacht (Bourn 2001, Bourn 2000). As the wing is highly exible, it requires active control to suppress utter and utilise warping for control over a wide range of operating conditions. The work presented in this thesis is more limited in scope, and is aimed at robustly controlling a simplified aeroelastic model.

1.1 Aims and objectives

The aim of this research is to create and implement novel aeroelasticity control schemes to robustly suppress undesirable aeroelastic phenomena, such as utter and limit-cycle oscillations. The aeroelastic system under investigation is the Nonlinear Aeroelastic Test Apparatus (NATA), located at Texas A&M University. The NATA features a strong torsional stiffness nonlinearity, which has been the focus of many nonlinear controllers. The control schemes in this work will focus on robustly scheduling with airspeed, rather than focussing on the NATA torsional stiffness nonlinearity.

The aeroelastic model of the NATA most commonly used by the research community neglects the dynamics of the control surface, however for this to be a reasonable approximation the servo dynamics should be at least approximately ten times as fast as the plant dynamics, which is not the case for the NATA.

Thus, the objectives of this research are:

- Develop an improved three degree-of-freedom (including the trailing-

edge actuator dynamics) and a four degree-of-freedom (including both trailing- and leading-edge actuator dynamics) dynamic model of the NATA.

- Using a quasi-steady aerodynamic model, represent the aeroelastic dynamics of the NATA in LPV form as a function of airspeed.

- Investigate alternative forms for representing, and controlling, the airspeed parameter dependence of the NATA.

- Develop robust control laws that schedule with airspeed, and suppress utter.

- Investigate methods of reducing the norm bound (increasing the performance) of LPV controllers.

1.2   Outline

Chapter 2 presents the background theory behind aeroelasticity, control theory, and the use of LMIs in control theory. A reader familiar with such theories may proceed to Chapter 3.

A review of the work that has been done for LMIs in control theory and the active control of aeroelasticity is presented in Chapter 3. This review shows that while there has been much research into aeroelasticity control, there is an opportunity to research the use of LPV controllers for robust scheduled aeroelasticity control.

The NATA is presented in Chapter 4, where three and four degree-of-freedom LPV models are derived. These models include the dynamics of the leading- and trailing-edge servo motors which have often been neglected in previous literature, but are slow enough that their dynamics need to be considered for effective control. A quasi-steady aerodynamic model is then combined with the mechanical model of the NATA. Parameter identification for this model is performed, and finally the dependence of the nonlinear model on the torsional stiffness nonlinearity and airspeed is performed.

In Chapter 5, LPV controller synthesis LMIs are derived based on the Linear Quadratic Regulator (LQR) framework. Using these, an LPV LQR controller that is scheduled with airspeed is synthesised for the

three degree-of-freedom NATA model. This controller is experimentally validated on the NATA, and the results are presented. At the end of this chapter, a comparison is performed between this LPV LQR control method synthesised using the $\mathcal{H}_2$ norm and with the same control criteria based on the $\mathcal{GH}_2$ norm.

In Chapter 6, a method of reducing the norm bound (increasing the performance) of LPV controllers when using a parameter dependent transformed Lyapunov variable is presented. This technique is applied to the $\mathcal{H}_2$ based LPV LQR controller from Chapter 5 and shown to effectively increase the closed-loop performance across most of the design airspeed range.

In Chapter 7, the LPV model of the NATA, which has a quadratic dependence upon airspeed, is linearised using a Linear Fractional Transformation (LFT). Using this model, a Linear Fractional Representation (LFR) controller is synthesised, such that it too schedules with airspeed in the same fashion as the NATA model. This controller is based on the induced $\mathcal{L}_2$ loop-shaping framework, which provide robustness guarantees against coprime factorised perturbations.

Finally, conclusions and future work are presented in Chapter 8.

1.3 Publications arising from this thesis

Sections of the work presented in this thesis have been previously published. Specifically, the work presented in Chapter 5 is based on the publication:

Prime, Z., B. Cazzolato, C. Doolan, and T. Strganac (2010). "Linear-parameter-varying control of an improved three-degree-of-freedom aeroelastic model". In: *AIAA Journal of Guidance, Control and Dynamics* Vol. 33, No. 2, pp. 615–619. DOI: 10.2514/1.45657. See pp. ii, 99.

and the work presented in Chapter 7 is a reformulation of the publication:

Prime, Z., B. Cazzolato, and C. Doolan (2008). "A mixed $\mathcal{H}_2/\mathcal{H}_\infty$ scheduling control scheme for a two degree-of-freedom aeroelastic system under varying airspeed and gust conditions". In: *AIAA Guidance, Navigation and Control Conference*. Honolulu, Hawaii, USA. 18–21 August. See pp. iii, 131, 137.

1.4   Thesis format

To comply with The University of Adelaide format requirements, the print and PDF versions of this thesis must be identical. As a result, hyperlinks, such as cross links to chapters, sections, equations, figures and tables, in the PDF version of this document are black, but are still active.

Many of the chapters in this thesis have additional material, such as the numeric values of matrices, that have not been explicitly displayed in the text. Instead these have been embedded inside the PDF version of this document, or written to the accompanying additional material CD found inside the back cover of the printed editions. Attachments are not visible in all PDF viewers, but are known to work in Adobe Reader.

2 Preliminary Theory

In this chapter a brief overview of the existing theory used throughout this work is presented, before a more thorough literature review in Chapter 3.

The preliminary theory starts with an overview of linear systems, including performance specifications often used in controller development, and some common methods of controller synthesis. An overview of convex optimisation and Linear Matrix Inequalities (LMIs) is presented, and it is shown how to represent common performance specifications as LMIs. A general procedure for transforming analysis LMIs to synthesis LMIs is presented, followed by the use of LMIs for synthesising Linear Parameter Varying (LPV) controllers.

Some preliminary aeroelastic theory is also presented, including descriptions of the static aeroelastic phenomena of divergence and control reversal, and overviews of the aerodynamic models used for the dynamic aeroelastic phenomena of gust loading and utter or limit-cycle oscillations.

2.1 Notation

$<, \leq, >, \geq$	scalar or element-wise inequalities.
$\prec, \preceq, \succ, \succeq$	matrix inequalities.
$a := b$	a is defined to be equal to b.
$(a, b]$	set open on a and closed on b.
$\begin{bmatrix} a & b & c \end{bmatrix}$	row vector containing a, b and c.
$\mathbb{R}$	the set of real numbers.
$\mathbb{I}$	the set of imaginary numbers.
$\mathbb{C}$	the set of complex numbers.
$\mathbb{R}^n$	the set of real vectors containing n elements.

$\mathbb{S}^{n \times n}$ the set of symmetric matrices with dimensions $n \times n$.

$\text{Tr}(\mathbf{P})$ trace ($\sum p_{i,i}$) of the matrix $\mathbf{P}$.

$\mathbf{P}^{\mathsf{T}}$ transpose of the matrix $\mathbf{P}$.

$\mathbf{P}^{\dagger}$ conjugate transpose, or Hermitian transpose, of the matrix $\mathbf{P}$.

$\text{sym}(\mathbf{P})$ $\mathbf{P}$ plus its transpose: $\mathbf{P} + \mathbf{P}^{\mathsf{T}}$.

$\mathbf{P} = \mathbf{P}^{\dagger}$ is the definition of a Hermitian matrix.

$\mathbf{I}$ the identity matrix, of dimensions necessary for the context.

$\mathbf{0}$ the zero matrix, of dimensions necessary for the context.

$\left[\begin{array}{c|c} \mathbf{A} & \mathbf{B} \\ \hline \mathbf{C} & \mathbf{D} \end{array} \right]$ shorthand for the system $\mathbf{C}(s\mathbf{I} - \mathbf{A})^{-1}\mathbf{B} + \mathbf{D}$.

$\left[\begin{array}{c|c} \mathbf{A}_c & \mathbf{B}_c \\ \hline \mathbf{C}_c & \mathbf{D}_c \end{array} \right]$ state-space matrices of the controller $\mathbf{K}$.

$\left[\begin{array}{c|c} \mathcal{A} & \mathcal{B} \\ \hline \mathcal{C} & \mathcal{D} \end{array} \right]$ state-space matrices of the closed-loop system $\mathcal{G}_{cl}$.

2.2 Systems and control

The work presented in this section assumes the reader is familiar with the fundamentals of linear systems and control systems. A good introductory text is Franklin et al. (1994).

2.2.1 Compact state-space notation

Consider the linear state-space system of the form:

$$\mathbf{x} = \mathbf{A}\mathbf{x} + \mathbf{B}\mathbf{u}, \text{ and} \tag{2.1}$$

$$\mathbf{y} = \mathbf{C}\mathbf{x} + \mathbf{D}\mathbf{u}, \tag{2.2}$$

where:

     $\mathbf{x}$ is a state vector,

     $\mathbf{u}$ is an input vector,

     $\mathbf{y}$ is an output vector,

A is the state matrix,
B is the input matrix,
C is the output matrix, and
D is the pass-through matrix.
This system will be abbreviated to the compact state-space notation:

$$\mathbf{G} := \left[\begin{array}{c|c} \mathbf{A} & \mathbf{B} \\ \hline \mathbf{C} & \mathbf{D} \end{array} \right], \tag{2.3}$$

which is shorthand for the matrix equation for Equations (2.1) and (2.2):

$$\mathbf{G} : \quad \left[\begin{array}{c} \mathbf{x} \\ \hline \mathbf{y} \end{array} \right] = \left[\begin{array}{c|c} \mathbf{A} & \mathbf{B} \\ \hline \mathbf{C} & \mathbf{D} \end{array} \right] \left[\begin{array}{c} \mathbf{x} \\ \hline \mathbf{u} \end{array} \right]. \tag{2.4}$$

The transfer function corresponding to Equation (2.3) is:

$$\mathbf{G}(s) = \mathbf{C}(s\mathbf{I} - \mathbf{A})^{-1}\mathbf{B} + \mathbf{D}. \tag{2.5}$$

2.2.2 Generalised control problem

Consider the state-space (or time-domain) linear system:

$$\mathbf{P} : \quad \left[\begin{array}{c} \mathbf{x} \\ \hline \mathbf{z}_j \\ \hline \mathbf{y} \end{array} \right] = \left[\begin{array}{c|c|c} \mathbf{A} & \mathbf{B}_j & \mathbf{B} \\ \hline \mathbf{C}_j & \mathbf{D}_j & \mathbf{E}_j \\ \hline \mathbf{C} & \mathbf{F}_j & \mathbf{D} \end{array} \right] \left[\begin{array}{c} \mathbf{x} \\ \hline \mathbf{w}_j \\ \hline \mathbf{u} \end{array} \right], \tag{2.6}$$

where:
x is a state vector,
u is the controllable system input,
y is the measurable system output,
$\mathbf{w}_j$ is a performance or disturbance input, and
$\mathbf{z}_j$ is a performance or disturbance output.
The performance input and output are given the subscript j to show that an arbitrary number of performance channels can be used simultaneously.

The generalised control problem is to design a controller which has **y** from Equation (2.6) as the input, and **u** from Equation (2.6) as the output:

$$\mathbf{K} : \quad \left[\begin{array}{c} \mathbf{x}_c \\ \hline \mathbf{u} \end{array} \right] = \left[\begin{array}{c|c} \mathbf{A}_c & \mathbf{B}_c \\ \hline \mathbf{C}_c & \mathbf{D}_c \end{array} \right] \left[\begin{array}{c} \mathbf{x}_c \\ \hline \mathbf{y} \end{array} \right], \tag{2.7}$$

such that for the closed loop system:

$$\mathcal{G}_{cl}: \quad \left[\begin{array}{c} \mathbf{x}_{cl} \\ \hline \mathbf{z}_j \end{array} \right] = \left[\begin{array}{c|c} \mathcal{A} & \mathcal{B}_j \\ \hline \mathcal{C}_j & \mathcal{D}_j \end{array} \right] \left[\begin{array}{c} \mathbf{x}_{cl} \\ \hline \mathbf{w}_j \end{array} \right], \quad (2.8)$$

as shown in Figure 2.1, an arbitrary performance specification is achieved from $\mathbf{w}_j$ to $\mathbf{z}_j$.

2.2.3 Linear fractional transform

A linear fractional transform (LFT), as generally referred to in control theory, is a matrix generalisation of the scalar, complex variable function (Zhou et al. 1996):

$$F(s) = \frac{a + bs}{c + ds}, \quad (2.9)$$

where:

a, b, c and $d \in \mathbb{C}$.

For a matrix $\mathbf{P}$ with dimensions $(m_1 + m_2) \times (n_1 + n_2)$ partitioned as:

$$\mathbf{P}: \quad \left[\begin{array}{c} \mathbf{z} \\ \mathbf{y} \end{array} \right] = \left[\begin{array}{cc} \mathbf{P}_{11} & \mathbf{P}_{12} \\ \mathbf{P}_{21} & \mathbf{P}_{22} \end{array} \right] \left[\begin{array}{c} \mathbf{w} \\ \mathbf{u} \end{array} \right], \quad (2.10)$$

upper and *lower* linear fractional transforms with matrices Δ_u and Δ_l respectively are defined as (Skogestad and Postlethwaite 2005):

$$\mathcal{F}_u(\mathbf{P}, \Delta_u) := \mathbf{P}_{22} + \mathbf{P}_{21}\Delta_u(\mathbf{I} - \mathbf{P}_{11}\Delta_u)^{-1}\mathbf{P}_{12}, \text{ and} \quad (2.11)$$

$$\mathcal{F}_l(\mathbf{P}, \Delta_l) := \mathbf{P}_{11} + \mathbf{P}_{12}\Delta_l(\mathbf{I} - \mathbf{P}_{22}\Delta_l)^{-1}\mathbf{P}_{21} \quad (2.12)$$

respectively, and are more intuitively shown in Figure 2.2.
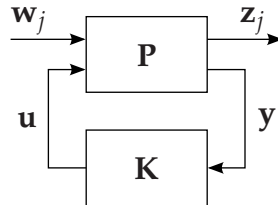
Figure 2.1: Closed-loop generalised control problem.

(a) Upper linear fractional transfor-
mation.

(b) Lower linear fractional transfor-
mation.
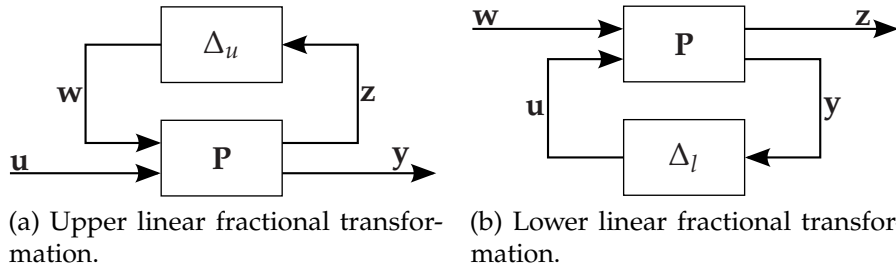
Figure 2.2: Linear Fractional Transformations used in control theory.

The upper LFT is often used to represent uncertainty in a plant. An interesting use of the upper LFT is to show the relationship between a state-space system, and a static matrix:

$$\left[\begin{array}{c|c} \mathbf{A} & \mathbf{B} \\ \hline \mathbf{C} & \mathbf{D} \end{array}\right] \equiv \mathcal{F}_u\left(\left[\begin{array}{cc} \mathbf{A} & \mathbf{B} \\ \mathbf{C} & \mathbf{D} \end{array}\right], \frac{1}{s}\right). \tag{2.13}$$

In control theory, the lower LFT is often used when closing the loop with a controller, $\mathbf{K}$, thus the closed-loop system

$$\left[\begin{array}{c|c} \mathcal{A} & \mathcal{B} \\ \hline \mathcal{C} & \mathcal{D} \end{array}\right] \equiv \mathcal{F}_l\left(\left[\begin{array}{c|c} \mathbf{A} & \mathbf{B} \\ \hline \mathbf{C} & \mathbf{D} \end{array}\right], \mathbf{K}\right). \tag{2.14}$$

2.2.4 Performance speci cations

A brief overview of performance specifications used in control theory is given in the following. For a more complete overview of performance specifications the reader is referred to the text by Zhou et al. (1996).

Firstly, a few preliminary definitions will be introduced.

A *normed* vector space, V, is a vector space for which a norm, $\|\cdot\|$, is defined on V.

A Cauchy sequence is a sequence, x_n, in a normed space V, with $\|x_n - x_m\| \to 0$ as $n, m \to \infty$. The normed space, V, is said to be *complete* if every Cauchy sequence in V converges to V, which means for $x \in V$, $\|x_n - x\| \to 0$ as $n \to \infty$.

A *Banach space* is a real or complex *complete* and *normed* vector space. An important set of Banach spaces used in control theory are:

$\mathcal{L}_p(I)$ **spaces for** $1 \leq p \leq \infty$. $\mathcal{L}_p$ spaces consist of all Lebesgue integrable[1] functions, $\mathbf{f}(t)$, over the interval $I \subset \mathbb{R}$, with norms (Zhou et al. 1996):

$$\|\mathbf{f}\|_p := \left(\int_I |\mathbf{f}(t)|^p dt \right)^{\frac{1}{p}} < \infty, \text{ for } 0 \leq p < \infty, \text{ and} \qquad (2.15)$$

$$\|\mathbf{f}\|_\infty := \sup_{t \in I} |\mathbf{f}(t)|. \qquad (2.16)$$

2.2.4.1 Hilbert spaces and the $\mathcal{H}_2$ Hardy space

A *Hilbert space* is a real or complex *complete inner product* space, which means it is a complete vector space with an inner product defined, and the norm is induced by the inner product. A Hilbert space is also a Banach space. An important set of real, infinite dimensional, matrix valued and functional Hilbert spaces in the time domain over Lebesgue integrable functions are (Zhou et al. 1996):

$\mathcal{L}_2 = \mathcal{L}_2(-\infty, \infty)$**:** for functions $\mathbf{f}(t)$ and $\mathbf{g}(t)$ with inner product defined by:

$$\langle \mathbf{f}, \mathbf{g} \rangle = \int_{-\infty}^{\infty} \text{Tr}[\mathbf{f}^\dagger(t)\mathbf{g}(t)]dt. \qquad (2.17)$$

$\mathcal{L}_{2+} = \mathcal{L}_2[0, \infty)$**:** is a subspace of $\mathcal{L}_2$ above, with $\mathbf{f}(t)$ and $\mathbf{g}(t)$ zero for $t < 0$.

$\mathcal{L}_{2-} = \mathcal{L}_2(-\infty, 0]$**:** is a subspace of $\mathcal{L}_2$ with $\mathbf{f}(t)$ and $\mathbf{g}(t)$ zero for $t > 0$.
  Similarly in the frequency domain, the $\mathcal{L}_2(j\mathbb{R})$ Hilbert space consists of all complex, matrix valued (or scalar) functions, $\mathbf{F}$ with bounded integral (Zhou et al. 1996):

$$\int_{-\infty}^{\infty} \text{Tr}[\mathbf{F}^\dagger(j\omega)\mathbf{F}(j\omega)]d\omega < \infty, \qquad (2.18)$$

inner product defined by:

$$\langle \mathbf{F}, \mathbf{G} \rangle := \frac{1}{2\pi} \int_{-\infty}^{\infty} \text{Tr}[\mathbf{F}^\dagger(j\omega)\mathbf{G}(j\omega)]d\omega, \qquad (2.19)$$

---

[1]f is Lebesgue integrable if $\int f^+ d\mu < \infty$, $\int f^- d\mu < \infty$ where $f^+ = \max(f, 0)$ and $f^- = \max(-f, 0)$.

for $\mathbf{F}, \mathbf{G} \in \mathcal{L}_2$, and the inner product induced norm defined as

$$\|\mathbf{F}\|_2 := \sqrt{\langle \mathbf{F}, \mathbf{F} \rangle}. \tag{2.20}$$

The $\mathcal{H}_2$ Hardy space is a subspace of $\mathcal{L}_2(j\mathbb{R})$ with the functions $\mathbf{F}(s)$ analytic for $\text{Re}(s) > 0$, i.e. the transfer function contains no right-hand plane poles. The corresponding norm is defined as (Zhou et al. 1996):

$$\|\mathbf{F}\|_2^2 := \sup_{\text{Re}(s)>0} \left\{ \frac{1}{2\pi} \int_{-\infty}^{\infty} \text{Tr}[\mathbf{F}^\dagger(\sigma + j\omega)\mathbf{F}(\sigma + j\omega)]d\omega \right\}, \tag{2.21}$$

but can also be shown to be (Zhou et al. 1996):

$$\|\mathbf{F}\|_2^2 = \frac{1}{2\pi} \int_{-\infty}^{\infty} \text{Tr}[\mathbf{F}^\dagger(j\omega)\mathbf{F}(j\omega)]d\omega. \tag{2.22}$$

2.2.4.2 The $\mathcal{H}_\infty$ Hardy space

The $\mathcal{L}_\infty(j\mathbb{R})$ space is a Banach space of complex, matrix values functions that are bounded on $j\mathbb{R}$, with the norm defined as:

$$\|\mathbf{F}\|_\infty := \sup_{\omega \in \mathbb{R}} \bar{\sigma}[\mathbf{F}(j\omega)], \tag{2.23}$$

where $\bar{\sigma}$ denotes the maximum singular value.

In the same way as the $\mathcal{L}_2$ space relates to the $\mathcal{H}_2$ Hardy space, the $\mathcal{H}_\infty$ Hardy space is a subspace of $\mathcal{L}_\infty(j\mathbb{R})$, with the functions $\mathbf{F}(s)$ analytic in $\text{Re}(s) > 0$. The $\mathcal{H}_\infty$ norm is defined as (Zhou et al. 1996):

$$\|\mathbf{F}\|_\infty := \sup_{\text{Re}(s)>0} \bar{\sigma}[\mathbf{F}(s)] = \sup_{\omega \in \mathbb{R}}[\mathbf{F}(j\omega)]. \tag{2.24}$$

2.2.4.3 Induced system norms

An important concept when analysing performance is the gain a system, $\mathbf{G}$, applies from the performance (or disturbance) input, $\mathbf{w}$, to the performance (or disturbance) output $\mathbf{z}$. This can be thought of as $\mathbf{G}$ inducing a norm on the performance channel, and is essentially a signal based interpretation of performance. Induced norms are especially useful for performance analysis when $\mathbf{G}$ is nonlinear. Several important induced norms are described below.

$\mathcal{L}_2$ **induced norm**   The $\mathcal{L}_2$ induced norm is defined as (Boyd et al. 1994):

$$\|\mathbf{G}\|_{\mathcal{L}_2} := \sup_{0 < \|\mathbf{w}\|_2 < \infty} \frac{\|\mathbf{z}\|_2}{\|\mathbf{w}\|_2}. \tag{2.25}$$

An interesting property of the $\mathcal{L}_2$ induced norm is that for linear $\mathbf{G}$ it is equivalent to the $\mathcal{H}_\infty$ norm of $\mathbf{G}$. There are many instances in literature where $\mathcal{H}_\infty$ control problems have been generalised from their strict definitions. Zhou et al. (1996) note of these:

> It should be mentioned that in these generalizations the term $\mathcal{H}_\infty$ has come to be (mis-)used to mean the induced norm in $\mathcal{L}_2$.

$\mathcal{L}_\infty$ **induced norm**   The $\mathcal{L}_\infty$ induced norm is defined as (Zhou et al. 1996):

$$\|\mathbf{G}\|_{\mathcal{L}_\infty} := \sup_{0 < \|\mathbf{w}\|_\infty < \infty} \frac{\|\mathbf{z}\|_\infty}{\|\mathbf{w}\|_\infty}. \tag{2.26}$$

When $\mathbf{G}$ is linear, the $\mathcal{L}_\infty$ induced norm is equivalent to the $\mathcal{L}_1$ norm of $\mathbf{G}$.

The Generalised $\mathcal{H}_2$ ($\mathcal{GH}_2$) norm   The $\mathcal{GH}_2$ norm is a signal based generalisation of the $\mathcal{H}_2$ norm, and is defined as the induced norm from $\mathbf{w} \in \mathcal{L}_2[0, \infty)$ to $\mathbf{z} \in \mathcal{L}_\infty(0, \infty)$ (Rotea 1993), and is sometimes written as the $\mathcal{L}_2$–$\mathcal{L}_\infty$ induced norm, or the energy to peak norm. An alternative definition that is often used is:

$$\|\mathbf{G}\|_g := \sup_{0 < \|\mathbf{w}\|_2 < \infty} \frac{\|\mathbf{z}\|_\infty}{\|\mathbf{w}\|_2}. \tag{2.27}$$

When $\mathbf{G}$ in linear, the $\mathcal{GH}_2$ norm satisfies:

$$\|\mathbf{G}\|_g^2 = \frac{1}{2\pi} \lambda_{\max} \left(\int_{-\infty}^{\infty} \mathbf{G}(j\omega)\mathbf{G}^\dagger(j\omega) d\omega \right), \tag{2.28}$$

where $\lambda_{\max}(\cdot)$ denotes the maximum eigenvalue. Thus when $\mathbf{z}$ is scalar, the $\mathcal{GH}_2$ norm reduces to the $\mathcal{H}_2$ norm.

2.2.5 Common linear control problems

This section will brie y describe some common state-space based linear control methods. More details on these methods can be found in many control theory texts, such as that by Skogestad and Postlethwaite (2005).

2.2.5.1 Linear Quadratic Regulator (LQR) Control

For a state-output system:

$$\mathbf{G}: \quad \left[\begin{array}{c} \mathbf{x} \\ \hline \mathbf{y} \end{array}\right] = \left[\begin{array}{c|c} \mathbf{A} & \mathbf{B} \\ \hline \mathbf{I} & \mathbf{0} \end{array}\right] \left[\begin{array}{c} \mathbf{x} \\ \hline \mathbf{u} \end{array}\right] \tag{2.29}$$

with $\mathbf{x} \in \mathbb{R}^n$ and $\mathbf{u} \in \mathbb{R}^m$, the LQR control problem is to find a static feedback controller, $\mathbf{K}$, such that the quadratic performance index

$$J = \int_0^\infty \left(\mathbf{x}^{\mathrm{T}}(t)\mathbf{Q}\mathbf{x}(t) + \mathbf{u}^{\mathrm{T}}(t)\mathbf{R}\mathbf{u}(t) \right) dt \tag{2.30}$$

is minimised, where

$\mathbf{Q} \in \mathbb{S}^{n \times n} \cap \mathbb{R}^{n \times n}$ is the state weighting matrix, and

$\mathbf{R} \in \mathbb{S}^{m \times m} \cap \mathbb{R}^{m \times m}$ is the input weighting matrix.

The optimal solution is $\mathbf{K} = \mathbf{R}^{-1}\mathbf{B}^{\mathrm{T}}\mathbf{P}$, where $\mathbf{P} \in \mathbb{S}^{n \times n} \cap \mathbb{R}^{n \times n}$ is the solution to the algebraic Riccati equation

$$\mathbf{A}^{\mathrm{T}}\mathbf{P} + \mathbf{P}\mathbf{A} - \mathbf{P}\mathbf{B}\mathbf{R}^{-1}\mathbf{B}^{\mathrm{T}}\mathbf{P} + \mathbf{Q} = 0, \text{ and } \mathbf{P} \succeq 0. \tag{2.31}$$

This standard LQR problem can be represented as an equivalent generalised control problem minimising the $\mathcal{H}_2$ norm from $\mathbf{w}$ to $\mathbf{z}$ (Feron et al. 1992, and Zhou et al. 1996):

$$\left[\begin{array}{c} \mathbf{x} \\ \hline \mathbf{z} \\ \hline \mathbf{y} \end{array}\right] = \left[\begin{array}{c|c|c} \mathbf{A} & \mathbf{I} & \mathbf{B} \\ \hline \mathbf{Q}^{1/2} & \mathbf{0} & \mathbf{0} \\ \mathbf{0} & \mathbf{0} & \mathbf{R}^{1/2} \\ \hline \mathbf{I} & \mathbf{0} & \mathbf{0} \end{array}\right] \left[\begin{array}{c} \mathbf{x} \\ \hline \mathbf{w} \\ \hline \mathbf{u} \end{array}\right]. \tag{2.32}$$

2.2.5.2 $\mathcal{H}_\infty$ loop-shaping

The $\mathcal{H}_\infty$ loop-shaping process involves shaping the singular values of a plant:

$$\mathbf{G} = \left[\begin{array}{c|c} \mathbf{A} & \mathbf{B} \\ \hline \mathbf{C} & \mathbf{D} \end{array}\right], \tag{2.33}$$

with pre- and post-compensators, $\mathbf{W}_1$ and $\mathbf{W}_2$ respectively, to achieve a desired performance. A robustly stabilising controller for the shaped plant is then synthesised using $\mathcal{H}_\infty$ optimisation (Glover and McFarlane 1989, and Skogestad and Postlethwaite 2005).

The pre- and post-compensators are usually chosen to fulfil the following:

- Normalise all of the inputs and outputs against their maximum expected values.

- Diagonalise the plant as much as possible (i.e. permute the inputs or outputs so that the first input has the greatest effect on the first output, and so on).

- Provide high open-loop singular values at low frequencies. This ensures good command following and disturbance rejection.

- Low singular value roll-off at the gain cross-over frequency to improve stability.

- Low singular values at high frequencies for reduced sensitivity to noise and plant uncertainty.

With the scaled plant given by $\mathbf{G}_s = \mathbf{W}_2\mathbf{G}\mathbf{W}_1$, the stabilising $\mathcal{H}_\infty$ controller, $\mathbf{K}_\infty$, is synthesised to minimise the $\mathcal{H}_\infty$ norm, γ, of (Zhou et al. 1996)

$$\left\| \begin{bmatrix} \mathbf{I} \\ \mathbf{K}_\infty \end{bmatrix} (\mathbf{I} + \mathbf{G}_s\mathbf{K}_\infty)^{-1} \begin{bmatrix} \mathbf{I} & \mathbf{G}_s \end{bmatrix} \right\|_\infty \leq \gamma. \tag{2.34}$$

The plant $\mathbf{G}$ can be left coprime factorised into:

$$\mathbf{G} = \mathbf{M}^{-1}\mathbf{N}, \tag{2.35}$$

where $\mathbf{M}$ and $\mathbf{N}$ are stable coprime transfer functions, which implies that all right-hand plane zeros of $\mathbf{G}$ are contained in $\mathbf{N}$, and the right-hand plane poles of $\mathbf{G}$ are contained in $\mathbf{M}$ as right-hand plane zeros.

With additive perturbations $\Delta_\mathbf{M}$ and $\Delta_\mathbf{N}$ applied to $\mathbf{M}$ and $\mathbf{N}$ respectively, the left coprime factor perturbed plant is

$$\mathbf{G} = (\mathbf{M} + \Delta_\mathbf{M})^{-1}(\mathbf{N} + \Delta_\mathbf{N}), \tag{2.36}$$

as shown in Figure 2.3.
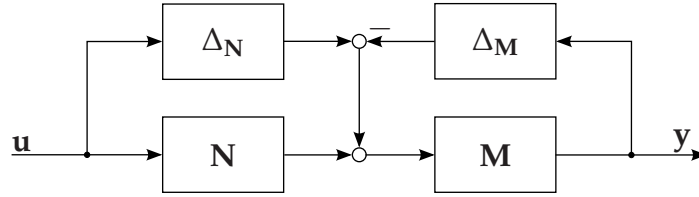
Figure 2.3: Left coprime factor perturbed system.

The system controlled by $\mathbf{K}_\infty$ is robustly stable so long as the perturbations

$$\left\| \begin{bmatrix} \Delta_\mathbf{N} & \Delta_\mathbf{M} \end{bmatrix} \right\|_\infty < \epsilon, \tag{2.37}$$

where $\epsilon = \frac{1}{\gamma}$.

The equivalent generalised control problem can easily be found by setting the performance input and output of the scaled system to

$$\mathbf{w}_s = \begin{bmatrix} \mathbf{u}_s & \mathbf{y}_s \end{bmatrix}^\mathrm{T}, \text{ and} \tag{2.38}$$

$$\mathbf{z}_s = \begin{bmatrix} \mathbf{y}_s & \mathbf{u}_s \end{bmatrix}^\mathrm{T}. \tag{2.39}$$

This gives the generalised control problem for the scaled plant as (Majumder et al. 2005):

$$\mathbf{P} = \left[\begin{array}{c|cc|c} \mathbf{A}_s & \mathbf{B}_s & \mathbf{0} & \mathbf{B}_s \\ \hline \mathbf{C}_s & \mathbf{0} & \mathbf{I} & \mathbf{0} \\ \mathbf{0} & \mathbf{0} & \mathbf{0} & \mathbf{I} \\ \hline \mathbf{C}_s & \mathbf{0} & \mathbf{I} & \mathbf{0} \end{array} \right]. \tag{2.40}$$

The stabilising $\mathcal{H}_\infty$ controller is then constructed to minimise the $\mathcal{H}_\infty$ (or $\mathcal{L}_2$ induced) norm from $\mathbf{w}_s$ to $\mathbf{z}_s$.

2.3 Linear Matrix Inequalities in control theory

In this section Linear Matrix Inequalities (LMIs) are presented as a convex optimisation problem. It is then shown how to use LMIs to solve standard control problems, as well as Linear Parameter Varying (LPV) control problems.

2.3.1 Convex optimisation

A general optimisation problem has the form (Boyd and Vandenberghe 2004):

$$\begin{aligned} \text{minimise} \quad & f_0(\mathbf{x}) \\ \text{subject to} \quad & f_i(\mathbf{x}) \leq b_i, \quad i = 1, \ldots, m \end{aligned} \tag{2.41}$$

where:

$\mathbf{x} \in \mathbb{R}^n$ is the optimisation variable,

$f_0 : \mathbb{R}^n \mapsto \mathbb{R}$ is the optimisation problem, and

$f_i : \mathbb{R}^n \mapsto \mathbb{R}$ for $i = 1, \ldots, m$ are the optimisation constraints.

A value $\mathbf{x}^* \in \mathbb{R}^n$ is optimal if $f_0(\mathbf{x}) \geq f_0(\mathbf{x}^*)$ for any $\mathbf{x} \in \mathbb{R}^n$ which satisfies the optimisation constraints: $f_i(\mathbf{x}) \leq b_i$, $i = 1, \ldots, m$.

A convex optimisation problem is an optimisation problem where both the problem and the constraints satisfy:

$$f_i\left(\alpha \mathbf{x}_1 + (1 - \alpha)\mathbf{x}_2\right) \leq \alpha f_i(\mathbf{x}_1) + (1 - \alpha)f_i(\mathbf{x}_2) \tag{2.42}$$

where:

$\mathbf{x}_1, \mathbf{x}_2 \in \mathbb{R}^n$, and

$\alpha \in [0, 1]$.

Convex optimisation can be seen as a generalisation of a linear programming problem: replacing the inequality in Equation (2.42) with an equality creates a linear programming problem. Whilst there are no analytical solutions to convex optimisation problems, there are several efficient numerical optimisation techniques, in particular the interior point methods (Boyd and Vandenberghe 2004), that can reliably solve large problems in a practical time frame.

The difficulty of convex optimisation lies in the recognising or constructing convex optimisation properties, to the extent that Boyd and Vandenberghe (2004) state:

> With only a bit of exaggeration, we can say that, if you formulate a practical problem as a convex optimization problem, then you have solved the original problem.

2.3.2 Linear Matrix Inequalities

A Linear Matrix Inequality (LMI) is an expression of the form:

$$\mathbf{P}(\mathbf{x}) := \mathbf{P}_0 + \mathbf{P}_1 x_1 + \ldots + \mathbf{P}_n x_n \prec 0 \tag{2.43}$$

where:

$x_i \in \mathbb{R}$,

$\mathbf{x} = [x_1, \ldots, x_n]$ is the optimisation variable, and

$\mathbf{P}_i \in \mathbb{S}^{m \times m} \cap \mathbb{R}^{m \times m}$ for $i = 0, \ldots, n$.

The matrix inequality $\mathbf{P}(\mathbf{x}) \prec 0$ is used to show that $\mathbf{P}(\mathbf{x})$ is *negative definite*, which is defined as meaning $\mathbf{u}^\mathsf{T} \mathbf{P}(\mathbf{x}) \mathbf{u} < 0$ for any non-zero $\mathbf{u} \in \mathbb{R}^m$. A further characterisation of a negative definite matrix is that all of its eigenvalues are negative: $\lambda\left(\mathbf{P}(\mathbf{x})\right) < 0$.

Similar definitions exist for *negative semidefinite* (nonstrict inequalities), *positive definite*, and *positive semidefinite*.

Linear Matrix Inequalities form a convex constraint on the optimisation variable $\mathbf{x}$, which can be easily shown using the formulation above. With $\mathbf{x}_1, \mathbf{x}_2 \in \mathbb{R}^n$, and $\alpha \in [0, 1]$:

$$\mathbf{P}\left(\alpha \mathbf{x}_1 + (1 - \alpha)\mathbf{x}_2\right) = \alpha \mathbf{P}(\mathbf{x}_1) + (1 - \alpha)\mathbf{P}(\mathbf{x}_2) \prec 0. \qquad (2.44)$$

Thus Linear Matrix Inequality problems can be solved quickly and efficiently, as briefy discussed above in Section 2.3.1.

A property of Linear Matrix Inequalities that will be used heavily and implicitly from this point forward is that *multiple LMIs can be expressed as a single LMI* (VanAntwerp and Braatz 2000). That is, the series of LMIs:

$$\mathbf{P}_1(\mathbf{x}) \prec 0, \ldots, \mathbf{P}_m(\mathbf{x}) \prec 0 \qquad (2.45)$$

can be written as the single LMI:

$$\mathrm{diag}\left(\mathbf{P}_1(\mathbf{x}), \ldots, \mathbf{P}_m(\mathbf{x})\right) \prec 0 \qquad (2.46)$$

Throughout this work all Linear Matrix Inequalities will feature *matrices as variables*, that is whenever a matrix variable is shown, the scalar variables x_i that form the LMI are implicit. Thus from this point forward the functional dependence on $\mathbf{x}$ will be omitted from the equations. As an example, the LMI $\mathbf{P}(\mathbf{x}) \prec 0$ will be written as $\mathbf{P} \prec 0$. When used for Linear Parameter Varying system, the functional dependence will omit the dependence on x_i. For example, the LMI $\mathbf{P}(\mathbf{x}, y_1) = \mathbf{P}_0(\mathbf{x}) + \mathbf{P}_1(\mathbf{x})y_1$ will henceforth be written as $\mathbf{P}(y_1) = \mathbf{P}_0 + \mathbf{P}_1 y_1$.

2.3.3 Common Linear Matrix Inequality problems

Much of the interest in Linear Matrix Inequalities in control theory stems from the ability to represent many standard and accepted control

methodologies in LMI form. A thorough treatment of LMIs in control theory, including a much broader range of problems is given by Boyd et al. (1994).

Schur complement lemma   As a preliminary to some of the control methodologies, the Schur complement converts a specific class of convex nonlinear inequalities into an LMI. These nonlinear inequalities occur frequently in control theory, and are given by

$$\mathbf{R} \prec 0, \text{ and} \tag{2.47}$$

$$\mathbf{Q} - \mathbf{S}\mathbf{R}^{-1}\mathbf{S}^{\mathrm{T}} \prec 0, \tag{2.48}$$

which the Schur complement converts to the LMI

$$\begin{bmatrix} \mathbf{Q} & \mathbf{S} \\ \mathbf{S}^{\mathrm{T}} & \mathbf{R} \end{bmatrix} \prec 0. \tag{2.49}$$

A proof of the Schur complement is given by VanAntwerp and Braatz (2000).

Lyapunov stability   From the work of the famous Russian scientist A. M. Lyapunov, a system is said to be asymptotically stable if we can find a positive definite storage function of the states, $\mathbf{V}$, such that its temporal derivative is negative definite. A more thorough and strict definition is given by Khalil (1996).

For the linear system

$$\mathbf{x}(t) = \mathbf{A}\mathbf{x}(t), \tag{2.50}$$

the storage function can be written in terms of a real symmetric matrix variable $\mathbf{P}$:

$$\mathbf{V}(\mathbf{x}) = \mathbf{x}^{\mathrm{T}}(t)\mathbf{P}\mathbf{x}(t) > \mathbf{0}, \ \forall \mathbf{x} \neq \mathbf{0} \tag{2.51}$$

which is the definition of a positive definite matrix, thus we require $\mathbf{P} \succ 0$. The temporal derivative of this storage function is

$$\mathbf{V}(\mathbf{x}) = \mathbf{x}^{\mathrm{T}}(t)\mathbf{P}\mathbf{x}(t) + \mathbf{x}^{\mathrm{T}}(t)\mathbf{P}\mathbf{x}(t) < 0, \ \forall \mathbf{x} \neq 0 \tag{2.52}$$

$$= \mathbf{x}^{\mathrm{T}}(t)\left(\mathbf{A}^{\mathrm{T}}\mathbf{P} + \mathbf{P}\mathbf{A}\right)\mathbf{x}(t) < 0, \ \forall \mathbf{x} \neq \mathbf{0}, \tag{2.53}$$

which is the definition of a negative definite matrix. Thus Lyapunov stability can be written as a feasibility LMI problem in $\mathbf{P}$:

$$\mathbf{P} \succ 0, \text{ and } \mathbf{A}^{\mathrm{T}}\mathbf{P} + \mathbf{P}\mathbf{A} \prec 0. \tag{2.54}$$

Quadratic nominal performance   An important concept for analysing the performance of a system is that of *quadratic nominal performance*.

Consider the linear system

$$\mathbf{G}(s): \quad \left[\begin{array}{c} \mathbf{x} \\ \hline \mathbf{z} \end{array}\right] = \left[\begin{array}{c|c} \mathbf{A} & \mathbf{B} \\ \hline \mathbf{C} & \mathbf{D} \end{array}\right] \left[\begin{array}{c} \mathbf{x} \\ \hline \mathbf{w} \end{array}\right]. \tag{2.55}$$

From Scherer and Weiland (2004), given a symmetric performance index:

$$\left[\begin{array}{cc} \mathbf{Q} & \mathbf{S} \\ \mathbf{S}^{\mathrm{T}} & \mathbf{R} \end{array}\right], \tag{2.56}$$

and suppose that $\mathbf{A} \prec 0$ and $\mathbf{x}(0) = 0$, then the following are equivalent:

1. There exists $\epsilon > 0$ such that for all $\mathbf{w} \in \mathcal{L}_2$

$$\int_0^\infty \left[\begin{array}{c} \mathbf{w} \\ \mathbf{z} \end{array}\right]^{\mathrm{T}} \left[\begin{array}{cc} \mathbf{Q} & \mathbf{S} \\ \mathbf{S}^{\mathrm{T}} & \mathbf{R} \end{array}\right] \left[\begin{array}{c} \mathbf{w} \\ \mathbf{z} \end{array}\right] dt \le -\epsilon^2 \int_0^\infty \mathbf{w}^{\mathrm{T}}(t)\mathbf{w}(t)dt, \quad (2.57)$$

2. For all $\omega \in \mathbb{R}$ there holds

$$\left[\begin{array}{c} \mathbf{I} \\ \mathbf{G}(i\omega) \end{array}\right]^{\dagger} \left[\begin{array}{cc} \mathbf{Q} & \mathbf{S} \\ \mathbf{S}^{\mathrm{T}} & \mathbf{R} \end{array}\right] \left[\begin{array}{c} \mathbf{I} \\ \mathbf{G}(i\omega) \end{array}\right] \prec 0, \text{ and} \tag{2.58}$$

3. There exists $\mathbf{P} \in \mathbb{S}^{m \times m} \cap \mathbb{R}^{m \times m}$, with $\mathbf{P} \succ 0$, such that

$$\left[\begin{array}{cc} \mathbf{I} & \mathbf{0} \\ \mathbf{A} & \mathbf{B} \\ \hline \mathbf{0} & \mathbf{I} \\ \mathbf{C} & \mathbf{D} \end{array}\right]^{\mathrm{T}} \left[\begin{array}{cc|cc} \mathbf{0} & \mathbf{P} & \mathbf{0} & \mathbf{0} \\ \mathbf{P} & \mathbf{0} & \mathbf{0} & \mathbf{0} \\ \hline \mathbf{0} & \mathbf{0} & \mathbf{Q} & \mathbf{S} \\ \mathbf{0} & \mathbf{0} & \mathbf{S}^{\mathrm{T}} & \mathbf{R} \end{array}\right] \left[\begin{array}{cc} \mathbf{I} & \mathbf{0} \\ \mathbf{A} & \mathbf{B} \\ \hline \mathbf{0} & \mathbf{I} \\ \mathbf{C} & \mathbf{D} \end{array}\right] \prec 0. \tag{2.59}$$

This definition is important because some common performance objectives can be represented in this way, such as several of the performance objectives below.

Furthermore, this representation allows for the easy conversion of these performance specifications from continuous systems to discrete systems, simply by replacing

$$\left[\begin{array}{cc} \mathbf{0} & \mathbf{P} \\ \mathbf{P} & \mathbf{0} \end{array}\right] \tag{2.60}$$

with

$$\begin{bmatrix} -\mathbf{P} & \mathbf{0} \\ \mathbf{0} & \mathbf{P} \end{bmatrix}, \qquad (2.61)$$

which tests for the eigenvalues of $\mathbf{A}$ in the unit-disk, rather than in left-half plane.

The positive-real lemma Determining if a system is *positive-real* (also known as a *dissipative* or *passive* system) is useful in robustness analysis, and also in problems such as the synthesis of passive electrical networks (Scherer and Weiland 2004).

$\mathbf{G}$ is said to be *positive-real* if (Anderson and Moore 1989):

$$\mathbf{G}(i\omega) + \mathbf{G}^{\dagger}(i\omega) \succeq 0, \ \forall \omega \in \mathbb{R} \text{ and } \det(i\omega\mathbf{I} - \mathbf{A}) \neq 0. \qquad (2.62)$$

This is equivalent to finding a feasible solution to the LMI problem in $\mathbf{P}$ (Boyd et al. 1994):

$$\mathbf{P} \succ 0, \text{ and } \begin{bmatrix} \mathbf{A}^{\mathrm{T}}\mathbf{P} + \mathbf{PA} & \mathbf{PB} - \mathbf{C}^{\mathrm{T}} \\ \mathbf{B}^{\mathrm{T}}\mathbf{P} - \mathbf{C} & -\mathbf{D}^{\mathrm{T}} - \mathbf{D} \end{bmatrix} \preceq 0. \qquad (2.63)$$

Positive-realness is an example of a quadratic performance problem, with

$$\begin{bmatrix} \mathbf{Q} & \mathbf{S} \\ \mathbf{S}^{\mathrm{T}} & \mathbf{R} \end{bmatrix} = \begin{bmatrix} \mathbf{0} & -\mathbf{I} \\ -\mathbf{I} & \mathbf{0} \end{bmatrix}. \qquad (2.64)$$

The bounded-real lemma A similarly important tool in robust analysis is determining if a system is *bounded-real*. Using the definition in Equation (2.55), a system is bounded real if (Anderson and Moore 1989):

$$\mathbf{G}^{\dagger}(i\omega)\mathbf{G}(i\omega) \leq \mathbf{I}, \ \forall \omega \in \mathbb{R} \text{ and } \det(i\omega\mathbf{I} - \mathbf{A}) \neq 0. \qquad (2.65)$$

This can also be expressed using the $\mathcal{H}_{\infty}$ norm:

$$\|\mathbf{G}\|_{\infty} \leq 1. \qquad (2.66)$$

This is equal to the feasibility LMI problem in $\mathbf{P}$ (Boyd et al. 1994):

$$\mathbf{P} \succ 0, \text{ and } \begin{bmatrix} \mathbf{A}^{\mathrm{T}}\mathbf{P} + \mathbf{PA} + \mathbf{C}^{\mathrm{T}}\mathbf{C} & \mathbf{PB} + \mathbf{C}^{\mathrm{T}}\mathbf{D} \\ \mathbf{B}^{\mathrm{T}}\mathbf{P} + \mathbf{D}^{\mathrm{T}}\mathbf{C} & \mathbf{D}^{\mathrm{T}}\mathbf{D} - \mathbf{I} \end{bmatrix} \preceq 0. \qquad (2.67)$$

Bounded-realness is an example of a quadratic performance problem, with

$$\begin{bmatrix} \mathbf{Q} & \mathbf{S} \\ \mathbf{S}^{\mathrm{T}} & \mathbf{R} \end{bmatrix} = \begin{bmatrix} -\mathbf{I} & \mathbf{0} \\ \mathbf{0} & \mathbf{I} \end{bmatrix}. \qquad (2.68)$$

The $\mathcal{H}_\infty$ norm The above bounded-real lemma is very closely related to the definition of the $\mathcal{H}_\infty$ norm, Equation (2.23). An upper bound on the $\mathcal{H}_\infty$ norm of the system in Equation (2.55):

$$\|\mathbf{G}\|_\infty \leq \gamma, \tag{2.69}$$

can be found using the LMI optimisation problem, with free variable $\mathbf{P}$ and optimisation variable γ, given by (Boyd et al. 1994):

$$\mathbf{P} \succ 0, \text{ and } \begin{bmatrix} \mathbf{A}^\mathrm{T}\mathbf{P} + \mathbf{P}\mathbf{A} + \mathbf{C}^\mathrm{T}\mathbf{C} & \mathbf{P}\mathbf{B} + \mathbf{C}^\mathrm{T}\mathbf{D} \\ \mathbf{B}^\mathrm{T}\mathbf{P} + \mathbf{D}^\mathrm{T}\mathbf{C} & \mathbf{D}^\mathrm{T}\mathbf{D} - \gamma^2\mathbf{I} \end{bmatrix} \preceq 0. \tag{2.70}$$

This form of the $\mathcal{H}_\infty$ LMIs is an example of a quadratic performance problem, with

$$\begin{bmatrix} \mathbf{Q} & \mathbf{S} \\ \mathbf{S}^\mathrm{T} & \mathbf{R} \end{bmatrix} = \begin{bmatrix} -\gamma^2\mathbf{I} & \mathbf{0} \\ \mathbf{0} & \mathbf{I} \end{bmatrix}. \tag{2.71}$$

However, this form is not amenable to controller synthesis, as it will not be affine in the controller variables due to the presence of terms like $\mathbf{C}^\mathrm{T}\mathbf{C}$.

An alternative form for the $\mathcal{H}_\infty$ analysis LMIs that is frequently used because during controller synthesis it is affine in the controller variables is (Gahinet and Apkarian 1994):

$$\mathbf{P} \succ 0, \text{ and } \begin{bmatrix} \mathbf{A}^\mathrm{T}\mathbf{P} + \mathbf{P}\mathbf{A} & \mathbf{P}\mathbf{B} & \mathbf{C}^\mathrm{T} \\ \mathbf{B}^\mathrm{T}\mathbf{P} & -\gamma\mathbf{I} & \mathbf{D}^\mathrm{T} \\ \mathbf{C} & \mathbf{D} & -\gamma\mathbf{I} \end{bmatrix} \prec 0. \tag{2.72}$$

This form of the $\mathcal{H}_\infty$ norm can be found by using the quadratic performance index

$$\begin{bmatrix} \mathbf{Q} & \mathbf{S} \\ \mathbf{S}^\mathrm{T} & \mathbf{R} \end{bmatrix} = \begin{bmatrix} -\gamma\mathbf{I} & \mathbf{0} \\ \mathbf{0} & \gamma^{-1}\mathbf{I} \end{bmatrix}, \tag{2.73}$$

and linearising the γ^{-1} term through a Schur complement transformation.

The $\mathcal{L}_2$ induced norm The Linear Matrix Inequality optimisation problem to find an upper bound on the $\mathcal{L}_2$ induced norm, Equation (2.25), is identical to that for the $\mathcal{H}_\infty$ norm, Equation (2.72).

The $\mathcal{H}_2$ norm The upper bound on the $\mathcal{H}_2$ norm, Equation (2.22), of the system described in Equation (2.55):

$$\|\mathbf{G}\|_2 < \nu, \tag{2.74}$$

can be found using LMI optimisation. Introducing an auxiliary, symmetric matrix variable $\mathbf{Z}$, the LMI problem is to optimise ν, with $\mathbf{P}$ as the free variable, the system of LMIs (Scherer et al. 1997):

$$\mathbf{D} = \mathbf{0}, \quad \begin{bmatrix} \mathbf{A}^\mathsf{T}\mathbf{P} + \mathbf{P}\mathbf{A} & \mathbf{P}\mathbf{B} \\ \mathbf{B}^\mathsf{T}\mathbf{P} & -\nu\mathbf{I} \end{bmatrix} \prec 0, \quad \begin{bmatrix} \mathbf{P} & \mathbf{C}^\mathsf{T} \\ \mathbf{C} & \mathbf{Z} \end{bmatrix} \succ 0 \text{ and } \mathrm{Tr}(\mathbf{Z}) < \nu. \tag{2.75}$$

$\mathbf{D} = \mathbf{0}$ is required for the $\mathcal{H}_2$ norm to be finite, and the usual requirement that $\mathbf{P} \succ 0$ is built into the third term above.

The $\mathcal{GH}_2$ norm The $\mathcal{GH}_2$ norm, also known as the induced $\mathcal{L}_2$–$\mathcal{L}_\infty$ norm, Equation (2.27), for the system Equation (2.55) is defined as:

$$\|\mathbf{G}\|_g = \sup_{0 < \|\mathbf{w}\|_2 < \infty} \frac{\|\mathbf{z}\|_\infty}{\|\mathbf{w}\|_2}, \text{ with } \mathbf{x}(0) = \mathbf{0}. \tag{2.76}$$

An upper bound on the $\mathcal{GH}_2$ norm, $\|\mathbf{G}\|_g < \nu$, can be found as an LMI optimisation problem in ν, with free matrix variable $\mathbf{P}$ (Wang and Wilson 2001):

$$\mathbf{D} = \mathbf{0}, \quad \begin{bmatrix} \mathbf{A}^\mathsf{T}\mathbf{P} + \mathbf{P}\mathbf{A} & \mathbf{P}\mathbf{B} \\ \mathbf{B}^\mathsf{T}\mathbf{P} & -\nu\mathbf{I} \end{bmatrix} \prec 0, \text{ and } \begin{bmatrix} \mathbf{P} & \mathbf{C}^\mathsf{T} \\ \mathbf{C} & \nu\mathbf{I} \end{bmatrix} \succ 0. \tag{2.77}$$

As with the $\mathcal{H}_2$ norm, $\mathbf{D} = 0$ is required for the $\mathcal{GH}_2$ norm to be finite, and the requirement that $\mathbf{P} \succ 0$ is built into the third term above.

The $\mathcal{L}_\infty$ induced norm The $\mathcal{L}_\infty$ induced norm, Equation (2.26), for the system in Equation (2.55) is given by:

$$\|\mathbf{G}\|_{\mathcal{L}_\infty} = \sup_{0 < \|\mathbf{w}\|_\infty < \infty} \frac{\|\mathbf{z}\|_\infty}{\|\mathbf{w}\|_\infty}, \text{ with } \mathbf{x}(0) = \mathbf{0}. \tag{2.78}$$

An upper bound on the $\mathcal{L}_\infty$ induced norm, $\|\mathbf{G}\|_{\mathcal{L}_\infty} < \gamma$, can be represented as an LMI optimisation problem. Optimising for γ, with free

matrix variable $\mathbf{P}$, and free scalar variables μ and λ, the LMIs are (Scherer and Weiland 2004):

$$\mu > 0, \ \gamma > 0, \ \begin{bmatrix} \mathbf{A}^{\mathrm{T}}\mathbf{P} + \mathbf{P}\mathbf{A} + \lambda\mathbf{P} & \mathbf{P}\mathbf{B} \\ \mathbf{B}^{\mathrm{T}}\mathbf{P} & -\mu\mathbf{I} \end{bmatrix} \prec 0, \text{ and}$$

$$\begin{bmatrix} \lambda\mathbf{P} & 0 & \mathbf{C}^{\mathrm{T}} \\ 0 & (\gamma - \mu)\mathbf{I} & \mathbf{D}^{\mathrm{T}} \\ \mathbf{C} & \mathbf{D} & \gamma\mathbf{I} \end{bmatrix} \succ 0. \tag{2.79}$$

Notice that these equations are not linear in the variables due to $\lambda\mathbf{P}$ in the last matrix above. Choosing a fixed value for λ will return an upper bound on the $\mathcal{L}_1$ norm, however it is unlikely to be close to the true $\mathcal{L}_1$ norm. Scherer and Weiland (2004) state that in practise, performing a line search over λ to minimise γ usually provides good results.

2.3.4 From analysis to control synthesis

A general procedure for converting the performance analysis LMIs presented above into controller synthesis LMIs was first proposed by Masubuchi et al. (1998), and the form presented here largely comes from Scherer (2000).

For the generalised control problem as presented in Equation (2.6):

$$\mathbf{P} = \left[\begin{array}{c|c|c} \mathbf{A} & \mathbf{B}_j & \mathbf{B} \\ \hline \mathbf{C}_j & \mathbf{D}_j & \mathbf{E}_j \\ \hline \mathbf{C} & \mathbf{F}_j & \mathbf{0} \end{array} \right], \tag{2.80}$$

applying the feedback controller:

$$\mathbf{K} = \left[\begin{array}{c|c} \mathbf{A}_c & \mathbf{B}_c \\ \hline \mathbf{C}_c & \mathbf{D}_c \end{array} \right], \tag{2.81}$$

yields the closed loop system:

$$\mathcal{G}_{cl} = \left[\begin{array}{c|c} \mathcal{A} & \mathcal{B}_j \\ \hline \mathcal{C}_j & \mathcal{D}_j \end{array} \right]. \tag{2.82}$$

If viewing the controller parameters as variables, and using the closed-loop matrices instead of the open-loop matrices in the analysis LMIs

above (also replacing $\mathbf{P}$ with its closed loop equivalent, $\mathcal{X}$), the LMIs are no longer linear, and hence cannot be solved directly.

Instead, a linearising transformation is applied to the controller matrices from Equation (2.7) and the closed loop Lyapunov matrix, $\mathcal{X}$, to a new set of variables (following the notation of Scherer (2000)):

$$\left(\mathcal{X}, \begin{bmatrix} \mathbf{A}_c & \mathbf{B}_c \\ \mathbf{C}_c & \mathbf{D}_c \end{bmatrix} \right) \mapsto \left(\mathbf{X}, \mathbf{Y}, \begin{bmatrix} \mathbf{K} & \mathbf{L} \\ \mathbf{M} & \mathbf{N} \end{bmatrix} \right). \tag{2.83}$$

The new LMI variables defined as:

$$\tilde{\mathbf{X}} = \begin{bmatrix} \mathbf{Y} & \mathbf{I} \\ \mathbf{I} & \mathbf{X} \end{bmatrix}, \text{ and} \tag{2.84}$$

$$\left[\begin{array}{c|c} \tilde{\mathbf{A}} & \tilde{\mathbf{B}}_j \\ \hline \tilde{\mathbf{C}}_j & \tilde{\mathbf{D}}_j \end{array} \right] = \left[\begin{array}{cc|c} \mathbf{AY} + \mathbf{BM} & \mathbf{A} + \mathbf{BNC} & \mathbf{B}_j + \mathbf{BNF}_j \\ \mathbf{K} & \mathbf{XA} + \mathbf{LC} & \mathbf{XB}_j + \mathbf{LF}_j \\ \hline \mathbf{C}_j \mathbf{Y} + \mathbf{E}_j \mathbf{M} & \mathbf{C}_j + \mathbf{E}_j \mathbf{NC} & \mathbf{D}_j + \mathbf{E}_j \mathbf{NF}_j \end{array} \right], \tag{2.85}$$

are linear in the transformed controller variables and the transformed Lyapunov matrices. Under a transformation with the variable $\mathcal{Y}$, the closed-loop matrices in the LMIs can be mapped to the new variables

$$\mathcal{Y}^{\mathrm{T}} \mathcal{X} \mathcal{Y} \mapsto \tilde{\mathbf{X}}, \text{ and} \tag{2.86}$$

$$\begin{bmatrix} \mathcal{Y}^{\mathrm{T}}(\mathcal{X}\mathcal{A})\mathcal{Y} & \mathcal{Y}^{\mathrm{T}}(\mathcal{X}\mathcal{B}_j) \\ \mathcal{C}_j \mathcal{Y} & \mathcal{D}_j \end{bmatrix} \mapsto \begin{bmatrix} \tilde{\mathbf{A}} & \tilde{\mathbf{B}} \\ \tilde{\mathbf{C}} & \tilde{\mathbf{D}} \end{bmatrix}. \tag{2.87}$$

Performing these transformations on any of the analysis LMIs outlined above generates controller synthesis LMIs, which can be solved as per the analysis LMIs. Once a feasible solution is found, the controller can be reconstructed by reversing the transformation, firstly by finding the nonsingular decomposition

$$\mathbf{U}\mathbf{V}^{\mathrm{T}} = \mathbf{I} - \mathbf{XY}, \tag{2.88}$$

and solving (Scherer 2000)

$$\begin{bmatrix} \mathbf{K} & \mathbf{L} \\ \mathbf{M} & \mathbf{N} \end{bmatrix} = \begin{bmatrix} \mathbf{U} & \mathbf{XB} \\ \mathbf{0} & \mathbf{I} \end{bmatrix} \begin{bmatrix} \mathbf{A}_c & \mathbf{B}_c \\ \mathbf{C}_c & \mathbf{D}_c \end{bmatrix} \begin{bmatrix} \mathbf{V}^{\mathrm{T}} & \mathbf{0} \\ \mathbf{CY} & \mathbf{I} \end{bmatrix} + \begin{bmatrix} \mathbf{XAY} & \mathbf{0} \\ \mathbf{0} & \mathbf{0} \end{bmatrix} \tag{2.89}$$

for the controller variables. The closed-loop Lyapunov matrix can be found by solving

$$\begin{bmatrix} \mathbf{Y} & \mathbf{V} \\ \mathbf{I} & \mathbf{0} \end{bmatrix} \mathcal{X} = \begin{bmatrix} \mathbf{I} & \mathbf{0} \\ \mathbf{X} & \mathbf{U} \end{bmatrix}. \tag{2.90}$$

In the specialised case of state feedback control with a static controller, the transformation variables become (Scherer 2000):

$$\tilde{\mathbf{X}} = \mathbf{Y}, \text{ and} \tag{2.91}$$

$$\left[\begin{array}{c|c} \tilde{\mathbf{A}} & \tilde{\mathbf{B}}_j \\ \hline \tilde{\mathbf{C}}_j & \tilde{\mathbf{D}}_j \end{array} \right] = \left[\begin{array}{c|c} \mathbf{AY} + \mathbf{BM} & \mathbf{B}_j \\ \hline \mathbf{C}_j\mathbf{Y} + \mathbf{E}_j\mathbf{M} & \mathbf{D}_j \end{array} \right]. \tag{2.92}$$

The controller gains can be reconstructed using

$$\mathbf{D}_c = \mathbf{MY}^{-1}, \tag{2.93}$$

and the closed-loop Lyapunov matrix is

$$\mathcal{X} = \mathbf{Y}^{-1}. \tag{2.94}$$

2.3.5 Reduced order controller synthesis

Reduced order controllers can be directly synthesised using the controller reconstruction discussed above, with the inclusion of some rank constraints using recent numerical methods such as those given by Orsi et al. (2006).

During the solving of the synthesis LMI, if a valid solution can be found such that

$$\text{rank} \begin{bmatrix} \mathbf{X} & \mathbf{I} \\ \mathbf{I} & \mathbf{Y} \end{bmatrix} \leq n + n_c \tag{2.95}$$

where:

n is the order (number of states) of the generalised control problem, and

n_c is the desired order of the controller,

then $\mathbf{U}$ and $\mathbf{V}$ can be constructed as non-square of size $n \times n_c$ from

$$\mathbf{UV}^\mathrm{T} = \mathbf{I} - \mathbf{XY}. \tag{2.96}$$

Possible methods to construct these variables include the Singular Value Decomposition and the Eigenvalue decomposition, with the removal of the zero (and near-zero) singular values or eigenvalues.

The controller variables can be reconstructed using the solution to Equation (2.89)

$$\left[\begin{array}{c|c} \mathbf{A}_c & \mathbf{B}_c \\ \hline \mathbf{C}_c & \mathbf{D}_c \end{array}\right] = \left[\begin{array}{c|c} \mathbf{U} & \mathbf{XB} \\ \hline \mathbf{0} & \mathbf{I} \end{array}\right] \Big\backslash \left[\begin{array}{c|c} \mathbf{K} - \mathbf{XAY} & \mathbf{L} \\ \hline \mathbf{M} & \mathbf{N} \end{array}\right] \Big/ \left[\begin{array}{c|c} \mathbf{V}^{\mathrm{T}} & \mathbf{0} \\ \hline \mathbf{CY} & \mathbf{I} \end{array}\right] \tag{2.97}$$

where \ and / denote left and right matrix division respectively, which is more numerically stable than multiplying by matrix inverses.

Directly synthesising a reduced order controller can be useful in cases such as a near-optimal $\mathcal{H}_\infty$ that may tend to push poles and zeros too close together.

2.3.6 Linear Parameter Varying systems

Linear Parameter Varying (LPV) systems are nonlinear systems that can be considered linear for a particular value of a time-varying parameter vector. That is, for the time varying parameter vector, $\mathbf{p}(t)$, the state-space matrices of a LPV system are fixed functions of the parameter (Apkarian et al. 1995):

$$\mathbf{G}(\mathbf{p}(t)) = \left[\begin{array}{c|c} \mathbf{A}(\mathbf{p}(t)) & \mathbf{B}(\mathbf{p}(t)) \\ \hline \mathbf{C}(\mathbf{p}(t)) & \mathbf{D}(\mathbf{p}(t)) \end{array}\right]. \tag{2.98}$$

Linear Matrix Inequalities allow for the powerful and mature linear control methods outlined previously to be used in controller synthesis for LPV plants, while still providing performance guarantees on the controlled system. From henceforth, the parameter s time dependence will be implicit.

Consider the LPV generalised control problem

$$\mathbf{P}(\mathbf{p}) = \left[\begin{array}{c|c|c} \mathbf{A}(\mathbf{p}) & \mathbf{B}_j(\mathbf{p}) & \mathbf{B}(\mathbf{p}) \\ \hline \mathbf{C}_j(\mathbf{p}) & \mathbf{D}_j(\mathbf{p}) & \mathbf{E}_j(\mathbf{p}) \\ \hline \mathbf{C}(\mathbf{p}) & \mathbf{F}_j(\mathbf{p}) & \mathbf{0} \end{array}\right] \tag{2.99}$$

with $\mathbf{p}$ bound:

$$p_i \in [\underline{p}_i, \bar{p}_i], \tag{2.100}$$

and the goal of finding a LPV controller to minimise an arbitrary performance objective. The LPV controller can be synthesised in several different ways.

Affine LPV controller   If the plant's dependence on $\mathbf{p}$ is affine, and the matrices $\mathbf{B}$, $\mathbf{C}$, $\mathbf{E}$, and $\mathbf{F}$ are all parameter independent:

$$
\left[
\begin{array}{cc|c}
\mathbf{A(p)} & \mathbf{B}_j\mathbf{(p)} & \mathbf{B} \\
\hline
\mathbf{C}_j\mathbf{(p)} & \mathbf{D}_j\mathbf{(p)} & \mathbf{E}_j \\
\hline
\mathbf{C} & \mathbf{F}_j & \mathbf{0}
\end{array}
\right]
=
\left[
\begin{array}{cc|c}
\mathbf{A}_{p0} & \mathbf{B}_{j,p0} & \mathbf{B}_{p0} \\
\hline
\mathbf{C}_{j,p0} & \mathbf{D}_{j,p0} & \mathbf{E}_{j,p0} \\
\hline
\mathbf{C}_{p0} & \mathbf{F}_{j,p0} & \mathbf{0}
\end{array}
\right]
+ \sum_{i=1}^{m}
\left[
\begin{array}{cc|c}
\mathbf{A}_{pi} & \mathbf{B}_{j,pi} & \mathbf{0} \\
\hline
\mathbf{C}_{j,pi} & \mathbf{D}_{j,pi} & \mathbf{0} \\
\hline
\mathbf{0} & \mathbf{0} & \mathbf{0}
\end{array}
\right] p_i,
\tag{2.101}
$$

then a controller that has the same parameter dependence as the plant can be synthesised by keeping the transformed Lyapunov matrices, $\mathbf{X}$ and $\mathbf{Y}$, parameter independent, and letting the transformed controller matrices take the same affine parameter dependence as the plant:

$$
\left[
\begin{array}{c|c}
\mathbf{K(p)} & \mathbf{L(p)} \\
\hline
\mathbf{M(p)} & \mathbf{N(p)}
\end{array}
\right]
=
\left[
\begin{array}{c|c}
\mathbf{K}_{p0} & \mathbf{L}_{p0} \\
\hline
\mathbf{M}_{p0} & \mathbf{N}_{p0}
\end{array}
\right]
+ \sum_{i=1}^{m}
\left[
\begin{array}{c|c}
\mathbf{K}_{pi} & \mathbf{L}_{pi} \\
\hline
\mathbf{M}_{pi} & \mathbf{N}_{pi}
\end{array}
\right] p_i.
\tag{2.102}
$$

Using the same transformations above, the analysis LMIs are converted to synthesis LMIs, and solved at each vertex of the hypercube formed by the parameter limits, Equation (2.100), simultaneously. The LPV controller is then reconstructed by finding the nonsingular decomposition, Equation (2.88), and by solving Equation (2.89). The resulting controller will have an affine parameter dependence on $\mathbf{p}$, and will provide a guarantee of the performance anywhere inside the parameter hypercube.

General parameter dependence   When the temporal derivative of the parameter variations, $\mathbf{q} = \mathbf{p}$, are bound:

$$
q_i \in [\underline{q}_i, \bar{q}_i],
\tag{2.103}
$$

for the generalised LPV control problem in Equation (2.99), a less conservative controller can be synthesised by including a parameter dependent Lyapunov matrix. For continuous systems this can be done by replacing every instance of

$$
\mathbf{PA} + \mathbf{A}^\mathrm{T}\mathbf{P}
\tag{2.104}
$$

in the analysis LMIs given above in Section 2.3.3 with

$$
\partial\mathbf{P} + \mathbf{PA} + \mathbf{A}^\mathrm{T}\mathbf{P},
\tag{2.105}
$$

using the notation

$$\frac{d\mathbf{P}(\mathbf{p})}{dt} = \sum_{j=1}^{m} \frac{\partial \mathbf{P}}{\partial p_j} q_j = \partial \mathbf{P}(\mathbf{p}, \mathbf{q}), \qquad (2.106)$$

which can be found from the Lyapunov stability example when taking the derivative of the storage function, Equation (2.51), when $\mathbf{P}$ is time-dependent.

Under the same transformation from analysis to synthesis LMIs, Equation (2.87) (Scherer and Weiland 2004),

$$\mathcal{Y}^{\mathrm{T}} \left(\partial \mathcal{X}(\mathbf{p}, \mathbf{q}) + \mathcal{X}(\mathbf{p})\mathcal{A}(\mathbf{p}) + \mathcal{A}^{\mathrm{T}}(\mathbf{p})\mathcal{X}(\mathbf{p}) \right) \mathcal{Y}$$
$$= \left[\begin{array}{c} -\partial \mathbf{Y}(\mathbf{p}, \mathbf{q}) + \mathrm{sym}\left(\mathbf{A}(\mathbf{p})\mathbf{Y}(\mathbf{p}) + \mathbf{B}(\mathbf{p})\mathbf{M}(\mathbf{p})\right) \\ \mathbf{K}(\mathbf{p}, \mathbf{q}) + (\mathbf{A}(\mathbf{p}) + \mathbf{B}(\mathbf{p})\mathbf{N}(\mathbf{p})\mathbf{C}(\mathbf{p}))^{\mathrm{T}} \end{array} \right. \cdots$$
$$\left. \begin{array}{c} \mathbf{A}(\mathbf{p}) + \mathbf{B}(\mathbf{p})\mathbf{N}(\mathbf{p})\mathbf{C}(\mathbf{p}) + \mathbf{K}^{\mathrm{T}}(\mathbf{p}, \mathbf{q}) \\ \partial \mathbf{X}(\mathbf{p}, \mathbf{q}) + \mathrm{sym}\left(\mathbf{X}(\mathbf{p})\mathbf{A}(\mathbf{p}) + \mathbf{L}(\mathbf{p})\mathbf{C}(\mathbf{p})\right) \end{array} \right], \quad (2.107)$$

the LMIs can be rendered affine in the parameter dependent transformed controller variables and Lyapunov matrices. Notice the dependence of $\mathbf{K}$ on both $\mathbf{p}$ and $\mathbf{q}$, this is a result of the transformation and takes the structure (Scherer and Weiland 2004)

$$\mathbf{K}(\mathbf{p}, \mathbf{q}) = \mathbf{K}_{q0}(\mathbf{p}) + \sum_{i=1}^{m} \mathbf{K}_{qi}(\mathbf{p}) q_i. \qquad (2.108)$$

If the parameter dependence is affine, then the synthesis LMIs can be solved at the vertices of the hypercube formed by $\mathbf{p}$ and $\mathbf{q}$ simultaneously before reconstructing the controller.

When the parameter dependance is general, the synthesis LMIs are no longer convex. However, by choosing appropriate basis functions for the parameters, and by constructing a grid across the true parameter trajectory, the general parameter dependence can be reduced to a finite number of LMIs and solved simultaneously at the grid points and the extreme values of $\mathbf{q}$. In this case, the controller can no longer provide a guarantee of performance between the grid points but provides a good approximation so long as the grid is sufficiently dense. To ensure the grid is sufficiently dense, it has been suggested that after controller synthesis and reconstruction, the performance results should be verified using the

closed-loop analysis LMIs on a finer grid (Apkarian and Adams 1998, and Cox 2003). Should verification fail, the synthesis grid density should be increased and the process repeated until the verification passes.

Once a valid solution is found to the synthesis LMI problem, the controller parameters can be reconstructed in the same fashion as given in Section 2.3.4, firstly by finding non-singular $\mathbf{U}(\mathbf{p})$ and $\mathbf{V}(\mathbf{p})$ such that

$$\mathbf{U}(\mathbf{p})\mathbf{V}^{\mathrm{T}}(\mathbf{p}) = \mathbf{I} - \mathbf{X}(\mathbf{p})\mathbf{Y}(\mathbf{p}), \tag{2.109}$$

and then solving for the parameters (Scherer and Weiland 2004):

$$\begin{bmatrix} \mathbf{A}_c(\mathbf{p},\mathbf{q}) & \mathbf{B}_c(\mathbf{p}) \\ \mathbf{C}_c(\mathbf{p}) & \mathbf{D}_c(\mathbf{p}) \end{bmatrix} = \begin{bmatrix} \mathbf{U}(\mathbf{p}) & \mathbf{X}(\mathbf{p})\mathbf{B}(\mathbf{p}) \\ \mathbf{0} & \mathbf{I} \end{bmatrix}$$

$$\Big\backslash \begin{bmatrix} \mathbf{K}(\mathbf{p},\mathbf{q}) - \mathbf{X}(\mathbf{p})\mathbf{A}(\mathbf{p})\mathbf{Y}(\mathbf{p}) - [\partial\mathbf{X}(\mathbf{p},\mathbf{q})\mathbf{Y}(\mathbf{p}) + \partial\mathbf{U}(\mathbf{p},\mathbf{q})\mathbf{V}^{\mathrm{T}}] & \mathbf{L}(\mathbf{p}) \\ \mathbf{M}(\mathbf{p}) & \mathbf{N}(\mathbf{p}) \end{bmatrix}$$

$$\Big/ \begin{bmatrix} \mathbf{V}^{\mathrm{T}}(\mathbf{p}) & \mathbf{0} \\ \mathbf{C}(\mathbf{p})\mathbf{Y}(\mathbf{p}) & \mathbf{I} \end{bmatrix} \tag{2.110}$$

where $\backslash$ and $/$ denote left and right matrix division respectively, and noting that when convenient

$$[\partial\mathbf{X}(\mathbf{p},\mathbf{q})\mathbf{Y}(\mathbf{p}) + \partial\mathbf{U}(\mathbf{p},\mathbf{q})\mathbf{V}^{\mathrm{T}}] \tag{2.111}$$

from Equation (2.110) can be replaced with

$$-[\mathbf{X}(\mathbf{p})\partial\mathbf{Y}(\mathbf{p},\mathbf{q}) + \mathbf{U}(\mathbf{p})\partial\mathbf{V}^{\mathrm{T}}(\mathbf{p},\mathbf{q})]. \tag{2.112}$$

Apkarian and Adams (1998) state that a controller which depends upon the derivative of a parameter is often not practically valid. One way of preventing the controller depending upon $\mathbf{q}$ is to let either $\mathbf{X}$ or $\mathbf{Y}$ be parameter independent, with the best choice between them depending upon the particular problem.

2.4 Aeroelasticity

Aeroelasticity is a broad term that describes the often complex interactions between aerodynamics and structural mechanics. In this section, a brief overview of aeroelastic theory is presented, focussing on the quasi-steady model that will be used throughout this work. A good resource for further reading is Dowell et al. (2004).

2.4.1 Typical section aerofoil

A simple aeroelastic model often used is the typical section aerofoil, which consists of a two-dimensional flat plate mounted parallel to a uniform freestream airflow via a torsional spring, as shown in Figure 2.4.

A variant of this typical section aerofoil that includes a trailing-edge control surface and a translational spring is shown in Figure 2.5.

The point about which the wing can twist, which is the location of the torsional spring in Figures 2.4 and 2.5, is known as the elastic axis, and is located at the distance x_0 from the leading-edge. The elastic axis is separate from the aerodynamic centre.

Using this simple mechanical model, several static and dynamic aeroelastic phenomena can be explained.

2.4.2 Static aeroelasticiy

Two static aeroelastic phenomena phenomena that will be quickly addressed are divergence and control reversal.

2.4.2.1 Divergence

Divergence is a static aeroelastic phenomena that occurs when the aerodynamic moment acting at the elastic axis causes the wing to twist until it structurally fails. A simple derivation of the *divergence airspeed*, the point at which the pitch angle asymptotes versus airspeed, can be performed using the steady aerodynamic model for moment:

$$M = \tfrac{1}{2}\rho U^2 A c C_{m_{\alpha,\text{eff.}}} \alpha \qquad (2.113)$$
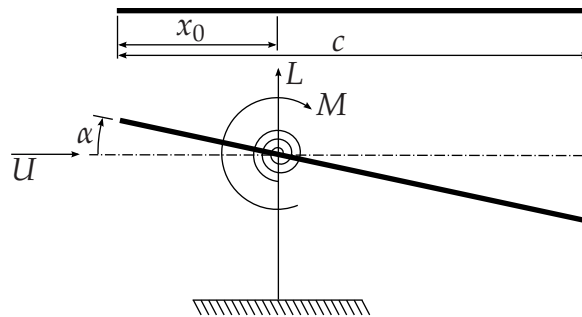
Figure 2.4: Typical section aerofoil model.
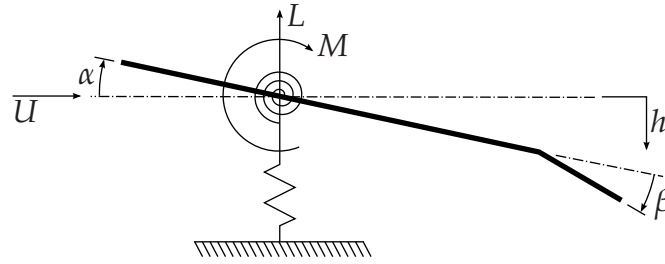
Figure 2.5: A variant of the typical section aerofoil model that includes a trailing-edge control surface and a translational spring.

where:

α is the pitching angle,

ρ is the freestream air density,

U is the freestream airspeed,

A is the aerofoil planform area,

c is the chord length of the aerofoil,

$C_{m_{\alpha,\text{eff.}}} = \frac{\partial C_m}{\partial \alpha} - (\frac{c}{4} - x_0)C_{l_\alpha}$,

C_m is the coefficient of moment at the aerodynamic centre,

$C_{l_\alpha} = \frac{\partial C_l}{\partial \alpha}$, and

C_l is the coefficient of lift at the aerodynamic centre.

The equation of reaction moment from the torsional spring is:

$$M_k = k_\alpha \alpha \tag{2.114}$$

where:

k_α is the torsional spring stiffness.

At equilibrium the two moments are equal, so equating Equations (2.113) and (2.114), and rearranging to find the pitching angle yields

$$\alpha = \frac{2}{\rho U^2 A c C_{m_{\alpha,\text{eff.}}} - 2k_\alpha}. \tag{2.115}$$

Solving for the asymptote (when the denominator equals zero) yields the divergence airspeed of

$$U_D = \pm\sqrt{\frac{2k_\alpha}{\rho A c C_{m_{\alpha,\text{eff.}}}}}. \tag{2.116}$$

It is worth noting that in practice various nonlinear effects and structural limitations will cause the true divergence airspeed to differ from this simple calculation.

2.4.2.2 Control reversal

Control reversal occurs when aeroelastic effects cause the total lift generated by actuating the control surface to be in the opposite direction to that generated by the control surface. A simple derivation for the conditions of control reversal are given below.

The aerodynamic moment at the elastic axis due to both the wing and the trailing-edge control surface is

$$M = \tfrac{1}{2}\rho U^2 Ac(C_{m_{\alpha,\text{eff.}}}\alpha + C_{m_{\beta,\text{eff.}}}\beta) \tag{2.117}$$

where:

$C_{m_{\beta,\text{eff.}}} = \frac{\partial C_m}{\partial \beta} - (\frac{c}{4} - x_0)C_{l_\beta}$, and

$C_{l_\beta} = \frac{\partial C_l}{\partial \beta}$.

Equating this with the reaction moment from Equation (2.114), and solving for α gives:

$$\alpha = \frac{\rho U^2 Ac C_{m_{\beta,\text{eff.}}}\beta}{2k_\alpha - \rho U^2 Ac C_{m_{\alpha,\text{eff.}}}}. \tag{2.118}$$

Defining the nominal lift due to the trailing-edge control surface as

$$L_r = \tfrac{1}{2}\rho U^2 AC_{l_\beta}\beta, \tag{2.119}$$

and the total lift from the aerofoil and the trailing-edge surface at the elastic axis as

$$L = \tfrac{1}{2}\rho U^2 A(C_{l_\alpha}\alpha + C_{l_\beta}\beta), \tag{2.120}$$

the ratio of lift to nominal lift is L/L_r. Substituting in the equilibrium angle for α from Equation (2.118), the ratio of lift to nominal lift is:

$$\frac{L}{L_r} = 1 + \frac{\rho U^2 Ac C_{m_{\beta,\text{eff.}}}C_{l_\alpha}}{(2k_\alpha - \rho U^2 Ac C_{m_{\alpha,\text{eff.}}})C_{l_\beta}}. \tag{2.121}$$

From this equation it can be seen that the same divergence asymptote, Equation (2.116), is present, as well as a solution to when the lift generated is zero.

$$U_R = \pm\sqrt{\frac{2k_\alpha C_{l_\beta}}{\rho Ac(C_{l_\beta}C_{m_{\alpha,\text{eff.}}} - C_{l_\alpha}C_{m_{\beta,\text{eff.}}})}}. \tag{2.122}$$

An example plot using values from Chapter 4, with the exception of $C_{m_{\alpha,\text{eff.}}}$ which is opposite in sign from that in Chapter 4 as reversal

34

does not occur for the original sign of $C_{m_{\alpha,\text{eff.}}}$, which shows the lift ratio versus airspeed normalised against the divergence airspeed as given in Figure 2.6. It clearly shows the lift generated by the aeroelastic system reversing direction against the nominal lift for airspeeds above U_R.

2.4.3 Dynamic aeroelasticity

Dynamic aeroelasticity refers to aeroelastic effects that occur due to the motion of the aerodynamic body. Several examples of dynamic aeroelastic phenomena are gust loading, limit-cycle oscillations and flutter (Mukhopadhyay 2003). This section will briefly describe the aerodynamic models required for these phenomena, but omit the dynamics as these are treated more thoroughly in Chapter 4.

2.4.3.1 Gust loading

Gust loading refers to the dynamic response of an aerofoil to a gust disturbance. One method of incorporating a gust acting perpendicular to the freestream airspeed, w_G, into an aeroelastic model is as a change in
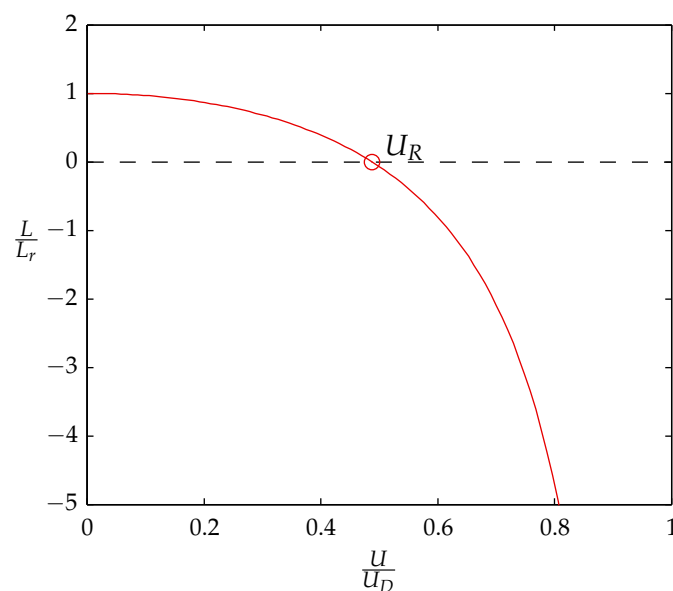
Figure 2.6: Normalised lift versus normalised airspeed. Above U_R the lift generated from the aeroelastic system has reversed direction versus the nominal trailing-edge lift, hence control reversal has occurred.

35

the effective angle of attack, such that (Dowell et al. 2004):

$$L = \tfrac{1}{2}\rho U^2 A C_{l_\alpha}(\alpha + \frac{w_G}{U}), \text{ and} \qquad (2.123)$$

$$M = \tfrac{1}{2}\rho U^2 A c C_{m_{\alpha,\text{eff.}}}(\alpha + \frac{w_G}{U}). \qquad (2.124)$$

Implicit in this formulation is a small-angle approximation that requires $w_G \ll U$.

2.4.3.2 Limit-cycle oscillations and flutter

Flutter is a dynamic aeroelastic instability which is caused by the feedback mechanism between aerofoil movement and aerodynamic forces.

Limit-cycle oscillation is a generic term used to describe oscillations that are bounded by some nonlinear effect. In the context of this work, the term limit-cycle oscillation will be used to describe flutter bounded by a nonlinear torsional stiffness.

The dynamic instability behind flutter and limit-cycle oscillations cannot be modelled using steady aerodynamic theory. Instead, both unsteady and quasi-steady aerodynamic models have been used in the literature to study flutter and limit-cycle oscillations. In this work, only the quasi-steady aerodynamic model is used.

The quasi-steady assumption is (Fung 1955):

> The aerodynamic characteristics of an airfoil whose motion consists of variable linear and angular motions are equal, at any instant in time, to the characteristics of the same airfoil moving with constant linear and angular velocities equal to the actual instantaneous values.

In other words, the aerodynamic characteristics only depend upon the current state of α and h, and not on any previous values.

The equations for the quasi-steady aerodynamic model can be derived from thin aerofoil theory. The aerofoil is replaced with a vortex sheet, of vorticity $\gamma(x)dx$ for $x \in [0, c]$ such that the total lift is given by

$$L = \rho U S \int_0^c \gamma(x)dx, \qquad (2.125)$$

where S is the span of the aerofoil.

By assuming that the vortices are situated along the x axis, the induced y velocity to a first order approximation is

$$v_i(x) = \int_0^c \frac{\gamma(\xi)d\xi}{2\pi(\xi - x)}. \tag{2.126}$$

The fluid velocity over the aerofoil must be tangental to the aerofoil itself, so under small angle approximations ($h \ll U$ and $c\alpha \ll U$), the induced velocities from the vorticity and the aerofoil motion must satisfy:

$$\frac{v_i(x)}{U} = -\alpha - \frac{h}{U} + (x - x_0)\frac{\alpha}{U}. \tag{2.127}$$

After solving for the vorticity distribution which satisfies Equation (2.127) and $\gamma(c) = 0$ (refer to Fung (1955) for the details) the quasi-steady lift coefficient is

$$C_l = C_{l_\alpha}\left(\alpha + \frac{h}{U} + (\tfrac{3}{4}c - x_0)\frac{\alpha}{U}\right), \tag{2.128}$$

which shows that the lift can be calculated from the induced angle of attack at the 3/4–chord point.

The corresponding solution for the aerodynamic moment about the elastic axis is

$$(C_m)_{x_0} = -\frac{c\pi}{8U}\alpha + \left(\frac{x_0}{c} - \tfrac{1}{4}\right)C_l, \tag{2.129}$$

which shows that the lift forces acts at the 1/4–chord point, and includes an extra damping term proportional to the pitching rate.

2.5 Summary

In this chapter some preliminary theory behind controller synthesis, Linear Matrix Inequalities, Linear Parameter Varying systems, static and dynamic aeroelasticity has been presented. This theory provides a base upon which the rest of this work can follow.

3 Literature Review

While the theory relevant to this work has been presented in Chapter 2, this chapter aims to put this work in context with the current state of LMIs in control theory and aeroelasticity control.

3.1 Control theory

The field of modern or optimal control matured in the 1960s, and involved the optimisation of feedback control gains with respect to the states and inputs for Linear Quadratic Regulator (LQR) control, optimisation of observer gains with respect to stochastic disturbances for Kalman filtering, and Linear Quadratic Gaussian (LQG) control combining the two.

A thorough treatment of optimal control is given by Anderson and Moore (1989), which the reader is referred to for more information.

More recently, robust control techniques focussing on minimising the in uence of uncertainty were developed using the $\mathcal{H}_\infty$ norm and μ (structured singular value) analysis. For more thorough treatments, the reader is referred to the texts by Zhou et al. (1996), and Skogestad and Postlethwaite (2005).

3.1.1 Linear Matrix Inequalities

Both Linear Matrix Inequalities (LMIs) for dynamical analysis and convex analysis techniques have been studied for over a century. LMIs date back to the work on Lyapunov stability, presented in Section 2.3.3. However, it was not until the early 1980s that numerical convex optimisation techniques were used to solve dynamical analysis problems.

During the late 1980s, efficient interior-point optimisation methods emerged, allowing for large optimisation problems to be solved quickly. These have caused a resurgence of interest in using LMIs for control analysis and synthesis.

The modern history of LMIs in control theory has largely emerged as individual performance specifications being represented in LMI form. A collection of these were published in one of the first texts written on the use of LMIs in control theory by Boyd et al. (1994).

Gahinet and Apkarian (1994) presented one of the first instances of $\mathcal{H}_\infty$ controller synthesis using LMIs, and showed how it related to the traditional method of solving algebraic Riccati equations.

For the construction of Linear Parameter Varying (LPV) controllers, Apkarian et al. (1995) presented both continuous and discrete $\mathcal{H}_\infty$ (technically induced $\mathcal{L}_2$) synthesis LMIs, and used them to solve for a self-scheduling controller. In their work, the plant parameter dependence was affine, and the Lyapunov matrix was fixed, which preserves convexity and allows for arbitrary parameter variations, but restricts the range over which the controller can schedule.

Gahinet et al. (1996) presented $\mathcal{H}_\infty$ (technically induced $\mathcal{L}_2$) analysis LMIs for an affinely parameter dependent plant using an affinely parameter dependent Lyapunov matrix while still preserving convexity. Unfortunately, to the author s knowledge, this has not been able to be used for synthesis, due to the inversion required for the transformed Lyapunov matrices.

A mixed $\mathcal{H}_\infty/\mathcal{H}_2$ (and mixed $\mathcal{H}_\infty/\mathcal{G}\mathcal{H}_2$) LMI control synthesis method was presented by Scherer (1996). Using a variation of the standard $\mathcal{H}_\infty$ control synthesis framework, the corresponding $\mathcal{H}_2$ Lyapunov equation solution is implicitly included, hence only the $\mathcal{H}_2$ performance term needed to be included to solve the mixed problem. Furthermore, Scherer (1996) also presented a linearising transformation on the controller variables, a method of synthesising a reduced-order controller, even though the numerical tools to achieve it did not exist at the time, and results for LPV controller synthesis.

A method for multiobjective controller synthesis was then presented by Scherer et al. (1997). For a Linear Time Invariant (LTI) plant, any combination of performance objective can be achieved through the use of a common Lyapunov matrix when solving the different performance

LMIs simultaneously.

Apkarian and Adams (1998) presented an LPV induced $\mathcal{L}_2$ norm controller for systems with general parameter dependence. They suggest that in general, measuring the derivative of the parameter variations is not practical, so using a table they outlined which combinations of parameter dependent and parameter independent transformed Lyapunov matrices are valid, an adapted form of which is shown in Table 3.1.

Apkarian and Adams (1998) also provide a guide for the gridding process. They suggest constructing a grid across the true parameter space, synthesising the controller over all of the grid vertices simultaneously, then verify the performance index using the closed-loop system on a finer grid. Should the verification fail, the synthesis grid density should be increased.

A unified framework for LMI controller synthesis was presented by Masubuchi et al. (1998). This involved the change of controller variables to render the synthesis LMIs affine in all of the variables, and showed that it applied to a large class of LMIs, including all of the typically used performance objectives in both the continuous and discrete domains. This work marks a point of maturity in the use of LMIs for control theory, as a generalised picture of how to create synthesis LMIs for arbitrary performance specifications emerged.

Methods for reducing different types of nonlinear parameter dependent functions, including ones with polynomial parameter dependence, to a finite set of LMIs was presented by Apkarian and Tuan (2000). While these methods preserve convexity, it is at the expense of conservatism, meaning the resulting controller will be suboptimal.

Table 3.1: Practical validity of LPV controllers adapted from Apkarian and Adams (1998), with the variables as given in Section 2.3.6.

		Practically valid?
$q = \mathbf{0}$	$\mathbf{X} := \mathbf{X}(\mathbf{p}), \ \mathbf{Y} := \mathbf{Y}(\mathbf{p})$	yes
q bounded	$\mathbf{X} := \mathbf{X}(\mathbf{p}), \ \mathbf{Y} := \mathbf{Y}(\mathbf{p})$	no
q bounded	$\mathbf{X} := \mathbf{X}(\mathbf{p}), \ \mathbf{Y} := \mathbf{Y}$	yes
q bounded	$\mathbf{X} := \mathbf{X}, \ \mathbf{Y} := \mathbf{Y}(\mathbf{p})$	yes
q unbounded	$\mathbf{X} := \mathbf{X}, \ \mathbf{Y} := \mathbf{Y}$	yes

A method of synthesising a Linear Fractional Representation (LFR) controller with a mixed $\mathcal{H}_\infty/\mathcal{H}_2$ performance objective was presented in Apkarian et al. (2000). The method they presented only utilised diagonal LFR multipliers, omitting the off-diagonal terms such that the multiplier, in the notation of this work, would be

$$\mathbf{P} = \begin{bmatrix} \mathbf{Q} & 0 \\ 0 & \mathbf{R} \end{bmatrix}. \tag{3.1}$$

Around the same time, a book chapter contribution by Scherer (2000) presented a more general method synthesising an LFR controller using full-block LFR multipliers, such that

$$\mathbf{P} = \begin{bmatrix} \mathbf{Q} & \mathbf{S} \\ \mathbf{S}^\mathrm{T} & \mathbf{R} \end{bmatrix}, \tag{3.2}$$

and did it in the general framework of a quadratic performance problem. This allowed the use of arbitrary performance specifications, including mixed performance if desired, in both the continuous and discrete domains. The book chapter was followed up by Scherer (2001), where the method for reconstructing the extended multiplier was given in more detail.

A tutorial on LMIs and bilinear matrix inequalities was presented by VanAntwerp and Braatz (2000). This work included a comprehensive list of LMI formulations for many different control problems, as well as other important results, such as the Schur complement lemma.

Hiret et al. (2001) presented a LFR $\mathcal{H}_\infty$ loop shaping controller for a missile autopilot, constructed using LMIs. This is similar to the work presented later in Chapter 7, with the significant exceptions being the use of single multiplier matrix, equivalent to

$$\mathbf{P} = \begin{bmatrix} \mathbf{Q} & 0 \\ 0 & \mathbf{Q}^{-1} \end{bmatrix} \tag{3.3}$$

in the notation of this work, and the forcing of the controller LFR scheduling, $\Delta_c(\Delta)$, to be the same as Δ. These restrictions employed by Hiret et al. (2001) result in a controller that is conservative compared to that produced in Chapter 7.

As previously mentioned, it was the progress in numerical LMI solvers that renewed the interest in using LMIs for control synthesis problems. Of particular interest for this work are several solvers written to interface directly with Matlab, the popular SeDuMi (Sturm 1999), and the preferred solver for this current work, SDPT3 (Toh et al. 1999). The author has found that SDPT3 provides a more numerically reliable solution when the LMI optimisation problem is close to optimal.

With the release of a Matlab toolbox called YALMIP (Löfberg 2004), it became much simpler to quickly create and solve LMI problems. YALMIP provides a fundamental matrix variable type, which can be manipulated using standard operators. This allows for LMIs to be constructed algebraically, rather than having to be explicitly constructed. YALMIP also abstracts the solving process, allowing for the easy changing or testing of multiple solvers.

Finally of note, Orsi et al. (2006) presented a method of solving rank constraints numerically, which is useful for the synthesis of reduced-order controllers. He produced a Matlab solver called LMIRank, which can be used with YALMIP.

3.2 Aeroelasticity

One of the first descriptions of aeroelasticity as a field was given by Collar (1946), where he describes the forces involved in aeroelasticity to be combinations of aerodynamic, elastic and inertial forces. Using what is now known as a Collar diagram, Figure 3.1, he described how various different aeroelastic phenomena occur as interactions of these forces. As knowledge of aeroelasticity has progressed, Collar diagrams have been extended many times to include such things as thermal effects and aeroelastic control systems.

Before the term aeroelasticity was coined, there was already much research into these aeroelastic phenomena. One example of such is the theory of aerodynamic instability and utter in two degrees-of-freedom by Theodorsen (1934), which he followed up with experiments (Theodorsen and Garrick 1940), and calculations in three degrees-of-freedom (Theodorsen and Garrick 1941).

A thorough treatment of aeroelasticity is given by Fung (1955), in particular the quasi-steady aerodynamic model, used extensively throughout
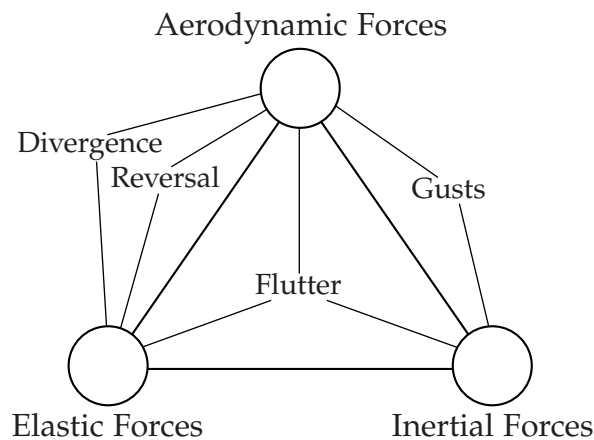
Figure 3.1: An example of a Collar diagram, showing how many aeroelastic phenomena relate to interactions of aerodynamic, elastic and inertial forces.

this work, for a thin two degree-of-freedom aerofoil is presented.

Another thorough text on aeroelasticity is given by Dowell et al. (2004), which after several editions now has contributions on a wide range of aeroelastic topics. The section on LPV LMI control, an extract of the work by Cox (2003), is particularly relevant to this work, and will be revisited later in Section 3.2.1.

An excellent historical perspective of aeroelasticity and its control has been presented by Mukhopadhyay (2003). In it, he mentions the Benchmark Active Control Technologies (BACT) two degree-of-freedom aeroelastic system, shown in Figure 3.2, located at the NASA Langley Research Centre.

The BACT is a NACA 0012 aerofoil mounted on a platform that allows it to pitch and plunge. It has a trailing-edge control surface, as well as upper- and lower-surface spoilers, all independently hydraulically actuated. The primary sensors used for feedback control are pressure transducers, and accelerometers located in each corner of the wing.

The goal of the BACT system was to measure unsteady transonic aerodynamic data, and to act as a test-bed for active control techniques. The BACT system has been modelled using several techniques (Waszak 1996, Blue and Balas 1997, and Taylor et al. 2007), and has been used to validate many types of control systems (Barker and Balas 1999, Barker and Balas 2000, and Mukhopadhyay 2000). These control schemes used

Figure 3.2: Benchmark Active Control Technologies (BACT) wing on an oscillating turntable. Image courtesy of NASA, `www.nasaimages.org`.

on the BACT will be revisited later in Section 3.2.1.

Another two degree-of-freedom aeroelastic platform that has been used as a test-bed for active control techniques is the Nonlinear Aeroelastic Test Apparatus (NATA), shown in Figure 3.3, located at Texas A&M University. The NATA has interchangeable aerofoils mounted to a carriage underneath the wind tunnel that allows it to pitch and plunge. Pitch and plunge are measured using encoders located on the carriage, and controlled using trailing-edge or leading- and trailing-edge (depending on the attached aerofoil) control surfaces actuated using servo motors. A thorough overview of the NATA hardware is given in Section 4.1.

The NATA is designed for operation at a lower airspeed, and features a nonlinear torsional spring for the evaluation of the effects of structural nonlinearity. The experimental effects of this structural nonlinearity have been presented and analysed by O Neil and Strganac (1998), Strganac et al. (2000), and Sheta et al. (2002), and theoretical effects have been investigated in Singh and Brenner (2003*a*), and Baldelli et al. (2008). The NATA has also had many different control systems experimentally applied to it, including Block and Strganac (1998), Strganac et al. (2000), and Platanitis and Strganac (2004). These active control techniques will be discussed in more detail below in Section 3.2.1.

Figure 3.3: Nonlinear Aeroelastic Test Apparatus in a wind tunnel at Texas A&M University.

3.2.1 Active control of aeroelasticity

There has been much research on the active control of aeroelasticity, sometimes termed aeroservoelasticity. The work presented here will largely focus on the more recent two and three degree-of-freedom efforts. For a more general historic overview, the reader is again referred to the article by Mukhopadhyay (2003).

An early example of applied active control of aeroelasticity is given by Karpel (1982). He compared several techniques for a low-order estimation of unsteady aerodynamics, and developed a new technique for a more accurate reduced-order approximation of the unsteady aerodynamic loads in the Laplace domain. The reduced-order aerodynamic model allowed for simpler control design, and using it he was able to design a constant-gain feedback controller using a pole-placement technique which was able to stabilise the aerofoil across its ight envelope.

Another example of typical section aeroelasticity control is the mixed $\mathcal{H}_\infty / \mathcal{H}_2$ controller synthesised by Özbay and Bachmann (1994). Using Theodorsen s formulation for unsteady aerodynamics and a three degree-

of-freedom mechanical aerofoil model, an infinite dimensional model (due to the aerodynamic model) was developed. This infinite dimension model was truncated to a finite size, and right coprime factorised, with the maximum error in aerodynamic model truncation acting as the perturbation $\Delta_{\mathbf{M}}$ (see Section 2.2.5.2). A robustly stabilising $\mathcal{H}_\infty$ controller was then synthesised, and combined with a gust response $\mathcal{H}_2$ minimisation control objective, which was modelled as low-pass filtered white-noise disturbances to the pitch, plunge and trailing-edge deflection states. Numerical results were presented in the form of closed-loop input to output and sensitivity transfer function magnitudes.

Further work on controlling aeroelasticity on a typical section aerofoil using an unsteady aerodynamic model continued. With the construction of the BACT, many of these control methods were able to be experimentally validated. As an example, Mukhopadhyay (2000) evaluated a variety of active control techniques, including several classical techniques using both pitch-rate feedback and pitch and pitch-rate feedback, as well as a mixed LQG and minimax (equivalent to $\mathcal{H}_\infty$), on the BACT in the transonic flutter regime. Using one of the classical control laws, the flutter dynamic pressure was increased by approximately 50% compared to the open loop results, as well as alleviate gust response by as much as 30% compared to the open-loop stable response.

Several $\mathcal{H}_\infty$ and μ based controllers, including Single Input Single Output (SISO) and Multiple Input and Multiple Output (MIMO) variations, were synthesised and compared for the BACT by Waszak (2001). These controllers were synthesised using the P–Δ framework, which separates a nominal plant, P, from the uncertainty in the model, which acts as an upper Linear Fractional Representation (LFR) perturbation, Δ. The control objectives were designed around scaled input and output signals, similar to mixed-sensitivity performance objectives. The resulting control laws were able to suppress flutter across the usable wind tunnel dynamic pressure and Mach number, and were shown to be robust by evaluating the minimum structured singular values.

Of particular relevance to the work presented in this thesis, Blue and Balas (1997) rearranged the dynamics of the BACT using a Linear Fractional Transformation (LFT) such that the feedback term, Δ, was a function of dynamic pressure and Mach number. This model was then used for developing a gain-scheduled LFR controller by Barker

and Balas (1999). They used LMIs to synthesise a controller based on several weighted $\mathcal{L}_2$ performance channels, with the controller gain-scheduled via an upper LFT with the same Δ which was used in the BACT model. The weighted $\mathcal{L}_2$ performance criteria used were to minimise peak response of pitch and plunge, and minimise the closed-loop response to noise and disturbances. Experimental results show that the LFR gain-scheduled controller was able to extend the utter boundary by over 50% for a large range of Mach numbers, as well as improve vibration attenuation.

The LFR gain-scheduled controller by Barker and Balas (1999) was compared to a directly synthesised LPV controller using the same performance specification framework by Barker and Balas (2000). Results show that the controller synthesised using the direct LPV framework offer a significant performance advantage over the LFR scheduled system, which is most likely due to the use of parameter dependent transformed Lyapunov matrices in the LPV case. In particular, they state that the LPV scheme achieves these improved results with less rapid actuator demands than the LFR controller by Barker and Balas (1999).

The first instance of experimental active control applied to the NATA was by Block (1996), an extract of which was published later (Block and Strganac 1998). He constructed a three degree-of-freedom model of the NATA with unsteady aerodynamics, which were approximated using the Jones approximation to Theodorsen s function. The model was compared with experimental utter data, and shown to match well in both utter speed and frequency. An LQG controller was then derived and applied, and experimentally shown to be able to settle limit-cycle oscillations in around three seconds.

This experimental work was followed by Strganac et al. (2000), who used a two degree-of-freedom model of the NATA with quasi-steady aerodynamics, and synthesised a feedback linearisation adaptive controller to suppress limit-cycle oscillations. The quasi-steady aerodynamic model was used in this work as they found that for low Strouhal numbers, $\frac{fb}{U} < 0.1$, where f is the oscillation frequency, b is the chord length and U is the airspeed, that there was negligible difference compared to the unsteady aerodynamic model. The control scheme used by Strganac et al. (2000) was based on that by Ko et al. (1999) for the two degree-of-freedom NATA and Ko and Strganac (1998), who applied the feedback

linearisation adaptive controller to a theoretical model, based on the NATA, that had two trailing-edge control surfaces, located at opposite ends of the aerofoil span. The experimental results shown by Strganac et al. (2000) demonstrate effective suppression of limit-cycle oscillations, with pitch settling in around one second, and plunge settling in around three seconds after the controller is activated.

The above references for experimental control on the NATA were performed on the original NATA aerofoil, which is discussed in Section 4.1, and shown in Figure 4.1. Later, a second aerofoil, which is also discussed in Section 4.1, and shown in Figure 4.2, which featured both leading- and trailing-edge control surfaces was installed into the NATA. This new section was used by Platanitis and Strganac (2004), who extended the adaptive nonlinear control scheme of Xing and Singh (2000). The work by Xing and Singh (2000) was based on a two degree-of-freedom NATA model with quasi-steady aerodynamics. The adaptive nonlinear control scheme used by Xing and Singh (2000) was based on the backstepping method, and the system parameters were assumed to be unknown, with the exception of a few parameters for which the sign was assumed to be known. The simulated results presented show limit-cycle oscillations and parameter estimations settling after approximately five seconds.

Platanitis and Strganac (2004) extended the control scheme of Xing and Singh (2000) by including the leading-edge control surface as a control input. When Platanitis and Strganac (2004) experimentally tested this control scheme, the results from using both control surfaces, as well as just using the trailing-edge control surface were unimpressive as the controller heavily saturated the control surfaces before managing to suppress the limit-cycle oscillations after around three seconds. It is thought by the author of this thesis that this is largely due to the neglection of the servo motor dynamics in the two degree-of-freedom model, discussed further in Section 4.4.

Later, the NATA with the second aerofoil was used by Platanitis and Strganac (2005) to develop a method of preventing control reversal by using the leading-edge control surface in combination with the trailing-edge control surface.

Many other authors have synthesised controllers for the two degree-of-freedom NATA without experimental validation. There have been several avours of nonlinear backstepping adaptive controllers, including

the aforementioned article by Xing and Singh (2000), and several others (Singh and Wang 2002, Reddy et al. 2007, and Lee and Singh 2009). These articles used the quasi-steady aerodynamic model, and due to it being a two degree-of-freedom model, implicitly assumed perfect trailing-edge control. In addition, controllers synthesised using backstepping control methodologies often have high feedback gain, which results is aggressive actuator demands, especially in the presence of unmodelled dynamics, such as the results presented by Platanitis and Strganac (2004) based on the controller in Xing and Singh (2000), and the results presented by Reddy et al. (2007).

Singh and Yim (2003) presented a nonlinear full-state feedback controller for the two degree-of-freedom NATA with quasi-steady aerodynamics based on the optimal infinite-horizon control law. Full-state feedback gains were solved using a state-dependent Riccati equation, allowing the gain to schedule with the pitch stiffness nonlinearity. Tadi (2003) presented a similar control method, with the inclusion of an optimal estimator. Both articles presented good simulation results, settling the closed-loop system after a pitch perturbation in around one to three seconds.

A modular adaptive control scheme for the two degree-of-freedom NATA with unsteady aerodynamics was presented by Singh and Brenner (2003*b*). The modular adaptive control scheme involved synthesising a input-to-state stabilising control law based on integrator backstepping, with separate adaptation, and the adaptation error treated as a disturbance into the stabilising control law. As with some of the other backstepping based control schemes, the simulated results after a pitch perturbation show the control surface saturating before finally settling the system after approximately three seconds.

Another nonlinear backstepping controller, although this time without adaptation, was presented by Bhoir and Singh (2004). This work used the two degree-of-freedom NATA model, but with an unsteady aerodynamic model. The presented simulation results show utter suppression after approximately three seconds following a pitch perturbation, however the control surface heavily saturates until the system settles.

Lee and Singh (2007) presented another nonlinear backstepping based controller for the two degree-of-freedom NATA with quasi-steady aerodynamics. The controller is said to be robust, because only the sign

of certain parameters are assumed to be known. This should not be confused with the way the term robust is used in modern or classical control. The results presented by Lee and Singh (2007) show effective utter suppression, however the control signal has been omitted from the article, so no conclusions about the practicality of the controller can be drawn, as many of these backstepping based controllers have very high gain, putting unreasonable demands on the trailing-edge control surface.

There has been research on two, three and four degree-of-freedom aeroelastic systems other than the BACT and NATA. Using an aeroelastic system consisting of a NACA 0012 aerofoil attached to a exible mount, and modelled using a low-order approximation to Theodorsen s function, De Marqui Jr et al. (2005) successfully applied a state-feedback pole-placement controller to suppress utter.

Another two degree-of-freedom aeroelastic system located at Duke University has been used for aeroelasticity control experiments, including Cox (2003), and McEver et al. (2007). Cox (2003) used a three degree-of-freedom model with unsteady aerodynamics to synthesise an LPV controller. The LPV controller was synthesised using LMIs, and consisted of a regional pole-placement requirement, along with a LQG-style controller designed for gust minimisation. Regional pole-placement involves creating a region in the s-plane in which the poles must be located, and Cox (2003) uses a conic region in the left-half plane which gives a minimum damping ratio of 0.1.

The LPV controller was synthesised using a reduced-order aerodynamic model with a quadratic dependence on airspeed, however a fixed transformed Lyapunov matrix was used, limiting the range over which the controller could schedule. The controller achieved the pole-placement and $\mathcal{H}_2$ norm requirements over the range of airspeeds from $U = 5\,\mathrm{m/s}$ to $U = 25\,\mathrm{m/s}$.

Cox (2003) then performed LPV system identification and applied the above control scheme to their aeroelastic system. The results show good utter suppression and minimum damping ratio, however the $\mathcal{H}_2$ norm results were suboptimal compared to their point-wise counterparts.

McEver et al. (2007) used the same aeroelastic system and performed closed-loop Q-parameterisation system identification on it. This involves the use of a stabilising controller and an excitation signal in order to perform system identification on the closed-loop system, which is useful

for system identification above the flutter speed. Using these results, an improved controller was constructed which was able to extend the flutter boundary by 52%.

Silva and Júnior (2006) performed flutter control simulations on a three degree-of-freedom aeroelastic system. The controller was synthesised using an LMI representation of a LQG controller, along with an ellipsoid inequality to limit the actuator demands. Their controller was made robust by solving the LMIs simultaneously at the vertices of the cube formed by uncertainty about the three stiffness parameters (pitch, plunge and trailing-edge stiffnesses). The simulations showed the robust version of their controller suppressed flutter more effectively than the controller synthesised at the nominal stiffnesses point.

Vepa (2007) created a flutter suppression controller for a four degree-of-freedom aeroelastic system with unsteady aerodynamics using transport lag compensation. The results show that the system poles are entirely contained in the left-half plane, hence the system is stable, for all of the airspeeds considered. No simulation or experimental results were presented.

3.3 Conclusions

As should be apparent, there has been considerable research into the active control of aeroelasticity, including LPV control. However, much of the work cited above has not been experimentally validated, and in particular for work based on two degree-of-freedom NATA models, many authors neglect the trailing-edge surface dynamics, which can lead to poor experimental results, such as those by Platanitis and Strganac (2004). In addition, although many backstepping based controllers have been derived and tested using simulations, they often have high gain, and in the presence of unmodelled dynamics, such as the servo-motor dynamics, put unreasonable demands on the control surface actuators. Thus, it is important that a high-fidelity dynamic model of the NATA including control surface dynamics be developed.

Another issue is that many of these advanced backstepping controllers provide no measure of robustness, which is at odds with the requirements of practical aerospace applications. Thus there exists a need for advanced nonlinear aeroelasticity controllers that can operate over a wide range

of operating conditions, while providing performance and robustness guarantees, such as those provided using LPV control.

The LPV aeroelasticity control methods cited above generally do not use the most common objectives, such as LQR or $\mathcal{H}_\infty$ loop-shaping. In addition, with the exception of Barker and Balas (2000), the LPV control methods use a fixed transformed Lyapunov matrix, limiting the achievable performance and scheduling range. Thus, there also exists an opportunity to apply the more standardised control methodologies to an LPV framework, such as LQR and $\mathcal{H}_\infty$ (induced $\mathcal{L}_2$ when used in an LPV system) loop-shaping to an aeroelastic system, with parameter dependent transformed Lyapunov matrices if possible, and investigate the resulting performance and scheduling range.

While several authors have constructed dynamic aeroelasticity models in LFR, none have used an LFT to linearise the quadratic airspeed dependence of the dynamic model.

Finally, methods of reducing the performance norms (hence increasing the performance) via the use of a parameter dependent performance bound has not been investigated.

4 Nonlinear Aeroelastic Test Apparatus

The Nonlinear Aeroelastic Test Apparatus (NATA) is an experimental testbed for research in nonlinear aeroelasticity and novel aeroelastic control methodologies (Block and Strganac 1998, Ko and Strganac 1998, O Neil and Strganac 1998, Strganac et al. 2000, Sheta et al. 2002, Platanitis and Strganac 2004, and Platanitis and Strganac 2005). The NATA is located in the Aerospace Engineering Department at Texas A&M University. The author visited Texas A&M University from the 24th of August to the 21st September 2008 to use the NATA. He was kindly hosted by Professor Strganac from the Aerospace Department, and was provided with financial assistance from The Sir Ross and Sir Keith Smith Fund, acknowledged on page 153.

4.1 Equipment

The NATA consists of interchangeable rigid wing sections that spans the height of a 3×2 foot working section wind tunnel. There are two wing sections that have been used in the past. The first of which is the original wing section which featured in papers such as Block and Strganac (1998), O Neil and Strganac (1998), Ko and Strganac (1998), Strganac et al. (2000), and Sheta et al. (2002), and is shown in Figure 4.1. This wing section was made of folded steel, and previously had an aluminium plate attached to the trailing edge to act as a control surface.

The second wing section was constructed from an Aluminium skeleton with a perspex skin, with both a leading- and trailing-edge control surface as shown in Figure 4.2. Two Futuba S9402 servo motors and two US Digital E2-1024-375-H optical encoders were located inside the wing

Figure 4.1: Photograph of the original wing section in the wind tunnel.

body to actuate and measure the position of the control surfaces. This wing section has featured in several papers with experimental results such as Platanitis and Strganac (2004), and Platanitis and Strganac (2005).

The wings were mounted on a plate that protruded from the base of the wind-tunnel. The plate was attached to a carriage below the wind-tunnel which allowed it to plunge (h, translational motion perpendicular to the free-stream ow), and pitch (α, angular motion relative to the ow). Translational stiffness was provided by a translational spring, and the displacement was measured by an encoder located on a pulley connected to the carriage. Torsional stiffness was provided by translational springs that were attached to a cam on the pitch shaft. A schematic and a photograph of this arrangement is shown in Figures 4.3 and 4.4. The cam provided a nonlinear torsional stiffness that allowed the wing to undergo limit-cycle oscillations.

The wind tunnel has a 3×2 foot working section, variable fan pitch

Figure 4.2: Photograph of the second wing section in the wind tunnel, with the leading edge taped in position.

control and has freestream air temperature regulation. Freestream airspeed is measured using a pitot tube connected to a pressure transducer. All of the wind tunnel controls were located in a dedicated cabinet located next to the working section.

Both the wing and pressure transducer were wired into a power supply and the breakout board of a Humusoft MF624 multifunction I/O card located inside a host computer.

As previously stated, the second wing contains two Futuba S9402 RC servo motors to actuate the leading- and trailing-edge control surfaces. RC servo motors are controlled by a Pulse Width Modulation (PWM) signal that typically runs at a frequency of 50 Hz, with pulse widths varying between 1 ms and 2 ms, which correspond to the minimum and
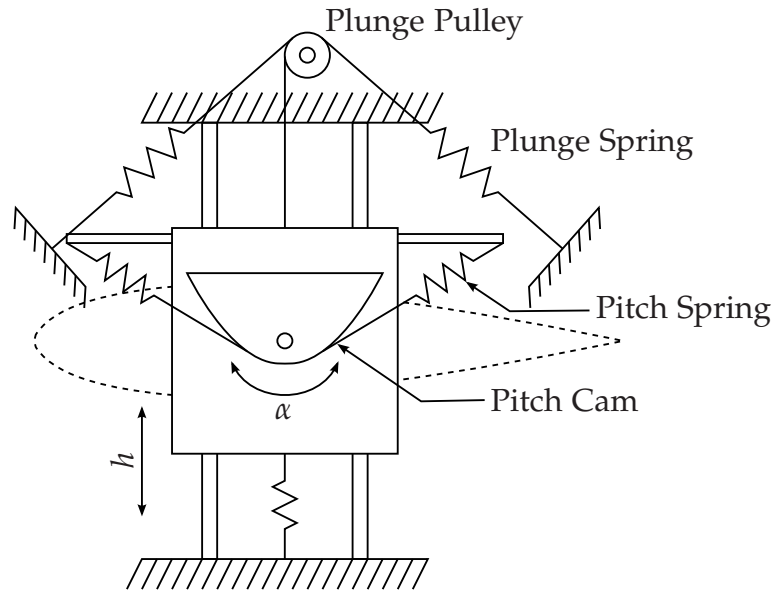
Figure 4.3: Schematic of the carriage mechanism when viewed from underneath the wind tunnel.
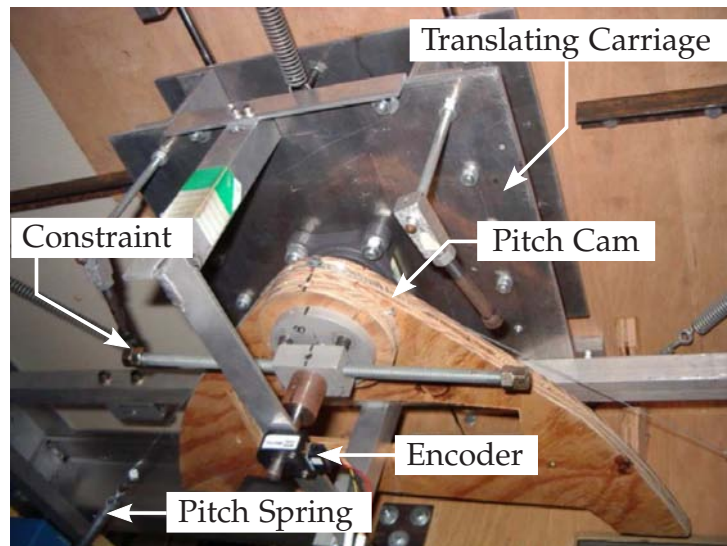
Figure 4.4: Photograph of the carriage mechanism when viewed from underneath the wind tunnel.

maximum de ection angles. These servo motors are connected with three wires: a power source between $+4.8\,$V and $+6\,$V; a common ground; and a signal wire. The PWM signal wire was connected to a 32-bit hardware timer output on the MF624 board, which generated the PWM signal. Without knowledge of the underlying timer hardware and the software PWM implementation it is impossible to calculate an exact value of the signal to noise ratio (SNR) of the PWM signal. Regardless, a signal to noise ratio estimate based on the 20 ns resolution specified by Humusoft is 94.0 dB.

There are two US Digital E2-1024-375-H optical encoders inside the second wing to measure the de ections of the two control surfaces. The carriage has a further two US Digital E2-1024-375-H optical encoders to measure both pitch and plunge. These encoders have a resolution of 1024 pulses per revolution, two main channels, and a third index channel. The encoders are connected with five wires; a power source at $+5\,$V, a common ground, channel A, channel B, and the index channel. Channels A & B from the encoders were connected to hardware encoder readers on the MF624, with the index input on the MF624 held high to prevent accidental reset. The MF624 encoder readers were operating in quadrature mode, providing a resolution of 4096 counts per revolution. Given an expected range of $\pm 0.5\,$rad for pitch and the trailing-edge control surface the signal to noise ratio for these measurements is 56.2 dB.

The radius of the cam connecting the plunge motion to its encoder was $r_h = 0.06\,$m, which gives a resolution of 10 865 counts per metre. Given an expected plunge range of $\pm 0.04\,$m, this corresponds to a signal to noise ratio of 58.7 dB.

The pressure transducer outputs a voltage proportional to the dynamic pressure, and has a sensitivity 1.606 mV/Pa. This voltage output was connected to a 14-bit Analogue-to-Digital converter on the MF624. The dynamic pressure was converted into a freestream airspeed using:

$$U = \sqrt{\frac{2p_d}{\rho}}, \tag{4.1}$$

where:
    U [m/s] is the freestream airspeed,
    ρ [kg/m^3] is the air density, and
    p_d [Pa] is the measured dynamic pressure.

The air density was calculated from the (regulated) temperature using:

$$\rho = \frac{p_s}{RT},$$ (4.2)

where:

$p_s = 100.8\,\text{kPa}$ is the static air pressure,
$R = 286.9\,\frac{\text{J}}{\text{kg}\cdot\text{K}}$ is the specific gas constant for dry air, and
T [K] is the absolute air temperature.

The 14-bit range of the MF624 ADC spans an input voltage range from $-10\,\text{V}$ to $10\,\text{V}$. Knowing this, the pressure transducer sensitivity and the expected airspeed range between $0\,\text{m/s}$ and $15\,\text{m/s}$, the airspeed resolution can be calculated to be 12.1 discrete values per $1\,\text{m/s}$ interval, or as a 45.1 dB signal to noise ratio.

4.2 Software

The Humusoft MF624 I/O card was controlled using the Real-Time Windows Target toolbox for The MathWorks Simulink. The four encoders were read using the Encoder Input blocks in quadrature mode and normalised to angles in radians and displacement in metres.

The two servo motors inside the second wing section were controlled using the Frequency Output blocks set to modulate duty cycle, with the signal normalised to produce high-pulse times between 1 ms and 2 ms at a frequency of 50 Hz as per the requirements for RC servo motors.

The airspeed was measured using an Analog Input block connected to the pressure transducer, which in turn is connected to the pitot tube in the wind tunnel. The dynamic pressure from the pressure transducer was converted into airspeed inside a subsystem named Pitot tube read.

The basic Simulink model used, which includes all of the input/output blocks used as well as the blocks that convert the quantities to SI units can be found on the additional materials CD, or as an attachment to the PDF version of this document.

4.3 Experimental considerations

Hard stops were placed at approximately $\alpha = \pm 0.3\,\text{rad}$ to prevent limit-cycle oscillations, described in more detail in Section 4.6, from growing

too large and damaging the carriage.

The freestream airspeed velocity was limited to 15 m/s in all experiments to prevent possible damage to the NATA and for safety reasons. At this airspeed the wing would hit the hard-stops described above during uncontrolled limit-cycle oscillations.

As mentioned above in Section 4.1, the wind tunnel freestream air was temperature regulated. During all experiments the air temperature was kept at a constant 12.8 °C (55 °F). This value was also used in the calculation of air density, Equation (4.2), for the simulations.

During four degree-of-freedom experiments, as described in Section 4.4.2, at airspeeds above approximately $U = 12$ m/s, the aerodynamic moment acting on the leading-edge control surface was greater than the torque capacity of the servo-motor, hence the leading-edge would diverge from the origin. An example of this divergence from a control experiment is given in Figure 4.5. For this reason all control experiments were limited to the three degree-of-freedom model, as described in Section 4.4.1.

During the three degree-of-freedom experiments the leading-edge surface was taped in position, as previously shown in Figure 4.2. This served to rigidly link the main wing body to the leading-edge surface, and to form a continuous section over the main wing/leading-edge link, which improved the aerodynamics of the wing.

Full-state output is when all of the dynamic states are measured. The encoders on the NATA only measure pitch, plunge, leading- and trailing-edge surface deflection. Full-state output was approximated using filters to estimate the temporal derivatives of these states. The transfer function of this filter used in experiments is:

$$\mathbf{G}_D(s) = \frac{s}{\frac{1}{50}s + 1}, \tag{4.3}$$

which is comprised of the a numerical derivative, and a single pole low-pass filter of 50 rad/s ($\approx$ 8 Hz) bandwidth. This provides accurate estimates of the temporal derivative states due to the high resolution of the encoders. The maximum bandwidth of the NATA is 27.7 rad/s, which is the speed of the trailing-edge servo motor, shown in Section 4.5.5.2. At this frequency there will be some phase delay through the filter, Equation (4.3), however in practice it proved not to be a problem.
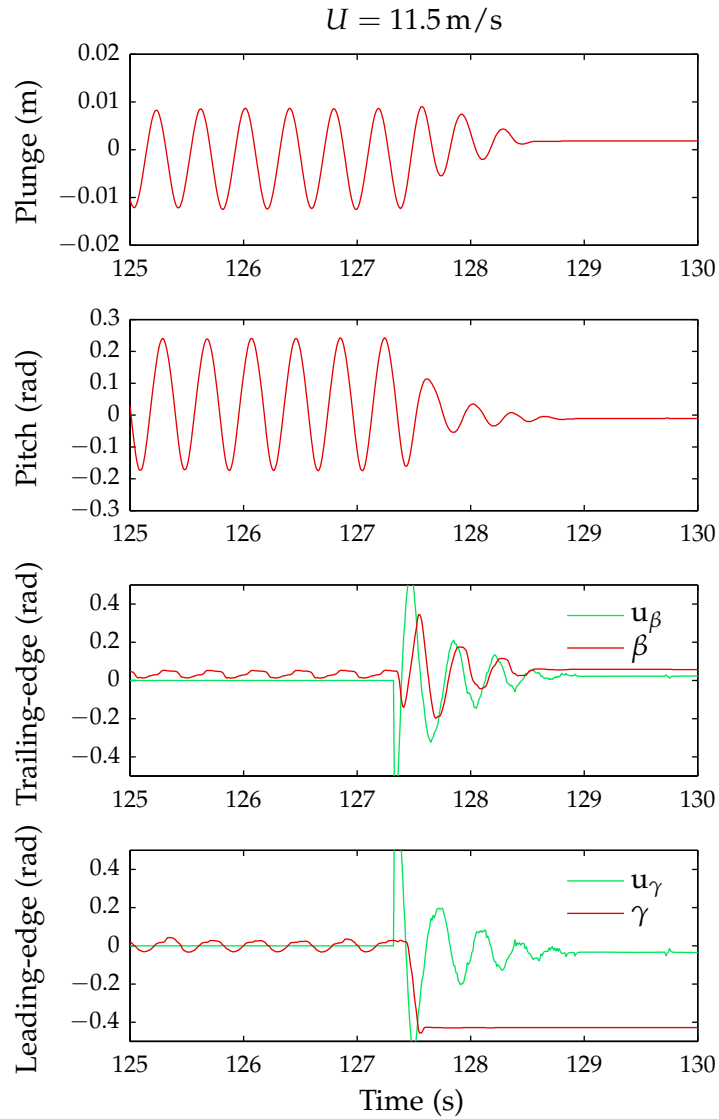
Figure 4.5: Example of the leading-edge diverging during a control experiment, with the control input, $\mathbf{u} = \begin{bmatrix} u_\beta & u_\gamma \end{bmatrix}^T$.

4.4 Dynamic model

Some previously published work, for example that by Strganac et al. (2000), and Platanitis and Strganac (2004), had difficulty achieving good performance in practice from the controlled wing. It was found that this difficulty was largely due to the phase-lag of the servo-motors, which was not captured by their dynamic model. Higher order dynamic models that more completely capture the servo motor dynamics as well as the inertial coupling between bodies are derived below.

These previous works normalised the dimensions of the aerofoil with respect to the half-chord length to create a non-dimensional model. However, to simplify the dynamic derivations a dimensional model is used here. It is straight-forward to convert the dimensional model to a non-dimensional model at the end of the derivation.

4.4.1 Three degree-of-freedom model

The dynamic states: pitch, plunge, and trailing-edge surface deflection (α, h, and β respectively), and the relevant dimensions of the three degree-of-freedom model are shown in Figure 4.6. The aerodynamic force and moment acting on the elastic axis are being modelled using the so called quasi-steady aerodynamic model, Section 2.4.3.2, which is a standard steady aerodynamic model augmented with linearised contributions to the angle of attack from the motion of the aerofoil. The aerodynamic force and moment are (Strganac et al. 2000):

$$L = \rho U^2 b S C_{l_\alpha} \left(\alpha + \frac{h}{U} + r_{3c/4} \frac{\alpha}{U} \right) + \rho U^2 b S C_{l_\beta} \beta, \qquad (4.4)$$

$$M = \rho U^2 b^2 S C_{m_{\alpha,\text{eff.}}} \left(\alpha + \frac{h}{U} + r_{3c/4} \frac{\alpha}{U} \right) + \rho U^2 b^2 S C_{m_{\beta,\text{eff.}}} \beta, \qquad (4.5)$$

where:
  L [N] is the lift force acting at the elastic axis,
  M [N·m] is the aerodynamic moment acting at the elastic axis,
  b [m] is the half-chord length,
  $r_{3c/4}$ [m] is the distance from the elastic axis to the 3/4–chord point of the wing,
  $C_{l_\alpha} = \frac{\partial C_l}{\partial \alpha}$ is the aerofoil coefficient of lift about the elastic axis,
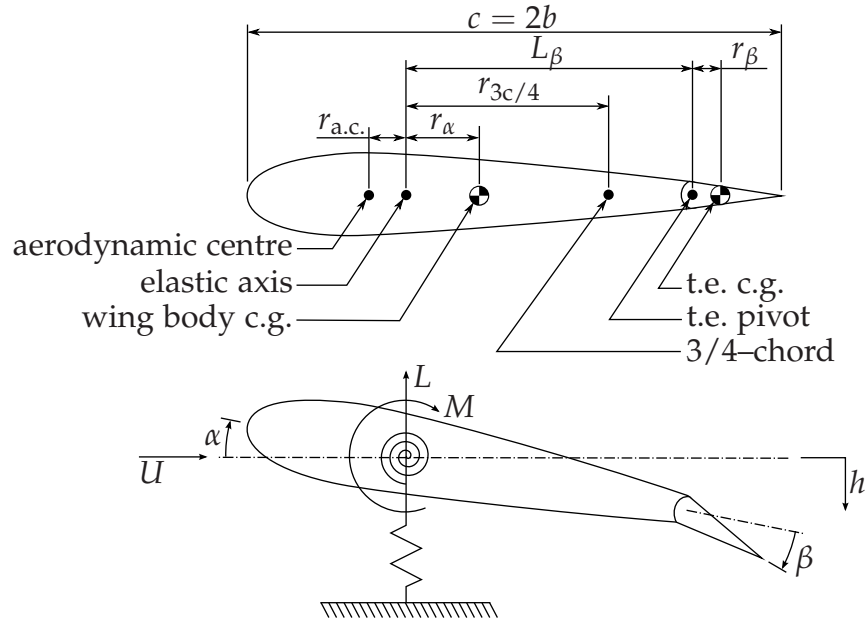
Figure 4.6: Three degree of freedom NATA model, showing states and dimensions.

$C_{l_\beta} = \frac{\partial C_l}{\partial \beta}$ is the trailing-edge surface coefficient of lift about the elastic axis,

$C_{m_{\alpha,\text{eff.}}} = 2\frac{\partial C_m}{\partial \alpha} + \frac{r_{\text{a.c.}}}{b}C_{l_\alpha}$ is the aerofoil moment coefficient about the elastic axis,

$C_{m_{\beta,\text{eff.}}} = 2\frac{\partial C_m}{\partial \beta} + \frac{r_{\text{a.c.}}}{b}C_{l_\beta}$ is the trailing-edge moment coefficient about the elastic axis, and

$r_{\text{a.c.}}$ is the distance from the elastic axis to the aerodynamic centre.

Note that this quasi-steady aerodynamic moment does not include the $\frac{c\pi}{8U}\alpha$ term from Equation (2.129). This has been omitted for consistency with the current literature. The omitted term provides only a minor contribution to the aerodynamic damping compared to the $r_{3c/4}$ term, and is partly accounted for in the work presented in this thesis during the system identification stage in Section 4.5.6. Hence this omission has a negligible effect on the model dynamics.

The reference frames used for the derivation are shown in Figure 4.7.

In the following sections, the dynamics are derived using two different methods, the Lagrangian energy method, and Newton-Euler iteration, then linearised and converted to a state-space form.
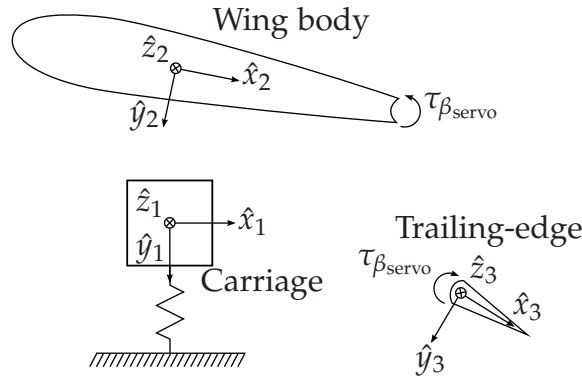
Figure 4.7: Reference frames used for the derivation of the three degree-of-freedom model.

4.4.1.1 Lagrangian energy method

The Lagrangian energy method involves computing a Lagrangian function, and taking partial and temporal derivatives of this Lagrangian to calculate the equations of motion in generalised coordinates. A thorough description of this method is given by Symon (1960).

The derivation of the dynamics using a Lagrangian energy method is as follows.

The velocity and angular velocity of frame 1 are:

$$\mathbf{v}_1 = \begin{bmatrix} 0 & h & 0 \end{bmatrix}^\mathrm{T} \tag{4.6}$$

$$\boldsymbol{\omega}_1 = \begin{bmatrix} 0 & 0 & 0 \end{bmatrix}^\mathrm{T} \tag{4.7}$$

from which the potential and kinetic energy of this first frame are:

$$V_1 = \tfrac{1}{2} k_h h^2, \text{ and} \tag{4.8}$$

$$T_1 = \tfrac{1}{2} m_h h^2 \tag{4.9}$$

respectively, where:

m_h [kg] is the mass of the components in the carriage that only translate (and do not rotate), and

k_h [N/m] is the translational spring stiffness.

The transformation from frame 1 to frame 2 is through a rotation

65

about $\hat{z}_1$ by amount α. This is described by the rotation matrix:

$$
{}_1^2\mathbf{R} = \begin{bmatrix} \cos(\alpha) & \sin(\alpha) & 0 \\ -\sin(\alpha) & \cos(\alpha) & 0 \\ 0 & 0 & 1 \end{bmatrix}. \tag{4.10}
$$

The translational and angular velocity of frame 2 are then:

$$
\mathbf{v}_2 = {}_1^2\mathbf{R}\mathbf{v}_1 = \begin{bmatrix} h\sin(\alpha) & h\cos(\alpha) & 0 \end{bmatrix}^\mathsf{T}, \tag{4.11}
$$

$$
\boldsymbol{\omega}_2 = {}_1^2\mathbf{R}\boldsymbol{\omega}_1 + \begin{bmatrix} 0 & 0 & \alpha \end{bmatrix}^\mathsf{T} = \begin{bmatrix} 0 & 0 & \alpha \end{bmatrix}^\mathsf{T}. \tag{4.12}
$$

The velocity at the centre of mass of the wing section is then:

$$
\mathbf{v}_{c_2} = \mathbf{v}_2 + \boldsymbol{\omega}_2 \times \begin{bmatrix} r_\alpha & 0 & 0 \end{bmatrix}^\mathsf{T} = \begin{bmatrix} h\sin(\alpha) & h\cos(\alpha) + \alpha r_\alpha & 0 \end{bmatrix}^\mathsf{T}, \tag{4.13}
$$

from which the potential and kinetic energies can be calculated as:

$$
V_2 = \tfrac{1}{2}k_\alpha \alpha^2, \text{ and} \tag{4.14}
$$

$$
\begin{aligned}
T_2 &= \tfrac{1}{2}\mathbf{v}_{c_2}^\mathsf{T} m_\alpha \mathbf{v}_{c_2} + \tfrac{1}{2}\boldsymbol{\omega}_2^\mathsf{T}\mathbf{I}_2\boldsymbol{\omega}_2 \\
&= \tfrac{1}{2}m_\alpha\left(h^2 + \alpha^2 r_\alpha^2 + 2h\alpha r_\alpha \cos(\alpha)\right) + \tfrac{1}{2}\alpha^2 I_\alpha,
\end{aligned} \tag{4.15}
$$

where:

 k_α [N·m/rad] is the torsional spring stiffness,

 m_α [kg] is the mass of the wing and the rotational component of the carriage,

 $\mathbf{I}_2$ is the principle moment of inertia matrix about the wing s centre of mass, with $\mathbf{I}_2 = \operatorname{diag}(0, 0, I_\alpha)$, and

 I_α [kg·m^2] is the rotational moment of inertia of the wing and rotational component of the carriage about the $\hat{z}_2$ axis and located at the wing s centre of mass.

Similarly, the transformation from frame 2 to 3 is a rotation about $\hat{z}_2$ by amount β. This is described by the transformation matrix:

$$
{}_2^3\mathbf{R} = \begin{bmatrix} \cos(\beta) & \sin(\beta) & 0 \\ -\sin(\beta) & \cos(\beta) & 0 \\ 0 & 0 & 1 \end{bmatrix}. \tag{4.16}
$$

The translational and angular velocity of frame 2 are then:

$$\mathbf{v}_3 = {}^3_2\mathbf{R}\mathbf{v}_2 + {}^3_2\mathbf{R}(\boldsymbol{\omega}_2 \times \begin{bmatrix} L_\beta & 0 & 0 \end{bmatrix}^{\mathrm{T}})$$
$$= \begin{bmatrix} h\sin(\alpha + \beta) + \alpha L_\beta \sin(\beta) & h\cos(\alpha + \beta) + \alpha L_\beta \cos(\beta) & 0 \end{bmatrix}^{\mathrm{T}},$$
$$\tag{4.17}$$

$$\boldsymbol{\omega}_3 = {}^3_2\mathbf{R}\boldsymbol{\omega}_2 + \begin{bmatrix} 0 & 0 & \beta \end{bmatrix}^{\mathrm{T}} = \begin{bmatrix} 0 & 0 & \alpha + \beta \end{bmatrix}^{\mathrm{T}}. \tag{4.18}$$

The velocity at the centre of mass of the trailing-edge section is then:

$$\mathbf{v}_{c_3} = \mathbf{v}_3 + \boldsymbol{\omega}_3 \times \begin{bmatrix} r_\beta \\ 0 \\ 0 \end{bmatrix} = \begin{bmatrix} h\sin(\beta + \alpha) + \alpha L_\beta \sin(\beta) \\ h\cos(\beta + \alpha) + \alpha L_\beta \cos(\beta) + r_\beta\alpha + r_\beta\beta \\ 0 \end{bmatrix}. \tag{4.19}$$

The potential and kinetic energies are calculated as:

$$V_3 = 0, \text{ and} \tag{4.20}$$
$$T_3 = \tfrac{1}{2}\mathbf{v}_{c_3}^{\mathrm{T}} m_\beta \mathbf{v}_{c_3} + \tfrac{1}{2}\boldsymbol{\omega}_3^{\mathrm{T}} \mathbf{I}_3 \boldsymbol{\omega}_3, \tag{4.21}$$

where:
  m_β [kg] is the mass of the trailing-edge,
  $\mathbf{I}_3$ is the principle moment of inertia matrix of the trailing-edge located at the centre of mass of the trailing-edge, with $\mathbf{I}_3 = \mathrm{diag}(0, 0, I_\beta)$, and
  I_β [kg·m^2] is the rotational moment of inertia of the trailing-edge section in the $\hat{z}_3$ axis and located at its centre of mass.
The expanded kinetic energy term has been omitted for the sake of brevity.

The Lagrangian is then defined as the difference between kinetic and potential energies:

$$\mathcal{L} = (T_1 + T_2 + T_3) - (V_1 + V_2 + V_3). \tag{4.22}$$

Substituting in replacement terms for the apparent inertia terms from their parallel-axis theorem equivalents

$$\hat{I}_\alpha = I_\alpha + m_\alpha r_\alpha^2, \text{ and} \tag{4.23}$$
$$\hat{I}_\beta = I_\beta + m_\beta r_\beta^2, \tag{4.24}$$

and assuming that the trailing-edge servo-motor dynamics can be represented by a second-order system of the form

$$\hat{I}_\beta \ddot{\beta} + c_{\beta_{\text{servo}}} \dot{\beta} + k_{\beta_{\text{servo}}} \beta = k_{\beta_{\text{servo}}} u_\beta, \tag{4.25}$$

where:

$c_{\beta_{\text{servo}}}$ [Nm·s/rad] is the virtual damping provided by the trailing-edge servo motor,

$k_{\beta_{\text{servo}}}$ [Nm/rad] is the virtual stiffness provided by the trailing-edge servo motor, and

u_β [rad] is the trailing-edge control signal, such that $\mathbf{u} = u_\beta$,

the dynamics of the entire system can be found as:

$$\frac{d}{dt} \begin{bmatrix} \frac{\partial \mathcal{L}}{\partial \dot{h}} \\ \frac{\partial \mathcal{L}}{\partial \dot{\alpha}} \\ \frac{\partial \mathcal{L}}{\partial \dot{\beta}} \end{bmatrix} - \begin{bmatrix} \frac{\partial \mathcal{L}}{\partial h} \\ \frac{\partial \mathcal{L}}{\partial \alpha} \\ \frac{\partial \mathcal{L}}{\partial \beta} \end{bmatrix} = - \begin{bmatrix} 0 \\ 0 \\ k_{\beta_{\text{servo}}} \beta \end{bmatrix} - \begin{bmatrix} c_h \dot{h} \\ c_\alpha \dot{\alpha} \\ c_{\beta_{\text{servo}}} \dot{\beta} \end{bmatrix} + \begin{bmatrix} -L \\ M \\ k_{\beta_{\text{servo}}} u_\beta \end{bmatrix}, \tag{4.26}$$

The full nonlinear equations of motion are then:

$$\begin{bmatrix} m_h + m_\alpha + m_\beta & \xi_1 & m_\beta r_\beta \cos(\alpha + \beta) \\ \xi_1 & \xi_2 & \hat{I}_\beta + L_\beta m_\beta r_\beta \cos(\beta) \\ m_\beta r_\beta \cos(\alpha + \beta) & \hat{I}_\beta + L_\beta m_\beta r_\beta \cos(\beta) & \hat{I}_\beta \end{bmatrix} \begin{bmatrix} \ddot{h} \\ \ddot{\alpha} \\ \ddot{\beta} \end{bmatrix}$$

$$+ \begin{bmatrix} k_h h + c_h \dot{h} - \left(\dot{\alpha} + \dot{\beta}\right)^2 m_\beta r_\beta \sin(\alpha + \beta) - \dot{\alpha}^2 \sin(\alpha) \left(m_\alpha r_\alpha + m_\beta L_\beta\right) \\ k_\alpha \alpha + c_\alpha \dot{\alpha} - \dot{\beta} \left(\dot{\beta} + 2\dot{\alpha}\right) m_\beta r_\beta L_\beta \sin(\beta) \\ k_{\beta_{\text{servo}}} \beta + c_{\beta_{\text{servo}}} \dot{\beta} + \dot{\alpha}^2 m_\beta r_\beta L_\beta \sin(\beta) \end{bmatrix}$$

$$= \begin{bmatrix} -L \\ M \\ k_{\beta_{\text{servo}}} u_\beta \end{bmatrix} \tag{4.27}$$

where:

$\xi_1 = \left(m_\alpha r_\alpha + m_\beta L_\beta\right) \cos(\alpha) + m_\beta r_\beta \cos(\alpha + \beta)$, and

$\xi_2 = \hat{I}_\alpha + \hat{I}_\beta + m_\beta L_\beta^2 + 2L_\beta m_\beta r_\beta \cos(\beta)$.

To the authors knowledge, these full nonlinear equations of motion have not been published previously. However, when linearised using small angle approximations they are similar to some previously published three degree-of-freedom models such as those in Olds (1997), Cox (2003), and Silva and Júnior (2006), with the main differences being those authors

normalise the plunge states against the half-chord length, b, and the neglection of damping.

Furthermore, as the work by Olds (1997), and Silva and Júnior (2006) was theoretical, there was no need to differentiate between the rotational and translational masses as was done here. Though the work by Cox (2003) included experimental results, it is unclear if this differentiation between masses was performed.

Compared to the linearised equations of motion from previous NATA works such as those by Strganac et al. (2000), and Platanitis and Strganac (2004), Equation (4.27) captures the coupling between pitch and plunge in the same manner, with the addition of the trailing-edge dynamics, providing confidence in the equations.

4.4.1.2 Newton-Euler iteration

In order to provide confidence the nonlinear equations of motion, Equation (4.27), the equations of motion will now be derived using an alternative procedure and be shown to be the same.

Newton-Euler iteration is a general procedure for calculating the equations of motion for a multi-body system. It involves an outward iteration over all the links from a base section, during which the linear and angular accelerations, and hence inertial forces and moments, are calculated. These inertial forces and moments are then transferred between joints during an inward iteration. A more thorough description of Newton-Euler iteration is given in Craig (2005).

Starting at the carriage during the outward iteration, the angular velocity and acceleration, and the translational acceleration at the location of frame 1 are

$$\boldsymbol{\omega}_1 = \begin{bmatrix} 0 & 0 & 0 \end{bmatrix}^{\mathrm{T}}, \tag{4.28}$$

$$\boldsymbol{\omega}_1 = \begin{bmatrix} 0 & 0 & 0 \end{bmatrix}^{\mathrm{T}}, \text{ and} \tag{4.29}$$

$$\mathbf{v}_1 = \begin{bmatrix} 0 & \ddot{h} & 0 \end{bmatrix}^{\mathrm{T}} \tag{4.30}$$

respectively. Since the location of frame 1 corresponds to the centre of mass of the carriage, the acceleration at the centre of mass is:

$$\mathbf{v}_{c_1} = \mathbf{v}_1. \tag{4.31}$$

The inertial force and moment on the carriage are then:

$$\mathbf{F}_1 = m_h \mathbf{v}_{c_1} = \begin{bmatrix} 0 & m_h \ddot{h} & 0 \end{bmatrix}^{\mathsf{T}}, \text{ and} \tag{4.32}$$

$$\mathbf{N}_1 = \begin{bmatrix} 0 & 0 & 0 \end{bmatrix}^{\mathsf{T}} \tag{4.33}$$

respectively.

Moving outward, the angular velocity and acceleration, and translational acceleration at frame 2 on the wing body are:

$$\boldsymbol{\omega}_2 = \begin{bmatrix} 0 & 0 & \alpha \end{bmatrix}^{\mathsf{T}}, \tag{4.34}$$

$$\dot{\boldsymbol{\omega}}_2 = \begin{bmatrix} 0 & 0 & \ddot{\alpha} \end{bmatrix}^{\mathsf{T}}, \text{ and} \tag{4.35}$$

$$\mathbf{v}_2 = {}_1^2\mathbf{R}\mathbf{v}_1 = \begin{bmatrix} \ddot{h}\sin(\alpha) & \ddot{h}\cos(\alpha) & 0 \end{bmatrix}^{\mathsf{T}} \tag{4.36}$$

respectively, where:

${}_1^2\mathbf{R}$ is the rotation matrix defined in Equation (4.10).

The translational acceleration at the centre of mass of the wing is

$$\begin{aligned} \mathbf{v}_{c_2} &= \dot{\boldsymbol{\omega}}_2 \times \begin{bmatrix} r_\alpha & 0 & 0 \end{bmatrix}^{\mathsf{T}} + \boldsymbol{\omega}_2 \times \begin{bmatrix} r_\alpha & 0 & 0 \end{bmatrix}^{\mathsf{T}} \times \boldsymbol{\omega}_2 + \mathbf{v}_2 \\ &= \begin{bmatrix} \ddot{h}\sin(\alpha) - \alpha^2 r_\alpha & \ddot{h}\cos(\alpha) + \ddot{\alpha}r_\alpha & 0 \end{bmatrix}^{\mathsf{T}}. \end{aligned} \tag{4.37}$$

The inertial force and moment on the wing are then:

$$\begin{aligned} \mathbf{F}_2 &= m_\alpha \mathbf{v}_{c_2} \\ &= \begin{bmatrix} \ddot{h}m_\alpha\sin(\alpha) - \alpha^2 m_\alpha r_\alpha & \ddot{h}m_\alpha\cos(\alpha) + \ddot{\alpha}m_\alpha r_\alpha & 0 \end{bmatrix}^{\mathsf{T}}, \text{ and} \end{aligned} \tag{4.38}$$

$$\mathbf{N}_2 = \mathbf{I}_2 \dot{\boldsymbol{\omega}}_2 + \boldsymbol{\omega}_2 \times \mathbf{I}_2 \boldsymbol{\omega}_2 = \begin{bmatrix} 0 & 0 & \ddot{\alpha} I_\alpha \end{bmatrix}^{\mathsf{T}}. \tag{4.39}$$

Continuing outward, the angular velocity and acceleration, and translational acceleration of the trailing-edge surface, frame 3, are:

$$\boldsymbol{\omega}_3 = {}_2^3\mathbf{R}\boldsymbol{\omega}_2 + \begin{bmatrix} 0 & 0 & \beta \end{bmatrix}^{\mathsf{T}} = \begin{bmatrix} 0 & 0 & \alpha + \beta \end{bmatrix}, \tag{4.40}$$

$$\begin{aligned} \dot{\boldsymbol{\omega}}_3 &= {}_2^3\mathbf{R}\dot{\boldsymbol{\omega}}_2 + {}_2^3\mathbf{R}\boldsymbol{\omega}_2 \times \begin{bmatrix} 0 & 0 & \beta \end{bmatrix}^{\mathsf{T}} + \begin{bmatrix} 0 & 0 & \ddot{\beta} \end{bmatrix}^{\mathsf{T}} \\ &= \begin{bmatrix} 0 & 0 & \ddot{\alpha} + \ddot{\beta} \end{bmatrix}^{\mathsf{T}}, \text{ and} \end{aligned} \tag{4.41}$$

$$\begin{aligned} \mathbf{v}_3 &= {}_2^3\mathbf{R}\left(\dot{\boldsymbol{\omega}}_2 \times \begin{bmatrix} L_\beta & 0 & 0 \end{bmatrix}^{\mathsf{T}} + \boldsymbol{\omega}_2 \times \begin{bmatrix} L_\beta & 0 & 0 \end{bmatrix}^{\mathsf{T}} \times \boldsymbol{\omega}_2 + \mathbf{v}_2 \right) \\ &= \begin{bmatrix} \ddot{h}\sin(\alpha + \beta) - \alpha^2 L_\beta \cos(\beta) + \ddot{\alpha}L_\beta \sin(\beta) \\ \ddot{h}\cos(\alpha + \beta) + \alpha^2 L_\beta \sin(\beta) + \ddot{\alpha}L_\beta \cos(\beta) \\ 0 \end{bmatrix} \end{aligned} \tag{4.42}$$

where:

$^3_2\mathbf{R}$ is the rotation matrix defined in Equation (4.16).

The translational acceleration at the centre of mass of the trailing-edge surface is then:

$$\mathbf{v}_{c_3} = \boldsymbol{\omega}_3 \times \begin{bmatrix} r_\beta & 0 & 0 \end{bmatrix}^\mathrm{T} + \boldsymbol{\omega}_3 \times \begin{bmatrix} r_\beta & 0 & 0 \end{bmatrix}^\mathrm{T} \times \boldsymbol{\omega}_3 + \mathbf{v}_3 \qquad (4.43)$$

where the expanded form has been omitted for brevity. The inertial force and moment acting on the trailing-edge section are then:

$$\mathbf{F}_3 = m_\beta \mathbf{v}_{c_3}, \text{ and} \qquad (4.44)$$

$$\mathbf{N}_3 = \mathbf{I}_3 \boldsymbol{\omega}_3 + \boldsymbol{\omega}_3 \times \mathbf{I}_3 \boldsymbol{\omega}_3 \qquad (4.45)$$

respectively.

The inward iteration is started at the outermost body, with the forces and moments calculated at each of the joints. Thus, starting at the trailing-edge surface, the force and moment acting on its joint are:

$$\mathbf{f}_3 = \mathbf{F}_3, \text{ and} \qquad (4.46)$$

$$\mathbf{n}_3 = \mathbf{N}_3 + \begin{bmatrix} r_\beta & 0 & 0 \end{bmatrix}^\mathrm{T}. \qquad (4.47)$$

Moving inward, the force and moment acting at the joint between the wing and the carriage are:

$$\mathbf{f}_2 = {}^3_2\mathbf{R}^\mathrm{T} \mathbf{f}_3, \text{ and} \qquad (4.48)$$

$$\mathbf{n}_2 = \mathbf{N}_2 + {}^3_2\mathbf{R}^\mathrm{T} \mathbf{n}_3 + \begin{bmatrix} r_\alpha & 0 & 0 \end{bmatrix}^\mathrm{T} \times \mathbf{F}_2 + \begin{bmatrix} L_\beta & 0 & 0 \end{bmatrix}^\mathrm{T} \times {}^3_2\mathbf{R}^\mathrm{T} \mathbf{f}_3 \qquad (4.49)$$

Lastly moving inward to the carriage, the force acting on the prismatic joint to the ground (the spring) is:

$$\mathbf{f}_1 = {}^2_1\mathbf{R}^\mathrm{T} \mathbf{f}_2 + \mathbf{F}_1. \qquad (4.50)$$

The moment is not calculated as it is not required.

The equations of motion are then constructed by taking the component of the force or moment vectors in Equations (4.47), (4.49) and (4.50) acting at the joints, and equating them to the forces and moments acting at these joints:

$$\begin{bmatrix} \mathbf{f}_1(2) \\ \mathbf{n}_2(3) \\ \mathbf{n}_3(3) \end{bmatrix} = - \begin{bmatrix} c_h h \\ c_\alpha \alpha \\ c_{\beta_{\text{servo}}} \beta \end{bmatrix} - \begin{bmatrix} k_h h \\ k_\alpha \alpha \\ k_{\beta_{\text{servo}}} \beta \end{bmatrix} + \begin{bmatrix} -L \\ M \\ k_{\beta_{\text{servo}}} \mathbf{u}_\beta \end{bmatrix}. \qquad (4.51)$$

When expanded, these equations of motion are identical to those shown in Equation (4.27).

4.4.1.3 Linearised equations of motion and state-space form

The equations of motion can be linearised using small angle approximations for all the trigonometric terms. This produces the linearised three degree-of-freedom equation of motion, including the quasi-steady aerodynamics, Equations (4.4) and (4.5),

$$
\underbrace{\begin{bmatrix} m_h + m_\alpha + m_\beta & m_\alpha r_\alpha + m_\beta r_\beta + m_\beta L_\beta & m_\beta r_\beta \\ m_\alpha r_\alpha + m_\beta r_\beta + m_\beta L_\beta & \hat{I}_\alpha + \hat{I}_\beta + m_\beta L_\beta^2 + 2L_\beta m_\beta r_\beta & \hat{I}_\beta + L_\beta m_\beta r_\beta \\ m_\beta r_\beta & \hat{I}_\beta + L_\beta m_\beta r_\beta & \hat{I}_\beta \end{bmatrix}}_{\mathbf{M}_{\text{eom}}} \begin{bmatrix} \ddot{h} \\ \ddot{\alpha} \\ \ddot{\beta} \end{bmatrix}
$$

$$
+ \underbrace{\begin{bmatrix} c_h + \rho b S C_{l_\alpha} U & \rho b S r_{3c/4} C_{l_\alpha} U & 0 \\ -\rho b^2 S C_{m_{\alpha,\text{eff.}}} U & c_\alpha - \rho b^2 S r_{3c/4} C_{m_{\alpha,\text{eff.}}} U & 0 \\ 0 & 0 & c_{\beta_{\text{servo}}} \end{bmatrix}}_{\mathbf{C}_{\text{eom}}} \begin{bmatrix} h \\ \alpha \\ \beta \end{bmatrix}
$$

$$
+ \underbrace{\begin{bmatrix} k_h & \rho b S C_{l_\alpha} U^2 & \rho b S C_{l_\beta} U^2 \\ 0 & k_\alpha(\alpha) - \rho b^2 S C_{m_{\alpha,\text{eff.}}} U^2 & -\rho b^2 S C_{m_{\beta,\text{eff.}}} U^2 \\ 0 & 0 & k_{\beta_{\text{servo}}} \end{bmatrix}}_{\mathbf{K}_{\text{eom}}} \begin{bmatrix} h \\ \alpha \\ \beta \end{bmatrix} = \underbrace{\begin{bmatrix} 0 \\ 0 \\ k_{\beta_{\text{servo}}} \end{bmatrix}}_{\mathbf{F}_{\text{eom}}} \mathbf{u}, \quad (4.52)
$$

where:

$\mathbf{M}_{\text{eom}}$ is the mass matrix of the equation of motion,

$\mathbf{C}_{\text{eom}}$ is the damping matrix of the equation of motion,

$\mathbf{K}_{\text{eom}}$ is the stiffness matrix of the equation of motion, and

$\mathbf{F}_{\text{eom}}$ is the forcing matrix of the equation of motion.

The three degree-of-freedom dynamics can be rearranged into a state-space form using the equation of motion matrices defined above. Defining the state-vector as:

$$
\mathbf{x} = \begin{bmatrix} h & \alpha & \beta & h & \alpha & \beta \end{bmatrix}^{\mathsf{T}}, \tag{4.53}
$$

the state matrix is:

$$
\mathbf{A}(U, \alpha) = \begin{bmatrix} -\mathbf{M}_{\text{eom}}^{-1} \mathbf{C}_{\text{eom}}(U) & -\mathbf{M}_{\text{eom}}^{-1} \mathbf{K}_{\text{eom}}(U, \alpha) \\ \mathbf{I} & \mathbf{0} \end{bmatrix}, \tag{4.54}
$$

and has the Linear Parameter Varying (LPV) form

$$
\mathbf{A}(U, \alpha) = \mathbf{A}_{p0} + \mathbf{A}_{p1} U + \mathbf{A}_{p2} U^2 + \mathbf{A}_{p3} k_\alpha(\alpha). \tag{4.55}
$$

The input matrix is parameter independent, and is

$$
\mathbf{B} = \begin{bmatrix} \mathbf{M}_{\text{eom}}^{-1} \mathbf{F}_{\text{eom}} \\ \mathbf{0} \end{bmatrix}. \tag{4.56}
$$

The output and feed-through matrices depend upon the system outputs. With the optical encoders on the NATA we can directly measure pitch, plunge and trailing-edge surface deflection, thus the output vector is $\mathbf{y} = [h \quad \alpha \quad \beta]^{\mathrm{T}}$, and the output and feed-through matrices are respectively:

$$\mathbf{C} = \begin{bmatrix} \mathbf{0} & \mathbf{I} \end{bmatrix}, \text{ and } \mathbf{D} = \mathbf{0}. \tag{4.57}$$

When assuming full-state output, as described in Section 4.3, the output vector is $\mathbf{y} = [h \quad \alpha \quad \beta \quad \dot{h} \quad \dot{\alpha} \quad \dot{\beta}]^{\mathrm{T}}$, and the output and feed-through matrices are respectively:

$$\mathbf{C} = \mathbf{I}, \text{ and } \mathbf{D} = \mathbf{0}. \tag{4.58}$$

When compared to the dynamic model used in previous two degree-of-freedom aeroelastic systems, such as those by Strganac et al. (2000), and Platanitis and Strganac (2004), the state-space model presented here includes the dynamics of the trailing-edge control surface and its servo-motor, and explicitly includes the quasi-steady aerodynamic model.

4.4.2 Four degree-of-freedom model

With a leading-edge control surface attached to the wing, a similar procedure to that followed in Section 4.4.1 can be followed to derive a four degree-of-freedom model.

Firstly, the dynamic states are labelled the same as for the three degree-of-freedom model with the addition of the leading-edge deflection, γ. These dynamic states as well as the dimensions are shown in Figure 4.8.

The aerodynamic model is again the quasi-steady model used previously, but with the addition of a leading-edge term (Platanitis and Strganac 2004):

$$L = \rho U^2 bS C_{l_\alpha} \left(\alpha + \frac{\dot{h}}{U} + r_{3c/4}\frac{\dot{\alpha}}{U} \right) + \rho U^2 bS C_{l_\beta} \beta + \rho U^2 bS C_{l_\gamma} \gamma, \tag{4.59}$$

$$M = \rho U^2 b^2 S C_{m_{\alpha,\text{eff.}}} \left(\alpha + \frac{\dot{h}}{U} + r_{3c/4}\frac{\dot{\alpha}}{U} \right) + \rho U^2 b^2 S C_{m_{\beta,\text{eff.}}} \beta + \rho U^2 b^2 S C_{m_{\gamma,\text{eff.}}} \gamma, \tag{4.60}$$

where
$C_{l_\gamma} = \frac{\partial C_l}{\partial \gamma}$ is the leading-edge lift coefficient about the elastic axis, and
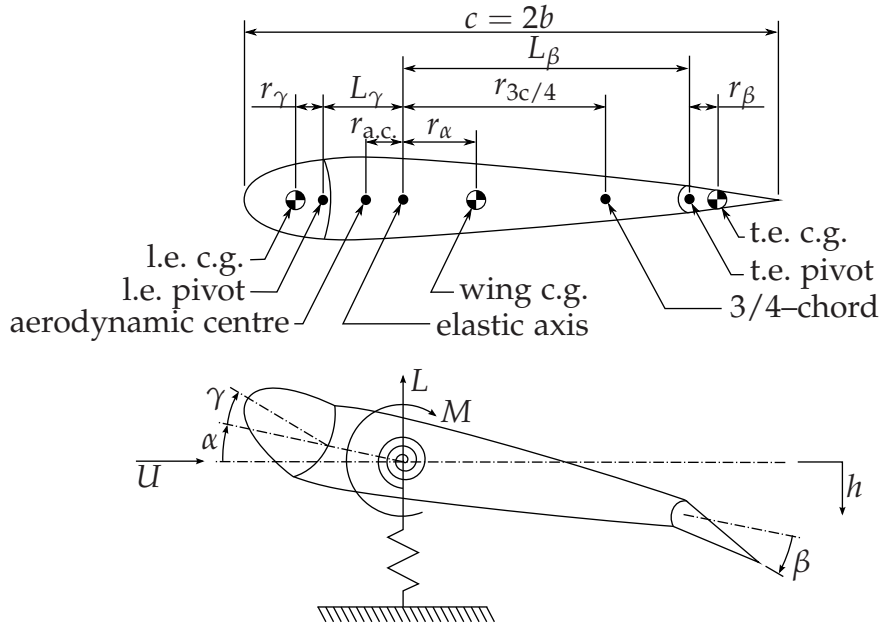
Figure 4.8: Four degree-of-freedom NATA model showing states and dimensions.

$C_{m_{\gamma,\text{eff.}}} = 2\frac{\partial C_m}{\partial \gamma} + \frac{r_{\text{a.c.}}}{b}C_{l_\gamma}$ is the leading-edge moment coefficient about the elastic axis.

The reference frames used for the derivation of the four degree-of-freedom dynamics are shown in Figure 4.9.

In the following sections the dynamics are again derived using both the Lagrangian energy method and Newton-Euler iteration, before being linearised and converted to state-space form.
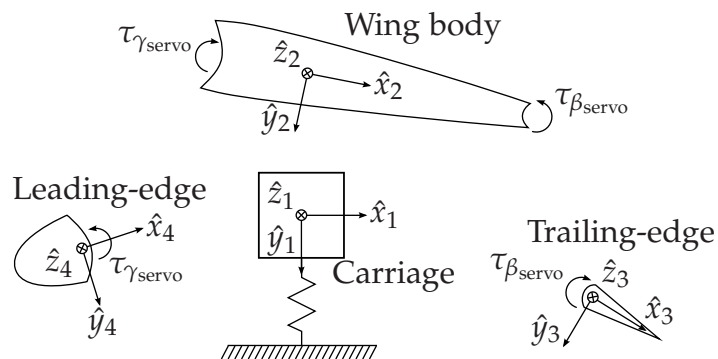
Figure 4.9: Reference frames for the four degree-of-freedom model.

4.4.2.1 Lagrangian energy method

The initial part of this Lagrangian derivation is identical to that for the three degree-of-freedom model presented in Section 4.4.1.1. The steps from Equation (4.6) to Equation (4.21) are used in this four degree-of-freedom derivation at this point, but have been omitted for the sake of brevity.

Continuing the derivation, the transformation from frame 2 to 4 is a rotation about $\hat{z}_2$ by amount γ. This is described by the transformation matrix:

$$
{}^4_2\mathbf{R} = \begin{bmatrix} \cos(\gamma) & \sin(\gamma) & 0 \\ -\sin(\gamma) & \cos(\gamma) & 0 \\ 0 & 0 & 1 \end{bmatrix}. \tag{4.61}
$$

The translational and angular velocity of frame 4 are then:

$$
\mathbf{v}_4 = {}^4_2\mathbf{R}\mathbf{v}_2 + {}^4_2\mathbf{R}(\omega_2 \times \begin{bmatrix} L_\gamma & 0 & 0 \end{bmatrix}^\mathsf{T}) \tag{4.62}
$$

$$
= \begin{bmatrix} h\sin(\alpha + \gamma) + \alpha L_\gamma \sin(\gamma) \\ h\cos(\alpha + \gamma) + \alpha L_\gamma \cos(\gamma) \\ 0 \end{bmatrix}^\mathsf{T}, \text{ and} \tag{4.63}
$$

$$
\omega_4 = {}^4_2\mathbf{R}\omega_2 + \begin{bmatrix} 0 & 0 & \gamma \end{bmatrix}^\mathsf{T} = \begin{bmatrix} 0 & 0 & \alpha + \gamma \end{bmatrix}^\mathsf{T}. \tag{4.64}
$$

The velocity at the centre of mass of the leading-edge section is then:

$$
\mathbf{v}_{c_4} = \mathbf{v}_4 + \omega_4 \times \begin{bmatrix} r_\gamma \\ 0 \\ 0 \end{bmatrix} = \begin{bmatrix} h\sin(\gamma + \alpha) + \alpha L_\gamma \sin(\gamma) \\ h\cos(\gamma + \alpha) + \alpha L_\gamma \cos(\gamma) + r_\gamma\alpha + r_\gamma\gamma \\ 0 \end{bmatrix}. \tag{4.65}
$$

As before, the potential and kinetic energies are calculated as:

$$
V_4 = 0, \text{ and} \tag{4.66}
$$

$$
T_4 = \tfrac{1}{2}\mathbf{v}_{c_4}^\mathsf{T} m_\gamma \mathbf{v}_{c_4} + \tfrac{1}{2}\omega_4^\mathsf{T}\mathbf{I}_4\omega_4, \tag{4.67}
$$

where:

m_γ [kg] is the mass of the leading-edge,

$\mathbf{I}_4$ is the principle moment of inertia matrix of the leading-edge located at the centre of mass of the leading-edge, with $\mathbf{I}_4 = \mathrm{diag}(0, 0, I_\gamma)$, and

I_γ [kg·m^2] is the leading-edge rotational moment of inertia about the $\hat{z}_4$ axis and located at its centre of mass.

Once again the expanded kinetic energy term has been omitted for the sake of brevity.

This time the Lagrangian is:

$$\mathcal{L} = (T_1 + T_2 + T_3 + T_4) - (V_1 + V_2 + V_3 + V_4). \tag{4.68}$$

Replacing the leading-edge inertia term with the apparent inertia at the joint calculated using the parallel-axis theorem,

$$\hat{I}_\gamma = I_\gamma + m_\gamma r_\gamma^2, \tag{4.69}$$

the leading-edge servo motor dynamics are assumed to be a second-order system of the form

$$\hat{I}_\gamma \ddot{\gamma} + c_{\gamma_{\text{servo}}} \gamma + k_{\gamma_{\text{servo}}} \gamma = k_{\gamma_{\text{servo}}} u_\gamma, \tag{4.70}$$

where:

$c_{\gamma_{\text{servo}}}$ [Nm·s/rad] is the virtual damping provided by the leading-edge servo motor,

$k_{\gamma_{\text{servo}}}$ [Nm/rad] is the virtual stiffness provided by the leading-edge servo motor, and

u_γ [rad] is the leading-edge servo-motor control signal.

Along with the trailing-edge servo-motor dynamic model from Equation (4.25), and with the four degree-of-freedom control signal defined as $\mathbf{u} = [u_\beta \quad u_\gamma]^{\mathrm{T}}$, the equations of motion for the entire system are

$$\frac{d}{dt} \begin{bmatrix} \frac{\partial \mathcal{L}}{\partial h} \\ \frac{\partial \mathcal{L}}{\partial \alpha} \\ \frac{\partial \mathcal{L}}{\partial \beta} \\ \frac{\partial \mathcal{L}}{\partial \gamma} \end{bmatrix} - \begin{bmatrix} \frac{\partial \mathcal{L}}{\partial h} \\ \frac{\partial \mathcal{L}}{\partial \alpha} \\ \frac{\partial \mathcal{L}}{\partial \beta} \\ \frac{\partial \mathcal{L}}{\partial \gamma} \end{bmatrix} = - \begin{bmatrix} 0 \\ 0 \\ k_{\beta_{\text{servo}}} \beta \\ k_{\gamma_{\text{servo}}} \gamma \end{bmatrix} - \begin{bmatrix} c_h h \\ c_\alpha \alpha \\ c_{\beta_{\text{servo}}} \beta \\ c_{\gamma_{\text{servo}}} \gamma \end{bmatrix} + \begin{bmatrix} -L \\ M \\ k_{\beta_{\text{servo}}} u_\beta \\ k_{\gamma_{\text{servo}}} u_\gamma \end{bmatrix}, \tag{4.71}$$

and in expanded form are

$$\begin{bmatrix} m_h + m_\alpha + m_\beta + m_\gamma & \xi_3 & m_\beta r_\beta \cos(\alpha + \beta) & m_\gamma r_\gamma \cos(\alpha + \gamma) \\ \xi_3 & \xi_4 & \hat{I}_\beta + L_\beta m_\beta r_\beta \cos(\beta) & \hat{I}_\gamma + L_\gamma m_\gamma r_\gamma \cos(\gamma) \\ m_\beta r_\beta \cos(\alpha + \beta) & \hat{I}_\beta + L_\beta m_\beta r_\beta \cos(\beta) & \hat{I}_\beta & 0 \\ m_\gamma r_\gamma \cos(\alpha + \gamma) & \hat{I}_\gamma + L_\gamma m_\gamma r_\gamma \cos(\gamma) & 0 & \hat{I}_\gamma \end{bmatrix} \begin{bmatrix} \ddot{h} \\ \ddot{\alpha} \\ \ddot{\beta} \\ \ddot{\gamma} \end{bmatrix}$$

$$+ \begin{bmatrix} k_h h + c_h h - (\alpha + \beta)^2 m_\beta r_\beta \sin(\alpha + \beta) - (\alpha + \gamma)^2 m_\gamma r_\gamma \sin(\alpha + \gamma) - \alpha^2 \sin(\alpha) \left(m_\alpha r_\alpha + m_\beta L_\beta + m_\gamma L_\gamma \right) \\ k_\alpha \alpha + c_\alpha \alpha - \beta \left(\beta + 2\alpha \right) m_\beta r_\beta L_\beta \sin(\beta) - \gamma \left(\gamma + 2\alpha \right) m_\gamma r_\gamma L_\gamma \sin(\gamma) \\ k_{\beta_{\text{servo}}} \beta + c_{\beta_{\text{servo}}} \beta + \alpha^2 m_\beta r_\beta L_\beta \sin(\beta) \\ k_{\gamma_{\text{servo}}} \gamma + c_{\gamma_{\text{servo}}} \gamma + \alpha^2 m_\gamma r_\gamma L_\gamma \sin(\gamma) \end{bmatrix}$$

$$= \begin{bmatrix} -L \\ M \\ k_{\beta_{\text{servo}}} u_\beta \\ k_{\gamma_{\text{servo}}} u_\gamma \end{bmatrix}, \tag{4.72}$$

where:
$$\xi_3 = \left(m_\alpha r_\alpha + m_\beta L_\beta + m_\gamma L_\gamma\right)\cos(\alpha) + m_\beta r_\beta \cos(\alpha + \beta) + m_\gamma r_\gamma \cos(\alpha + \gamma),$$
and
$$\xi_4 = \hat{I}_\alpha + \hat{I}_\beta + \hat{I}_\gamma + m_\beta L_\beta^2 + m_\gamma L_\gamma^2 + 2L_\beta m_\beta r_\beta \cos(\beta) + 2L_\gamma m_\gamma r_\gamma \cos(\gamma).$$

Again, to the authors knowledge, these full nonlinear four degree-of-freedom equations of motion have not been published, and the four degree-of-freedom aeroelasticity control work by Vepa (2007) mentioned in Section 3.2.1 omitted the details of their mechanical model.

However, the structure of these equations of motion is very similar to those presented in Equation (4.27), with the extension to the leading-edge surface dynamics.

4.4.2.2 Newton-Euler iteration

As with the three degree-of-freedom equations of motion, the four degree-of-freedom equations of motion will now be derived using the Newton-Euler iteration method to provide confidence in the derived equations of motion.

The Newton-Euler iteration method for deriving the four degree-of-freedom equations of motion follows that for the three degree-of-freedom model from Equation (4.28) to Equation (4.43), and is omitted for the sake of brevity.

Continuing the derivation during the outward iteration, the angular velocity and acceleration and linear acceleration of the leading-edge are:

$$\omega_4 = {}^4_2\mathbf{R}\omega_2 + \begin{bmatrix} 0 & 0 & \dot{\gamma} \end{bmatrix}^{\mathrm{T}} = \begin{bmatrix} 0 & 0 & \dot{\alpha} + \dot{\gamma} \end{bmatrix}, \tag{4.73}$$

$$\dot{\omega}_4 = {}^4_2\mathbf{R}\dot{\omega}_2 + {}^3_2\mathbf{R}\omega_2 \times \begin{bmatrix} 0 & 0 & \dot{\gamma} \end{bmatrix}^{\mathrm{T}} + \begin{bmatrix} 0 & 0 & \ddot{\gamma} \end{bmatrix}^{\mathrm{T}}$$
$$= \begin{bmatrix} 0 & 0 & \ddot{\alpha} + \ddot{\gamma} \end{bmatrix}^{\mathrm{T}}, \text{ and} \tag{4.74}$$

$$\mathbf{v}_4 = {}^4_2\mathbf{R}\left(\omega_2 \times \begin{bmatrix} L_\gamma & 0 & 0 \end{bmatrix}^{\mathrm{T}} + \omega_2 \times \begin{bmatrix} L_\gamma & 0 & 0 \end{bmatrix}^{\mathrm{T}} \times \omega_2 + \mathbf{v}_2\right)$$
$$= \begin{bmatrix} \ddot{h}\sin(\alpha + \gamma) - \dot{\alpha}^2 L_\gamma \cos(\gamma) + \ddot{\alpha}L_\gamma \sin(\gamma) \\ \ddot{h}\cos(\alpha + \gamma) + \dot{\alpha}^2 L_\gamma \sin(\gamma) + \ddot{\alpha}L_\gamma \cos(\gamma) \\ 0 \end{bmatrix} \tag{4.75}$$

where:
${}^4_2\mathbf{R}$ is the rotation matrix defined in Equation (4.61).

The translational acceleration at the centre of mass of the leading-edge section is then:

$$\mathbf{v}_{c_4} = \boldsymbol{\omega}_4 \times \begin{bmatrix} r_\gamma & 0 & 0 \end{bmatrix}^\mathrm{T} + \boldsymbol{\omega}_4 \times \begin{bmatrix} r_\gamma & 0 & 0 \end{bmatrix}^\mathrm{T} \times \boldsymbol{\omega}_4 + \mathbf{v}_4. \qquad (4.76)$$

The inertial force and moment on the leading-edge section at its centre of mass is then:

$$\mathbf{F}_4 = m_\gamma \mathbf{v}_{c_4}, \text{ and} \qquad (4.77)$$

$$\mathbf{N}_4 = \mathbf{I}_4 \boldsymbol{\omega}_4 + \boldsymbol{\omega}_4 \times \mathbf{I}_4 \boldsymbol{\omega}_4 \qquad (4.78)$$

respectively.

Starting the inward iteration at the leading-edge surface, the force and moment acting at the joint between it and the wing body are:

$$\mathbf{f}_4 = \mathbf{F}_4, \text{ and} \qquad (4.79)$$

$$\mathbf{n}_4 = \mathbf{N}_4 + \begin{bmatrix} r_\gamma & 0 & 0 \end{bmatrix}^\mathrm{T}. \qquad (4.80)$$

The force and moment from the trailing-edge surface acting at the joint between it and the wing body is the same as for the three degree-of-freedom case, as given in Equations (4.46) and (4.47).

This time the force and moment acting at the joint between the wing body and the carriage have contributions from both the leading- and trailing-edge surfaces:

$$\mathbf{f}_2 = {}^4_2\mathbf{R}^\mathrm{T}\mathbf{f}_4 + {}^3_2\mathbf{R}^\mathrm{T}\mathbf{f}_3, \text{ and} \qquad (4.81)$$

$$\begin{aligned} \mathbf{n}_2 = \mathbf{N}_2 + {}^4_2\mathbf{R}^\mathrm{T}\mathbf{n}_4 + {}^3_2\mathbf{R}^\mathrm{T}\mathbf{n}_3 + \begin{bmatrix} r_\alpha & 0 & 0 \end{bmatrix}^\mathrm{T} \times \mathbf{F}_2 \\ + \begin{bmatrix} L_\gamma & 0 & 0 \end{bmatrix}^\mathrm{T} \times {}^4_2\mathbf{R}^\mathrm{T}\mathbf{f}_4 + \begin{bmatrix} L_\beta & 0 & 0 \end{bmatrix}^\mathrm{T} \times {}^3_2\mathbf{R}^\mathrm{T}\mathbf{f}_3 \qquad (4.82) \end{aligned}$$

Lastly, the force acting at the prismatic joint between the carriage and the ground is calculated as per the three degree-of-freedom example:

$$\mathbf{f}_1 = {}^2_1\mathbf{R}^\mathrm{T}\mathbf{f}_2 + \mathbf{F}_1. \qquad (4.83)$$

The four degree-of-freedom equations of motion are constructed by extracting the dimension that corresponds to the freedom in the joint in the same way as was done for the three degree-of-freedom case:

$$\begin{bmatrix} \mathbf{f}_1(2) \\ \mathbf{n}_2(3) \\ \mathbf{n}_3(3) \\ \mathbf{n}_4(3) \end{bmatrix} = - \begin{bmatrix} c_h h \\ c_\alpha \alpha \\ c_{\beta_\text{servo}} \beta \\ c_{\gamma_\text{servo}} \gamma \end{bmatrix} - \begin{bmatrix} k_h h \\ k_\alpha \alpha \\ k_{\beta_\text{servo}} \beta \\ k_{\gamma_\text{servo}} \gamma \end{bmatrix} + \begin{bmatrix} -L \\ M \\ k_{\beta_\text{servo}} u_\beta \\ k_{\gamma_\text{servo}} u_\gamma \end{bmatrix}. \qquad (4.84)$$

When expanded, this expression yields exactly the same equations of motion, Equation (4.72) as the Lagrangian energy method.

4.4.2.3 Linearised equations of motion and state-space form

Again using a small-angle approximation to linearise the dynamics, the four degree-of-freedom dynamics, including the quasi-steady aerodynamics Equations (4.59) and (4.60) are:

$$
\underbrace{\begin{bmatrix} m_h + m_\alpha + m_\beta + m_\gamma & \xi_5 & m_\beta r_\beta & m_\gamma r_\gamma \\ \xi_5 & \xi_6 & \hat{I}_\beta + L_\beta m_\beta r_\beta & \hat{I}_\gamma + L_\gamma m_\gamma r_\gamma \\ m_\beta r_\beta & \hat{I}_\beta + L_\beta m_\beta r_\beta & \hat{I}_\beta & 0 \\ m_\gamma r_\gamma & \hat{I}_\gamma + L_\gamma m_\gamma r_\gamma & 0 & \hat{I}_\gamma \end{bmatrix}}_{\mathbf{M}_{\text{eom}}} \begin{bmatrix} \ddot{h} \\ \ddot{\alpha} \\ \ddot{\beta} \\ \ddot{\gamma} \end{bmatrix}
$$

$$
+ \underbrace{\begin{bmatrix} c_h + \rho b S C_{l_\alpha} U & \rho b S r_{3c/4} C_{l_\alpha} U & 0 & 0 \\ -\rho b^2 S C_{m_{\alpha,\text{eff.}}} U & c_\alpha - \rho b^2 S r_{3c/4} C_{m_{\alpha,\text{eff.}}} U & 0 & 0 \\ 0 & 0 & c_{\beta_{\text{servo}}} & 0 \\ 0 & 0 & 0 & c_{\gamma_{\text{servo}}} \end{bmatrix}}_{\mathbf{C}_{\text{eom}}} \begin{bmatrix} h \\ \alpha \\ \beta \\ \gamma \end{bmatrix}
$$

$$
+ \underbrace{\begin{bmatrix} k_h & \rho b S C_{l_\alpha} U^2 & \rho b S C_{l_\beta} U^2 & \rho b S C_{l_\gamma} U^2 \\ 0 & k_\alpha(\alpha) - \rho b^2 S C_{m_{\alpha,\text{eff.}}} U^2 & -\rho b^2 S C_{m_{\beta,\text{eff.}}} U^2 & -\rho b^2 S C_{m_{\gamma,\text{eff.}}} U^2 \\ 0 & 0 & k_{\beta_{\text{servo}}} & 0 \\ 0 & 0 & 0 & k_{\gamma_{\text{servo}}} \end{bmatrix}}_{\mathbf{K}_{\text{eom}}} \begin{bmatrix} h \\ \alpha \\ \beta \\ \gamma \end{bmatrix}
$$

$$
= \underbrace{\begin{bmatrix} 0 & 0 \\ 0 & 0 \\ k_{\beta_{\text{servo}}} & 0 \\ 0 & k_{\gamma_{\text{servo}}} \end{bmatrix}}_{\mathbf{F}_{\text{eom}}} \mathbf{u}, \tag{4.85}
$$

where:

$\xi_5 = m_\alpha r_\alpha + m_\beta r_\beta + m_\beta L_\beta + m_\gamma r_\gamma + m_\gamma L_\gamma$, and
$\xi_6 = \hat{I}_\alpha + \hat{I}_\beta + \hat{I}_\gamma + m_\beta L_\beta^2 + 2L_\beta m_\beta r_\beta + m_\gamma L_\gamma^2 + 2L_\gamma m_\gamma r_\gamma$.

The four degree-of-freedom dynamics can be represented in a state-space model in a similar fashion to that described above at the end of Section 4.4.1. Defining the state vector as:

$$
\mathbf{x} = \begin{bmatrix} h & \alpha & \beta & \gamma & h & \alpha & \beta & \gamma \end{bmatrix}^{\text{T}}, \tag{4.86}
$$

the rest of the state-space equations can be constructed in exactly the same way as from Equation (4.54) to Equation (4.58).

Again, compared to the two degree-of-freedom models in previous works, such as those by Strganac et al. (2000), and Platanitis and Strganac (2004), the interaction between the pitch and plunge dynamics is captured, along with the extra contributions due to trailing- and leading-edge control surfaces. Furthermore, this state-space model explicitly includes the servo motor dynamics, and the quasi-steady aerodynamic model.

4.5 NATA parameters

The parameters for the NATA model are detailed below, and were sourced using several methods including direct measurement, system identification, and from previously published data.

4.5.1 Weight

The parameters of the second wing section previously published such as in Platanitis and Strganac (2004), and Platanitis and Strganac (2005) separate the mass into carriage and wing components. However, since a significant proportion of the carriage mass also rotates it is necessary to split the system into translating and rotating masses to correctly capture the inertial coupling.

The rotating and translational masses of the carriage were estimated using estimates for all of the components based on their size and material, as detailed in Table 4.1. It was necessary to estimate the the weights of some components as they could not be easily removed from the apparatus.

The mass of the wing section, including its mounting plate, was measured to be 4.34 kg, including the masses of the leading and trailing-edge control surfaces.

4.5.2 Torsional stiffness

The torsional stiffness was measured by loading the torsional spring with a known moment, then measuring the pitching angle using the relevant encoder. This measured data is shown in Figure 4.10, along with cubic and quintic functions fit to the applied moment data with their coefficients of determination, a measure of the *goodness* of the fit,

Table 4.1: Weight estimates of the carriage.

Translating

Component	Volume (mm^3)	Quantity	Total Weight (kg)
L beam, Al.	$3 \times 30 \times (315 + 2 \times 170 + 2 \times 180)$	1	0.192
Plates, Al.	$4 \times 300 \times 305$	2	1.537
C beam, Al.	$(75 + 2) \times 5 \times 305$	2	0.929
Bearing holder, Steel	$(7^2 - 2^2\pi) \times 15$	2	0.852
Square tube, Al.	$(25^2 - 19^2) \times (2 \times 410 + 1260)$	1	1.153
Linear bearings, Al.	$(20 \times 30 - 6^2\pi) \times 40$	3	0.123
Springs, Steel	$(15^2 - 11^2)\pi \times 20$	3	1.019
Bolts (est. 15.9 g each)		35	0.557
			6.362

Rotating

Component	Volume (mm^3)	Quantity	Total Weight (kg)
Cam (est.)			0.87
Shaft, Steel	$8.5^2\pi \times 300$	1	0.531
Mount plate, Al.	$430 \times 6 \times 102$	1	0.552
Mount collar, Steel	$(50^2 - 8.5^2)\pi \times 50$	1	0.677
Other (est.)			0.5–1.0
			3.13–3.63

calculated using:

$$R^2 = 1 - \frac{\sum (y_i - k_\alpha(\alpha_i))^2}{\sum (y_i - \bar{y})}. \tag{4.87}$$

The applied moment corresponds to the reaction moment of the torsional spring, $k_\alpha(\alpha)\alpha$, so the torsional stiffness functions can be calculated by taking the derivative of the moment functions with respect to α. This yields quartic and quadratic stiffness functions for the quintic and cubic moment functions respectively, which are:

$$k_\alpha(\alpha) = 27.96 - 167.63\alpha + 552.55\alpha^2 + 1589.3\alpha^3 - 3247.2\alpha^4 \tag{4.88}$$

$$k_\alpha(\alpha) = 25.55 - 103.19\alpha + 543.24\alpha^2 \tag{4.89}$$

The quartic stiffness function, Equation (4.88), which was used in many previous studies (Ko and Strganac 1998, and Strganac et al. 2000), fits the measured data better than the quadratic stiffness function, Equation (4.89), across the range of measure data. However, it extrapolates

poorly outside of this range, which can lead to simulation and system-identification instabilities. For this reason the quadratic stiffness function was used in all models, simulations and system-identification.
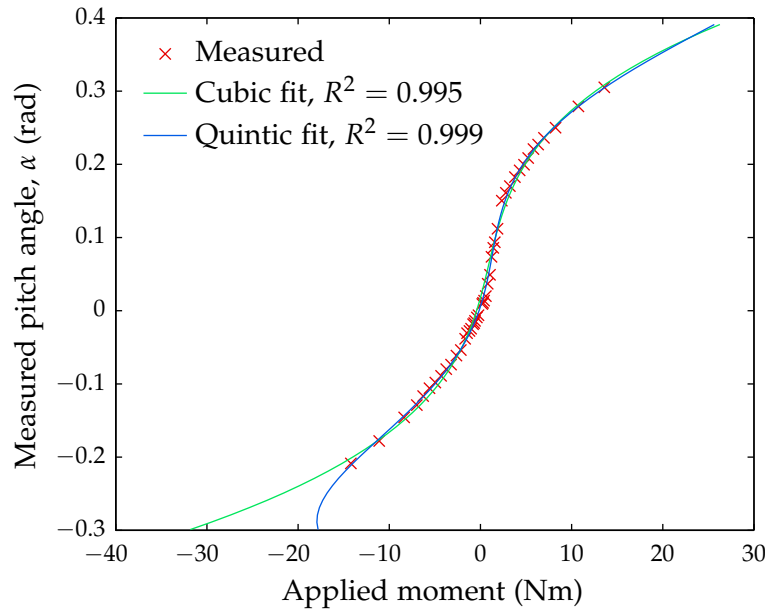

Figure 4.10: Applied moment versus pitch angle measurements and moment functions fit to this data used to calculate the torsional stiffness function. The stiffness functions are calculated by taking the derivative of the moment functions with respect to α, which yields quartic and quadratic stiffness functions.

4.5.3 Wing position

The wing sections are connected to the carriage via a mounting plate on each wing section and on the carriage. The bolt holes in these mounting plates were slotted so that the wing can be moved in the $\hat{x}_2$ direction, from Figures 4.7 and 4.9. This changes the position of the elastic axis of wing relative to the wing, which changes the length of r_α, $r_{a.c.}$, $r_{3c/4}$, L_β and L_γ.

For all experiments the wing was placed in the same position used in Platanitis and Strganac (2004), which corresponds to the dimensions shown in Table 4.2.

Table 4.2: Dimensions resulting from the chosen position of the wing.

r_α	$0.040\,\mathrm{m}$
$r_{3\mathrm{c}/4}$	$0.223\,\mathrm{m}$
$r_{\mathrm{a.c.}}$	$-0.033\,\mathrm{m}$
L_β	$0.233\,\mathrm{m}$
L_γ	$-0.01\,\mathrm{m}$

4.5.4 Aerodynamics

The pitch coefficient of lift for the second wing section was taken from Platanitis and Strganac (2004), and is $C_{l_\alpha} = 6.757$. The effective pitch coefficient of moment at the pivot is calculated due to the lift and moment at the aerodynamic centre:

$$C_{m_{\alpha,\mathrm{eff.}}} = C_{m_\alpha} + \frac{r_{\mathrm{a.c.}}}{b}C_{l_\alpha} \tag{4.90}$$
$$= -1.17,$$

where the coefficient of moment at the aerodynamic centre, $C_{m_\alpha} = 0$ because the aerofoil is symmetric.

The coefficient of moment for both the leading-edge and trailing-edge control surfaces were measured using static deflection tests and corrected using the pitching coefficient of moment. The resulting coefficients of moment are $C_{m_{\beta,\mathrm{eff.}}} = -2.10$, and $C_{m_{\gamma,\mathrm{eff.}}} = 0.127$.

Due to the low plunge displacements experienced, the coefficient of lift due to the leading-edge and trailing-edge control surfaces could not be directly measured, thus the values from Platanitis and Strganac (2004) were used, which are $C_{l_\beta} = 3.774$, and $C_{l_\gamma} = 0.1566$.

4.5.5 Servo motor parameters

The servo motor dynamics were measured by applying a chirp input to each servo, measuring the output response and fitting a second-order state-space model to the data.

For both servo motors the chirp input had an amplitude equal to the full-scale deflection of the servo motor, $\pm 0.5\,\mathrm{rad}$, and increased in frequency from $0.001\,\mathrm{Hz}$ to $10\,\mathrm{Hz}$ over a period of $60\,\mathrm{seconds}$. The output

was measured using the corresponding encoder, and was recorded at a sample rate of 100 Hz.

4.5.5.1 Trailing-edge servo motor

Using the compact state-space notation, the second order state space model that was fit to the data from the trailing-edge servo motor test is:

$$
\mathbf{G}_{\beta_{\text{servo, fit}}} = \left[
\begin{array}{cc|c}
-41.82 & -766.08 & 766.08 \\
1 & 0 & 0 \\
\hline
0 & 1 & 0
\end{array}
\right].
\tag{4.91}
$$

The transfer function was also estimated from the chirp data, and is defined as:

$$
T_{uy}(j\omega) = \frac{P_{yu}(j\omega)}{P_{uu}(j\omega)},
\tag{4.92}
$$

where:

P_{yu} is the cross power spectral density of the input (u) and the output (y), and

P_{uu} is the power spectral density of u.

The coherence function, γ, is a measure of the coherence between the input and output, and hence re ects the quality of the transfer function estimate. It is defined as:

$$
\gamma^2(j\omega) = \frac{P_{yu}^2(j\omega)}{P_{uu}(j\omega)P_{yy}(j\omega)},
\tag{4.93}
$$

where:

P_{yy} is the power spectral density of y.

This transfer function estimate was calculated using a Blackman window of size 2^{11} samples, a Discrete Fourier Transform (DFT) size of 2^{11} samples, and a window overlap of 2^{10} samples. The transfer function estimate, coherence function, as well as the frequency response of the state space model are both shown in Figure 4.11.

The model has a natural frequency of $\omega_n = 27.7 \, \text{rad/s}$ and damping ratio of $\zeta = 0.755$. The stiffness and damping values for use in the dynamics, Equation (4.52), are then:

$$
k_{\beta_{\text{servo}}} = 766.08 \hat{I}_\beta, \text{ and}
\tag{4.94}
$$

$$
c_{\beta_{\text{servo}}} = 41.82 \hat{I}_\beta.
\tag{4.95}
$$

Figure 4.11: Trailing-edge servo motor parameter identification using a chirp input of amplitude equal to the full-scale deﬂection of the servo motor and frequency range from 0.001 Hz to 10 Hz over 60 s. The poor coherence at low frequencies is due to the chirp signal passing through the low frequency range quickly, but is of little concern as the servo motors controllers ensure a DC gain of 1. The loss of coherence at higher frequencies corresponds to the maximum chirp frequency, 10 Hz (approximately 62.8 rad/s).

4.5.5.2 Leading-edge servo motor

The second order state-space model that was fit to the data from the leading-edge servo motor is:

$$\mathbf{G}_{\gamma_{\text{servo, fit}}} = \left[\begin{array}{cc|c} -44.27 & -530.24 & 530.24 \\ 1 & 0 & 0 \\ \hline 0 & 1 & 0 \end{array} \right]. \tag{4.96}$$

The transfer function estimate, as defined above in Equation (4.92) and calculated using the same parameters, for the leading-edge servo, along with the coherence function and frequency response of the state space model are shown in Figure 4.12.

The natural frequency of the leading-edge servo motor is $\omega_n = 23.03\,\text{rad/s}$, which is less than that for the trailing-edge servo motor above. The damping ratio is $\zeta = 0.961$, which is higher than that for the trailing-edge servo motor. The reason for the reduced natural frequency and increased damping of the leading-edge servo motor compared with the trailing-edge servo motor is due to the larger inertia and friction of the leading-edge control surface compared to the trailing-edge control surface.

This gives stiffness and damping values for use in dynamics of:

$$k_{\gamma_{\text{servo}}} = 530.24\hat{I}_\gamma, \text{ and} \tag{4.97}$$

$$c_{\gamma_{\text{servo}}} = 44.27\hat{I}_\gamma. \tag{4.98}$$

4.5.6 System identification

Several parameters were not measured due to either difficulties in measuring them or time constraints. Instead their estimates were refined using a nonlinear grey-box system identification, as part of the System Identification toolbox in Matlab. Due to the highly nonlinear nature of the dynamics during the limit-cycle oscillations, it was impossible to use a more traditional system-identification method.

The nonlinear grey-box system identification process attempts to refine parameter estimates for a model of known structure but parameter uncertainties. It requires experimental data as an input, a model for simulating parameter changes, and a set of parameters with reasonable initial estimates for it to refine.
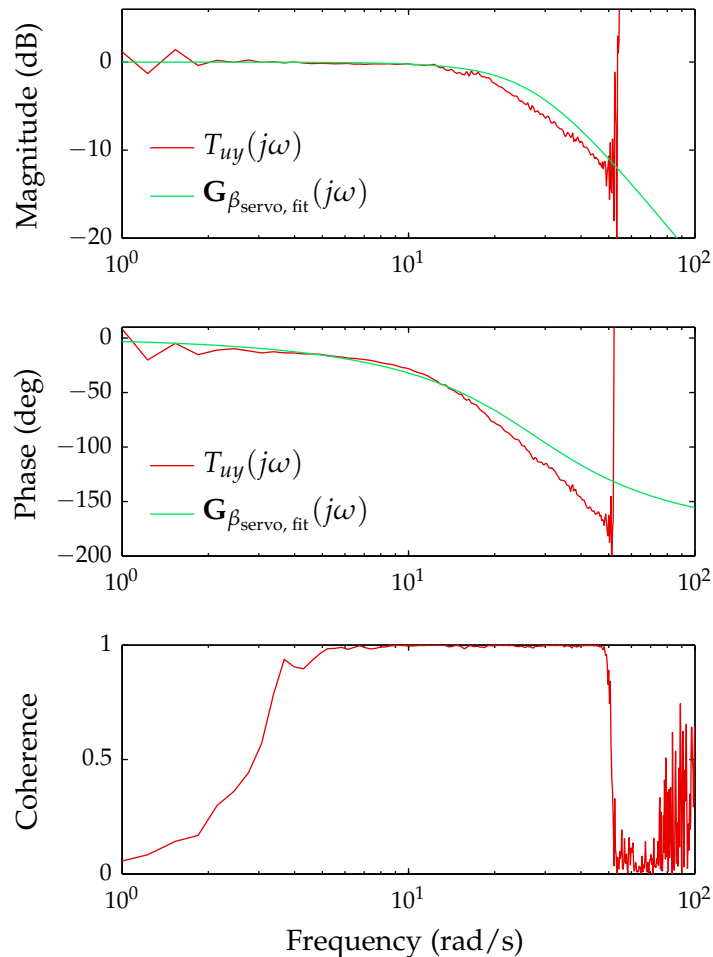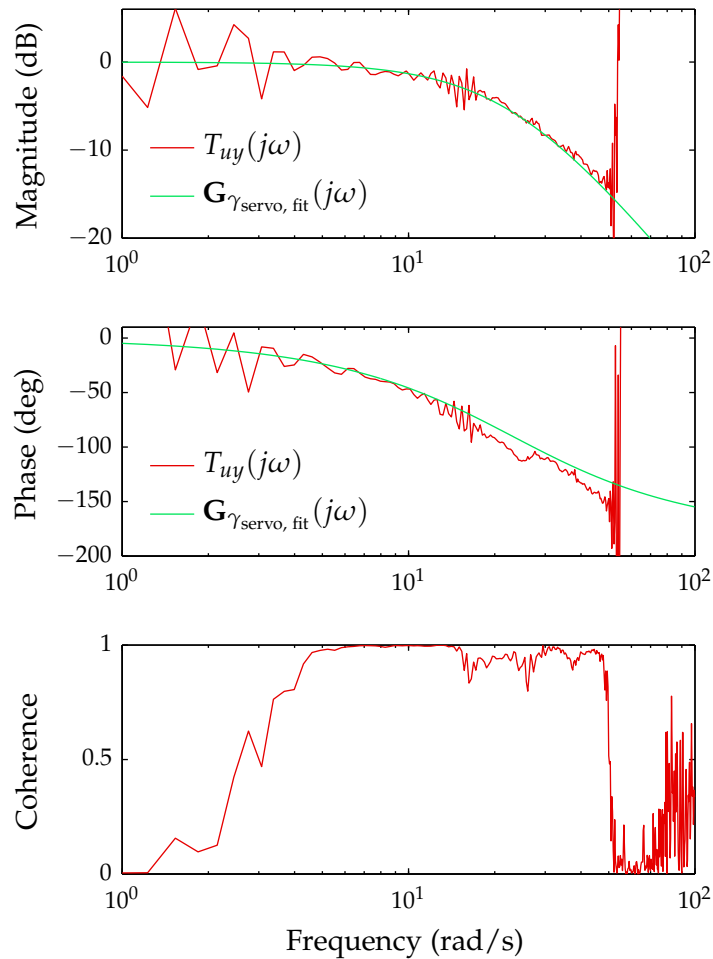
Figure 4.12: Leading-edge servo motor parameter identification using a chirp input of amplitude equal to the full-scale deflection of the servo motor and frequency range from 0.001 Hz to 10 Hz over 60 s. The poor coherence at low frequencies is due to the chirp signal passing through the low frequency range quickly, but is of little concern as the servo motors controllers ensure a DC gain of 1. The loss of coherence at higher frequencies corresponds to the maximum chirp frequency, 10 Hz (approximately 62.8 rad/s).

The uncontrolled, and hence oscillating (refer to Section 4.6 for more details about the limit-cycle oscillations), response of the aerofoil at different airspeeds with step control surface inputs was recorded for use as the input data.

The linearised three and four degree-of-freedom dynamic models, Equations (4.52) and (4.85), which still contained the torsional stiffness nonlinearity were initially coded into a Matlab m-file, however this was too slow to be useful. The models were then coded into a c-mex file and compiled which resulted in an approximate two orders of magnitude speed improvement during the system identification process.

The c-mex file and Matlab script to perform the system identification and an example dataset can be found on the additional materials CD, or as an attachment to the PDF version of this document.

The initial and final parameter estimates from this identification process are given in Table 4.3. These initial estimates were taken from the weight calculations in Section 4.5.1, previously published data in Platanitis and Strganac (2004), or selected to be close to their expected values.

Notice that the wing mass, m_α, appears twice in Table 4.3, once each for the three and four degree-of-freedom models, with the difference being that for the three degree-of-freedom case, the leading-edge surface

Table 4.3: Parameters estimated with initial and final estimates from the Nonlinear Grey-Box System Identification process. The values for m_γ, $\hat{I}_\beta$ and $\hat{I}_\gamma$ remained at the lower limits specified for the system identification process.

Parameter	Initial estimate	Final estimate
m_h	6.36 kg	6.815 kg
m_α (3 DOF)	6.97 kg	6.285 kg
m_α (4 DOF)	6.47 kg	5.715 kg
m_β	0.500 kg	0.537 kg
m_γ	0.500 kg	0.500 kg
$\hat{I}_\alpha$	0.113 kg·m^2	0.119 kg·m^2
$\hat{I}_\beta$	1.00×10^{-5} kg·m^2	1.00×10^{-5} kg·m^2
$\hat{I}_\gamma$	1.00×10^{-5} kg·m^2	1.00×10^{-5} kg·m^2
c_α	0.036 Nm·s/rad	0.205 Nm·s/rad

mass is added to the wing mass, as they are considered to be one body. The contribution to the wing inertia from the leading-edge surface in the three degree-of-freedom case is negligible, and is therefore left as one value for both cases.

Example outputs from the three degree-of-freedom model using the final parameters estimated alongside actual measured limit-cycle oscillations are given in Figures 4.13 and 4.14. The examples are performed at different airspeeds to demonstrate the accuracy of the nonlinear model s dependence on airspeed. The pitch and plunge from the model match well with those of the experimental results in both amplitude and frequency. The trailing-edge surface position shows a moderate amplitude error, which is largely due to the servo motor dynamics measured using full-scale inputs, which corresponds to a worst-case bandwidth for the servo motors. At low de ections, the servo motor has a higher bandwidth, and hence a reduced tracking error.

Example outputs from the four degree-of-freedom using the final estimated parameters alongside limit-cycle oscillation data are given in Figures 4.15 and 4.16.

In Figure 4.15, the frequency and amplitude of the dominant pitch and plunge states again agree very well. The trailing-edge surface has a similar error to that discussed for the three degree-of-freedom system above, and the leading-edge surfaces agree excellently.

In Figure 4.16 the amplitude of the dominant pitch and plunge states match well, but there is a small error in frequency of approximately 4.5 %. This frequency error also propagates through to the leading- and trailing-edge surfaces.

4.5.7 Summary

The entire set of parameters finally used for each model, after the system-identification process, are given in Table 4.4. Notice that m_α appears twice, once each for the three and four degree-of-freedom cases. This is due to the reasons discussed above in Section 4.5.6.

Figure 4.13: Example output from the nonlinear grey-box system identification for the three degree-of-freedom model at $U = 11.3\,\text{m/s}$.

Figure 4.14: Example output from the nonlinear grey-box system identification for the three degree-of-freedom model at $U = 13.1\,\text{m/s}$.
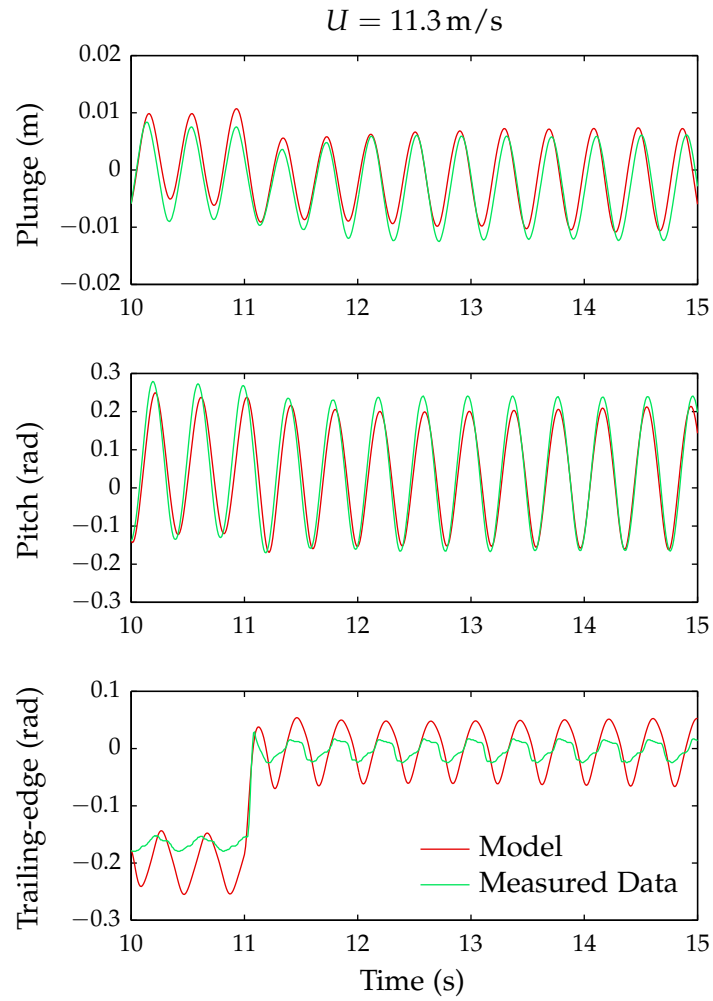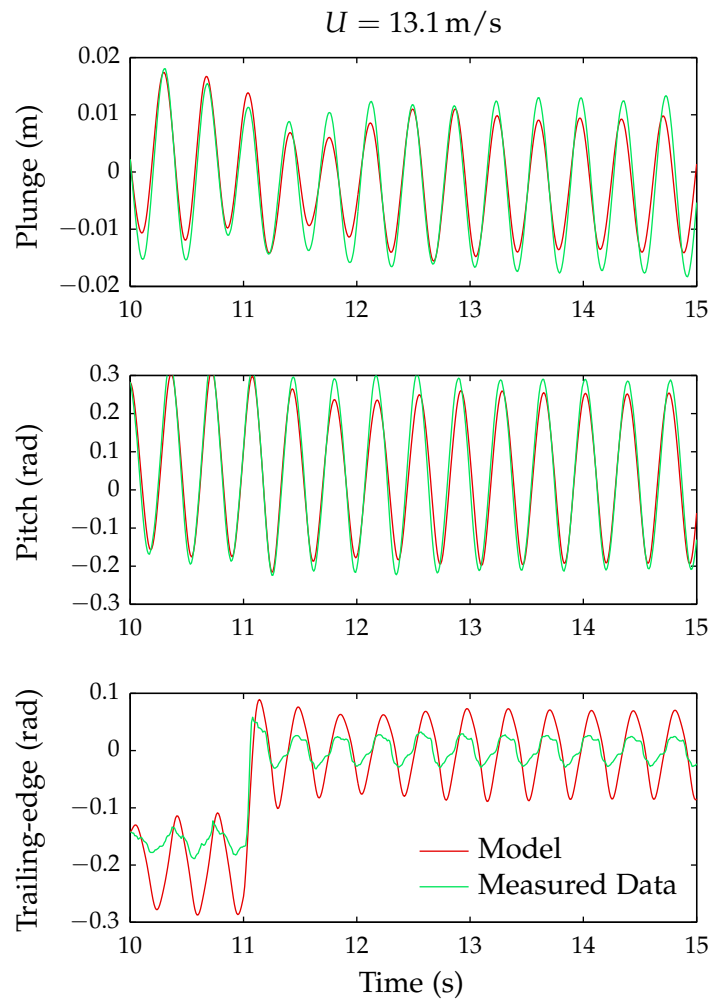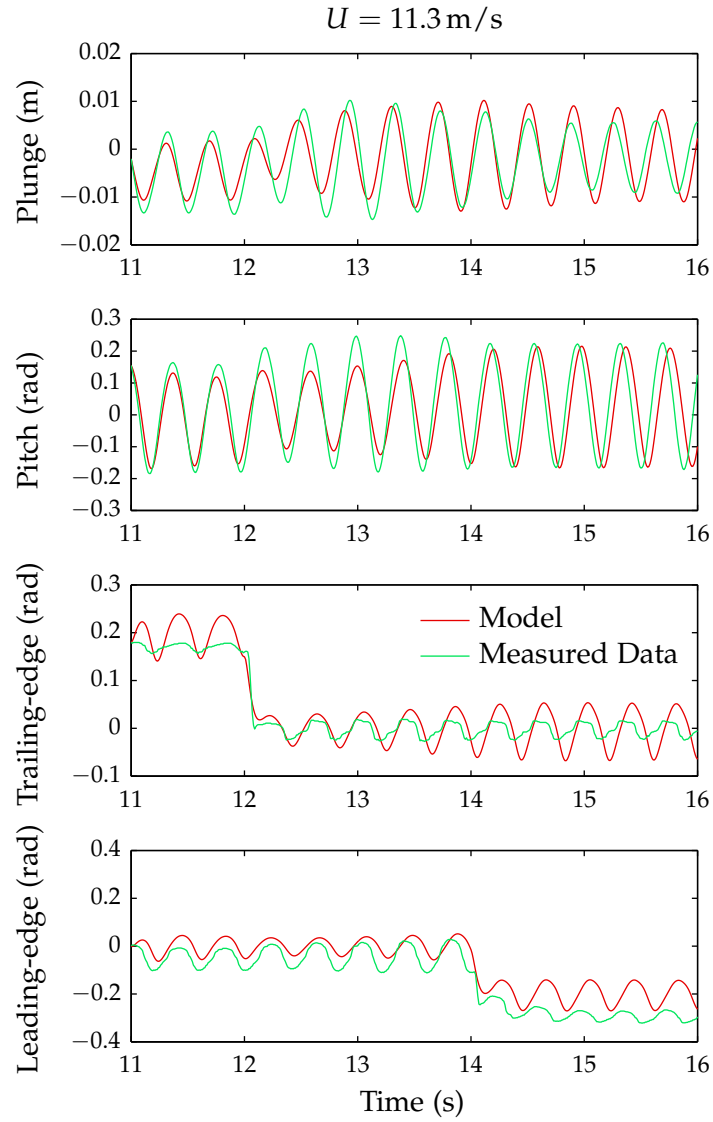
Figure 4.15: Example output from the nonlinear grey-box system identification for the four degree-of-freedom model at $U = 11.3\,\text{m/s}$.
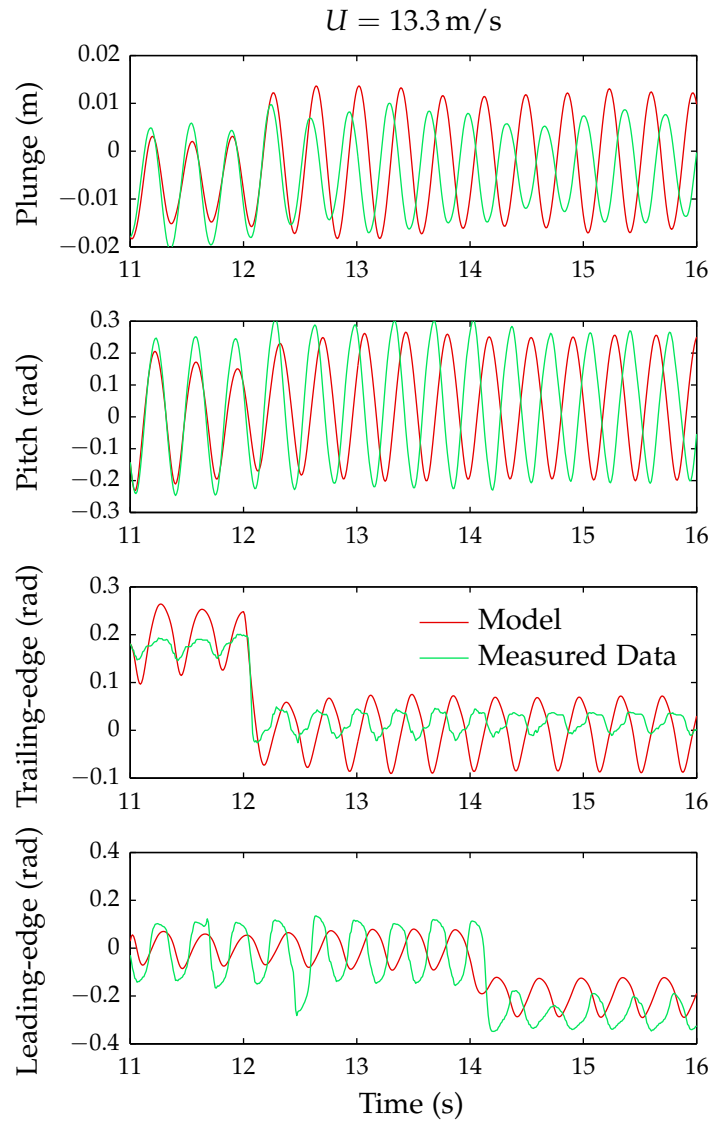
Figure 4.16: Example output from the nonlinear grey-box system identification for the four degree-of-freedom model at $U = 13.3\,\text{m/s}$.

Table 4.4: System parameters for the NATA models.

m_h	6.815 kg
m_α (3 DOF)	6.285 kg
m_α (4 DOF)	5.715 kg
m_γ	0.50 kg
m_β	0.537 kg
$\hat{I}_\alpha$	0.119 kg·m^2
$\hat{I}_\gamma$	1.00×10^{-5} kg·m^2
$\hat{I}_\beta$	1.00×10^{-5} kg·m^2
b	0.1905 m
S	0.5945 m
r_α	0.040 m
$r_{\text{a.c.}}$	0.223 m
$r_{3c/4}$	-0.033 m
r_γ	0
r_β	0
L_γ	-0.01 m
L_β	0.233 m
c_h	27.43 N·s/m
c_α	0.205 Nm·s/rad
c_{γ_servo}	4.447×10^{-4} Nm·s/rad
c_{β_servo}	4.182×10^{-4} Nm·s/rad
k_h	2844 N/m
$k_\alpha(\alpha)$	$25.55 - 103.19\alpha + 543.2\alpha^2$ Nm/rad
k_{γ_servo}	5.302×10^{-3} Nm/rad
k_{β_servo}	7.661×10^{-3} Nm/rad
C_{l_α}	6.757
$C_{m_{\alpha,\text{eff.}}}$	-1.17
C_{l_γ}	0.1566
$C_{m_{\gamma,\text{eff.}}}$	0.127
C_{l_β}	3.774
$C_{m_{\beta,\text{eff.}}}$	-2.10

4.6 Parameter dependence

This section explores the dependence of the NATA to both airspeed and torsional stiffness, which are the two significant nonlinearities in the model.

An airspeed root locus for the three degree-of-freedom system, which shows the movement of the poles with respect to airspeed at several different torsional stiffnesses, is given in Figure 4.17. The root locus is constructed through Jacobian linearisation of the pitch stiffness function at five equidistant values between $\alpha = 0$ rad and $\alpha = 0.3$ rad, and evaluating the linearised system poles at varying airspeeds. For the sake of brevity the airspeed root locus for the four degree-of-freedom model has been omitted because it does not differ significantly from the three degree-of-freedom case.

Figure 4.17 shows that the NATA is stable for low airspeeds, and as the airspeed increases it becomes unstable. The effect of the increasing torsional stiffness is to increase the speed of the unstable poles, and increase the airspeed at which the system goes unstable. The airspeeds at which the system goes unstable for the different stiffnesses, as well as the frequency of the unstable poles are given in Table 4.5.

Whilst not immediately obvious from Figure 4.17, the main effect of the nonlinear torsional stiffness is that it prevents the wing from going unstable, instead causing limit-cycle oscillations. Recall from Section 2.4.3.2 that a limit-cycle oscillation is an oscillation bound by some nonlinear effect, in this instance utter bounded by the nonlinear torsional stiffness, and they will settle into the same oscillation cycle for all reasonable initial state trajectories.

Table 4.5: Airspeed at which the NATA model goes unstable, and the frequency of the unstable poles, for different torsional stiffness values.

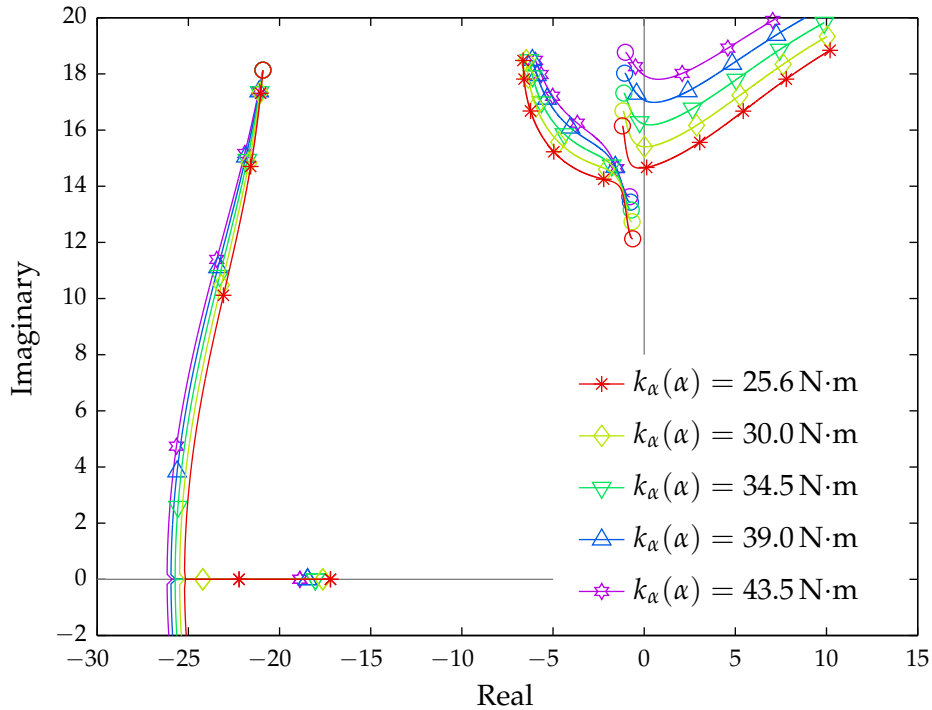| $k_\alpha(\alpha)$	U	$\omega_{unstable}$
25.6 N·m	9.7 m/s	14.7 rad/s
30.0 N·m	10.0 m/s	15.4 rad/s
34.5 N·m	10.7 m/s	16.2 rad/s
39.0 N·m	11.6 m/s	17.1 rad/s
43.5 N·m	12.6 m/s	18.0 rad/s

Figure 4.17: Airspeed root locus of the three degree-of-freedom aeroelastic system at different torsional stiffnesses. The circle marker, $\circ$, indicates the point where $U = 0 \, \text{m/s}$, and markers are placed every $10 \, \text{m/s}$ thereafter.

At low stiffnesses (around $\alpha = 0 \, \text{rad}$) the system is unstable and begins to oscillate. As the oscillations, and hence pitch angle, increase, so too does the torsional stiffness and hence torsional restoring moment, which prevents further increase in the magnitude of the oscillations. This is more clearly shown in the phase-plot for the three degree-of-freedom system shown in Figure 4.18.

This figure clearly shows the limit-cycle oscillations at airspeeds that would be unstable at $\alpha = 0 \, \text{rad}$, and that the NATA model will settle into these limit-cycle oscillations for reasonable initial state trajectories.

Figure 4.18 also shows that with increasing airspeed the amplitude of the limit-cycle oscillations also increase. At airspeeds much above those plotted the limit-cycle oscillations grow in amplitude significantly such that many of the assumptions in the model would break down.

It is clear that the torsional stiffness nonlinearity prevents the NATA from going unstable, and is hence a useful nonlinearity. The dependence
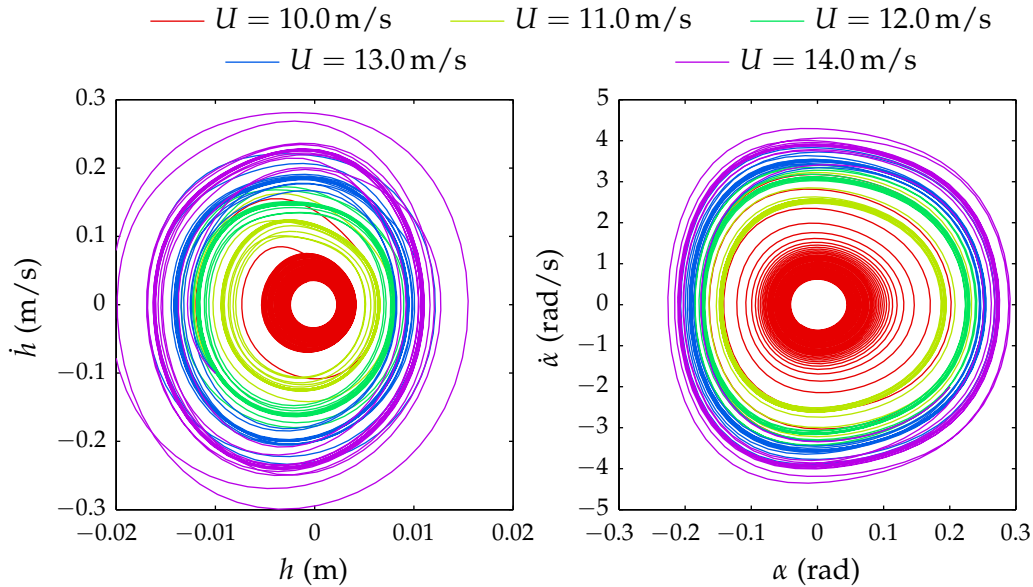
Figure 4.18: Phase plot for the three degree-of-freedom NATA model at different airspeeds. The model was simulated for 20 seconds from an initial state vector of $\mathbf{x} = \begin{bmatrix} -0.1 & -2 & 0.2 & -0.01 & 0.1 & 0 \end{bmatrix}^{\mathrm{T}}$, where $\mathbf{x} = \begin{bmatrix} h & \alpha & \beta & h & \alpha & \beta \end{bmatrix}^{\mathrm{T}}$.

of the model on airspeed is more dramatic. For all values of the torsional stiffness, increasing the airspeed pushes the unstable poles further into the right-half plane. Therefore, the primary concern for any nonlinear controller should be to stabilise the NATA at different airspeeds.

4.7   Summary

In this chapter the Nonlinear Aeroelastic Test Apparatus (NATA) has been described, along with the apparatus used during experiments. New three and four degree-of-freedom dynamic models were derived for the NATA when considering only trailing-edge, and leading- and trailing-edge control respectively. The parameters for the new dynamic models were either taken from previous studies, measured or estimated using a system-identification process. Finally it was shown that the torsional stiffness nonlinearity prevents instability, instead starting limit-cycle oscillations at low airspeeds.

5 Linear Parameter Varying Linear Quadratic Regulator Control

This chapter is based on the work published in Prime et al. (2010). A Linear Parameter Varying (LPV) state feedback controller is synthesised for the three degree-of-freedom Nonlinear Aeroelastic Test Apparatus (NATA) model based on the Linear Quadratic Regulator (LQR) framework presented as a $\mathcal{H}_2$ minimisation generalised control problem.

Using a congruence transformation, the $\mathcal{H}_2$ minimisation generalised control problem Linear Matrix Inequalities (LMIs) are rendered affine in the transformed controller and Lyapunov variables. These variables are then allowed to vary with the LPV design parameter, airspeed, and simultaneously solved at a series of grid points over the parameter space.

The controller gains are reconstructed, and a classical robustness analysis is performed on the closed-loop model.

The controller is experimentally validated, with good results, on the NATA at Texas A&M University, the results of which are presented.

Finally the results of minimising the same control problem with respect to the $\mathcal{GH}_2$ norm, instead of the $\mathcal{H}_2$ norm, are presented and contrasted with the results from the $\mathcal{H}_2$ based controller.

5.1 LPV LQR control theory

As shown in Section 2.2.5.1, the standard LQR control problem can be represented as a minimisation of the $\mathcal{H}_2$ norm from a unit white noise input, **w**, to a performance output, **z**, for the linear time-invariant state

system described by (Feron et al. 1992, and Zhou et al. 1996):

$$\mathbf{x} = \mathbf{Ax} + \mathbf{Bu} + \mathbf{w}, \tag{5.1}$$

$$\mathbf{z} = \begin{bmatrix} \mathbf{Q}^{\frac{1}{2}} & \mathbf{0} \\ \mathbf{0} & \mathbf{R}^{\frac{1}{2}} \end{bmatrix} \begin{bmatrix} \mathbf{x} \\ \mathbf{u} \end{bmatrix}, \tag{5.2}$$

where $\mathbf{Q}$ and $\mathbf{R}$ are the state and input weightings respectively.

As previously shown in Equation (2.32), this can be represented as the generalised control problem:

$$\mathbf{P}: \quad \begin{bmatrix} \mathbf{x} \\ \mathbf{z} \\ \mathbf{y} \end{bmatrix} = \left[\begin{array}{c|c|c} \mathbf{A} & \mathbf{B}_1 & \mathbf{B} \\ \hline \mathbf{C}_1 & \mathbf{D}_1 & \mathbf{E}_1 \\ \hline \mathbf{C} & \mathbf{F}_1 & \mathbf{0} \end{array} \right] \begin{bmatrix} \mathbf{x} \\ \mathbf{w} \\ \mathbf{u} \end{bmatrix} \tag{5.3}$$

with $\mathbf{B}_1 = \mathbf{I}$, $\mathbf{C}_1 = [\mathbf{Q}^{\frac{1}{2}} \ \mathbf{0}]^{\mathrm{T}}$, $\mathbf{D}_1 = [\mathbf{0} \ \mathbf{0}]^{\mathrm{T}}$, $\mathbf{E}_1 = [\mathbf{0} \ \mathbf{R}^{\frac{1}{2}}]^{\mathrm{T}}$ and $\mathbf{F}_1 = \mathbf{0}$.

5.1.1 LPV $\mathcal{H}_2$ analysis LMIs

The analysis LMIs for a $\mathcal{H}_2$ generalised control problem were previously given in Section 2.3.3. In this current section, the LPV form of the $\mathcal{H}_2$ analysis LMIs are derived.

Given a parameter vector $\mathbf{p}$, the objective is to synthesise state-feedback controller, $\mathbf{K}(\mathbf{p})$, without dynamics to minimise the $\mathcal{H}_2$ norm from $\mathbf{w}$ to $\mathbf{z}$ for the generalised control problem in Equation (5.3). State-feedback implies that the output matrix, $\mathbf{C} = \mathbf{I}$ such that the output $\mathbf{y} = \mathbf{x}$, and the control input

$$\mathbf{u} = \mathbf{K}(\mathbf{p})\mathbf{x}. \tag{5.4}$$

Applying this controller, the closed-loop form of Equation (5.3) is:

$$\mathcal{G}_{cl}(\mathbf{p}) := \left[\begin{array}{c|c} \mathcal{A}(\mathbf{p}) & \mathcal{B}_1(\mathbf{p}) \\ \hline \mathcal{C}_1(\mathbf{p}) & \mathcal{D}_1(\mathbf{p}) \end{array} \right] := \left[\begin{array}{c|c} \mathbf{A}(\mathbf{p}) + \mathbf{B}(\mathbf{p})\mathbf{K}(\mathbf{p}) & \mathbf{B}_1(\mathbf{p}) \\ \hline \mathbf{C}_1(\mathbf{p}) + \mathbf{E}_1(\mathbf{p})\mathbf{K}(\mathbf{p}) & \mathbf{D}_1(\mathbf{p}) \end{array} \right]. \tag{5.5}$$

A stochastic interpretation of the $\mathcal{H}_2$ norm that is appropriate for LPV systems, based on linear time-varying systems, is given as (Souza et al. 2003):

$$||\mathcal{G}_{cl}||_2^2 = \lim_{\tau \to \infty} \mathrm{E} \left\{ \frac{1}{\tau} \int_0^\tau \mathbf{z}^{\mathrm{T}}(t)\mathbf{z}(t) dt \right\} \tag{5.6}$$

if $\mathcal{G}_{cl}$ is exponentially stable, $\mathcal{D}_1 = \mathbf{0}$, $\mathbf{x}(0) = \mathbf{0}$ and $\mathbf{w}$ is a unit white noise process.

This norm can be calculated as (Xie 2005):

$$||\mathcal{G}_{cl}||_2^2 = \lim_{\tau \to \infty} \frac{1}{\tau} \int_0^\tau \text{Tr}[\mathcal{C}_1(\mathbf{p})\mathbf{S}_0(\mathbf{p})\mathcal{C}_1^T(\mathbf{p})]dt \qquad (5.7)$$

where $\mathbf{S}_0(\mathbf{p})$ satisfies the Lyapunov equation:

$$\mathbf{S}_0(\mathbf{p}, \mathbf{q}) = \mathcal{A}(\mathbf{p})\mathbf{S}_0(\mathbf{p}) + \mathbf{S}_0(\mathbf{p})\mathcal{A}^T(\mathbf{p}) + \mathcal{B}_1(\mathbf{p})\mathcal{B}_1^T(\mathbf{p}), \quad \mathbf{S}_0(0) = 0. \quad (5.8)$$

For any $\mathbf{S}(\mathbf{p}) > \mathbf{S}_0(\mathbf{p})$, it follows that:

$$-\mathbf{S}(\mathbf{p}, \mathbf{q}) + \mathcal{A}(\mathbf{p})\mathbf{S}(\mathbf{p}) + \mathbf{S}(\mathbf{p})\mathcal{A}^T(\mathbf{p}) + \mathcal{B}_1(\mathbf{p})\mathcal{B}_1^T(\mathbf{p}) \prec 0. \qquad (5.9)$$

Introducing the performance index ν, it is easily verified that $||\mathcal{G}_{cl}||_2 < \nu$ if and only if there exists a $\mathbf{S}(\mathbf{p}) \succ 0$ and

$$\lim_{\tau \to \infty} \frac{1}{\tau} \int_0^\tau \text{Tr}[\mathcal{C}_1(\mathbf{p})\mathbf{S}(\mathbf{p})\mathcal{C}_1^T(\mathbf{p})]dt < \nu^2. \qquad (5.10)$$

From this, the analysis LMIs are produced by firstly introducing symmetric $\mathcal{X}(\mathbf{p}) := \nu^{-1}\mathbf{S}^{-1}(\mathbf{p})$ with $\mathcal{X}(\mathbf{p}) \succ 0$, such that Equation (5.9) can be rearranged to

$$\mathcal{X}(\mathbf{p}, \mathbf{q}) + \mathcal{A}^T(\mathbf{p})\mathcal{X}(\mathbf{p}) + \mathcal{X}(\mathbf{p})\mathcal{A}(\mathbf{p}) - \mathcal{X}(\mathbf{p})\mathcal{B}_1(\mathbf{p})(-\nu^{-1}\mathbf{I})\mathcal{B}_1^T(\mathbf{p})\mathcal{X}(\mathbf{p}) \prec 0, \qquad (5.11)$$

and introducing a symmetric auxiliary parameter, $\mathcal{Z}(\mathbf{p})$, as well as $\mathcal{X}(\mathbf{p})$ to Equation (5.10), such that it can be rearranged to

$$\mathcal{Z}(\mathbf{p}) - \mathcal{C}_1(\mathbf{p})\mathcal{X}^{-1}(\mathbf{p})\mathcal{C}_1^T(\mathbf{p}) \succ 0, \text{ and } \text{Tr}(\mathcal{Z}(\mathbf{p})) < \nu. \qquad (5.12)$$

Finally taking the Schur complement of both Equations (5.11) and (5.12) yields the $\mathcal{H}_2$ analysis LMIs (Scherer et al. 1997):

$$\begin{bmatrix} \mathcal{X}(\mathbf{p}, \mathbf{q}) + \mathcal{A}^T(\mathbf{p})\mathcal{X}(\mathbf{p}) + \mathcal{X}(\mathbf{p})\mathcal{A}(\mathbf{p}) & \mathcal{X}(\mathbf{p})\mathcal{B}_1(\mathbf{p}) \\ \mathcal{B}_1^T(\mathbf{p})\mathcal{X}(\mathbf{p}) & -\nu\mathbf{I} \end{bmatrix} \prec 0,$$

$$\begin{bmatrix} \mathcal{X}(\mathbf{p}) & \mathcal{C}_1^T(\mathbf{p}) \\ \mathcal{C}_1(\mathbf{p}) & \mathcal{Z}(\mathbf{p}) \end{bmatrix} \succ 0$$

$$\text{Tr}(\mathcal{Z}(\mathbf{p})) < \nu \quad \mathcal{D}_1 = \mathbf{0}. \qquad (5.13)$$

$\mathcal{X}(\mathbf{p})$ is often known as a parameter dependent Lyapunov matrix.

5.1.2 Synthesis LPV LMIs

A general procedure for transforming analysis LMIs into controller synthesis form was previously shown in Section 2.3.4. In this section the congruence transformation for the state-feedback case is described in more detail.

The procedure involves transforming the controller parameters and the Lyapunov matrix into a new set of variables that render the LMIs affine. For the state-feedback case we introduce a transformed Lyapunov variable, $\mathbf{Y}$, and a transformed controller variable, $\mathbf{M}$, a transformation variable, $\mathcal{Y}$, and apply a congruence transformation of

$$
\mathcal{Y}, \quad \mathcal{Y} \quad \text{and} \quad \left[\begin{array}{c|c} \mathcal{Y} & \mathbf{0} \\ \hline \mathbf{0} & \mathbf{I} \end{array}\right] \tag{5.14}
$$

to

$$
\mathcal{X}, \quad \mathcal{X} \quad \text{and} \quad \left[\begin{array}{c|c} \mathcal{X}\mathcal{A} & \mathcal{X}\mathcal{B}_1 \\ \hline \mathcal{C}_1 & \mathcal{D}_1 \end{array}\right] \tag{5.15}
$$

respectively.

The solution

$$
\mathcal{Y} = \mathbf{Y}, \tag{5.16}
$$

$$
\mathcal{X} = \mathbf{Y}^{-1}, \quad \text{and} \tag{5.17}
$$

$$
\mathbf{K} = \mathbf{M}\mathbf{Y}^{-1} \tag{5.18}
$$

under the congruence transformation render the state-feedback analysis LMIs, Equation (5.13), affine with respect to the controller parameters

$$
\mathcal{Y}^{\mathrm{T}}\mathcal{X}\mathcal{Y} = \mathbf{Y}, \tag{5.19}
$$

$$
\mathcal{Y}^{\mathrm{T}}\mathcal{X}\mathcal{Y} = -\mathbf{Y}, \quad \text{and} \tag{5.20}
$$

$$
\left[\begin{array}{c|c} \mathcal{Y}^{\mathrm{T}}\mathcal{X}\mathcal{A}\mathcal{Y} & \mathcal{Y}^{\mathrm{T}}\mathcal{X}\mathcal{B}_1 \\ \hline \mathcal{C}_1\mathcal{Y} & \mathcal{D}_1 \end{array}\right] = \left[\begin{array}{c|c} \mathbf{A}\mathbf{Y} + \mathbf{B}\mathbf{M} & \mathbf{B}_1 \\ \hline \mathbf{C}_1\mathbf{Y} + \mathbf{E}_1\mathbf{M} & \mathbf{D}_1 \end{array}\right] := \left[\begin{array}{c|c} \tilde{\mathbf{A}} & \tilde{\mathbf{B}} \\ \hline \tilde{\mathbf{C}} & \tilde{\mathbf{D}} \end{array}\right]. \tag{5.21}
$$

The synthesis state-feedback LMIs are then solved for the variables $\mathbf{Y}$ and $\mathbf{M}$, and the controller and Lyapunov matrix are reconstructed using Equations (5.17) and (5.18).

Applying this transformation to the $\mathcal{H}_2$ analysis LMIs, Equation (5.13), yields the synthesis form of the $\mathcal{H}_2$ LMIs:

$$\begin{bmatrix} -\mathbf{Y}(\mathbf{p}, \mathbf{q}) + \tilde{\mathbf{A}}(\mathbf{p}) + \tilde{\mathbf{A}}^{\mathsf{T}}(\mathbf{p}) & \tilde{\mathbf{B}}(\mathbf{p}) \\ \tilde{\mathbf{B}}^{\mathsf{T}}(\mathbf{p}) & -\nu\mathbf{I} \end{bmatrix} \prec 0,$$

$$\begin{bmatrix} \mathbf{Y}(\mathbf{p}) & \tilde{\mathbf{C}}^{\mathsf{T}}(\mathbf{p}) \\ \tilde{\mathbf{C}}(\mathbf{p}) & \mathbf{Z}(\mathbf{p}) \end{bmatrix} \succ 0,$$

$$\mathrm{Tr}(\mathbf{Z}(\mathbf{p})) < \nu, \quad \text{and} \quad \tilde{\mathbf{D}} = \mathbf{0}. \tag{5.22}$$

5.2 Controller synthesis

Using the generalised control form of the LQR control problem presented in Section 5.1 above, and the controller synthesis form of the $\mathcal{H}_2$ LMIs from Section 5.1.2 above, the LPV controller for the NATA are presented below.

5.2.1 Linear parameter varying form of the NATA

The state-space matrices for the three degree-of-freedom NATA model with full-state output are were presented in Section 4.4.1, Equations (4.54), (4.56) and (4.58). Written in the compact state-space notation, this state-space model is:

$$\mathbf{G}(U, \alpha) = \left[\begin{array}{c|c} \mathbf{A}(U, \alpha) & \mathbf{B} \\ \hline \mathbf{C} & \mathbf{D} \end{array} \right], \tag{5.23}$$

where the parameter dependence is structured as:

$$\mathbf{A}(U, \alpha) = \mathbf{A}_{p0} + \mathbf{A}_{p1}U + \mathbf{A}_{p2}U^2 + \mathbf{A}_{p3}k_\alpha(\alpha). \tag{5.24}$$

It was argued in Section 4.6 that the torsional stiffness is a useful nonlinearity, and that it was more important to focus on controlling the NATA across a range of airspeeds. Hence for the remainder of this chapter the torsional stiffness will be linearised about $\alpha = 0$ rad such that the LPV form of the system can be written as:

$$\mathbf{A}(U) = \underbrace{(\mathbf{A}_{p0} + \mathbf{A}_{p3}k_\alpha(0))}_{\mathbf{A}_{p\hat{0}}} + \mathbf{A}_{p1}U + \mathbf{A}_{p2}U^2. \tag{5.25}$$

Using the dynamic model given in Section 4.4.1, and the parameters given previously in Table 4.4, the LPV state and input matrices can be calculated. The numerical values of these matrices can be found on the additional materials CD, or as an attachment to the PDF version of this document.

For full-state feedback the output and feed-forward matrices are $\mathbf{C} = \mathbf{I}$ and $\mathbf{D} = \mathbf{0}$ respectively.

5.2.2 Parameter space gridding

During controller synthesis, the parameters U and U^2 can be treated in two ways. The first is to treat U and U^2 as independent, which only requires solving the LMIs at the vertices of the parameter space, but this approach is overly conservative as it ignores the relationship between the two parameters.

The alternative approach is to create a grid over the true parameter space of U versus U^2 (a quadratic curve), then solve the LMIs at each of the grid points. This approach greatly reduces conservatism, however it also increases the computational cost and destroys true convexity, so that performance claims are no longer valid. To ensure adequate controller performance the controller gains generated from this grid must be verified on a finer grid and shown to achieve the performance specification. Should verification fail, the controller synthesis step should be repeated using a finer grid.

In this work, the gridding approach was used. Triangular grid elements were constructed over the curve of U versus U^2 such that the curve always lay within the grid element. The triangular elements are constructed from two points on the curve, and a third point at the intersection of the curve tangent from the first two points, as shown in Figure 5.1.

For $x = U$, $f(x) = x^2$ and with two points, x_1 and x_2, on the $y = f(x)$ curve, the intersection of the tangents point is

$$x_c = \frac{f'(x_1)x_1 - f'(x_2)x_2 - f(x_1) - f(x_2)}{f'(x_1) - f'(x_2)}. \tag{5.26}$$

The equation of the line directly between the two points x_1 and x_2 is then

$$f_{1,2}(x) = \left(\frac{f(x_2) - f(x_1)}{x_2 - x_1} \right) (x - x_1) + f(x_1), \tag{5.27}$$
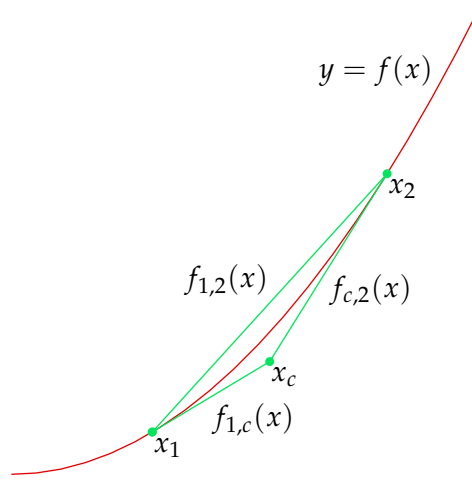
Figure 5.1: Triangular grid element as formed over the U versus U^2 parameter space.

and the equations of the two lines to x_c are

$$f_{1,c}(x) = f'(x_1)(x - x_1) + f(x_1) \text{ for } x_1 \leq x \leq x_c, \text{ and} \qquad (5.28)$$
$$f_{c,2}(x) = f'(x_2)(x - x_2) + f(x_2) \text{ for } x_c \leq x \leq x_2. \qquad (5.29)$$

5.2.3 Controller Synthesis

The parameter dependent transformed controller variables take the same form as Equation (4.55):

$$\mathbf{Y}(U) = \mathbf{Y}_{p0} + \mathbf{Y}_{p1}U + \mathbf{Y}_{p2}U^2, \qquad (5.30)$$
$$\mathbf{M}(U) = \mathbf{M}_{p0} + \mathbf{M}_{p1}U + \mathbf{M}_{p2}U^2. \qquad (5.31)$$

From which, the temporal derivative of the transformed Lyapunov matrix is easily shown to be

$$\mathbf{Y} = \mathbf{Y}_{p1}U + 2\mathbf{Y}_{p2}UU. \qquad (5.32)$$

The temporal derivative of airspeed is expected to be much slower than the dynamics of the wing, thus for this study U is assumed to be zero. Additionally, due to a limitation of the wind tunnel it was not possible to vary the airspeed in a useful way for experimentation, thus in practise $U \approx 0$.

With the aim of suppressing the limit-cycle oscillations with moderate actuator demands, and using a trial-and-error approach, the state and input LQR weightings were chosen to be:

$$\mathbf{Q} = \mathrm{diag}\left(1, 10, 1 \times 10^{-4}, 0.1, 1, 1 \times 10^{-4}\right), \text{ and} \qquad (5.33)$$

$$\mathbf{R} = 100. \qquad (5.34)$$

The synthesis LMIs were constructed in Matlab using the package YALMIP (Löfberg 2004), the LPV form of the NATA dynamics given in Section 5.2.1, and the LQR weightings above. The LMIs were constructed at a series of 50 evenly spaced points (resulting in 49 triangular regions) from $U = 8\,\mathrm{m/s}$ to $U = 40\,\mathrm{m/s}$ as described in Section 5.2.2 above, and solved using the SDPT3 (Toh et al. 1999) solver. This resulted in a $\mathcal{H}_2$ performance index of $\nu = 101.6$.

This $\mathcal{H}_2$ performance index, as well as the resulting controller gains were then successfully verified on a finer grid spanning the same range, but containing 1000 evenly spaced grid points (resulting in 999 triangular regions).

The numeric values of the $\mathbf{M}$ and $\mathbf{Y}$ matrices that make up the controller gains can be found on the additional materials CD, or as an attachment to the PDF version of this document.

The performance index, which is the upper bound on the $\mathcal{H}_2$ norm from airspeed $8\,\mathrm{m/s}$ to $40\,\mathrm{m/s}$, is plotted against the pointwise optimal value for each airspeed calculated using a standard Riccati based LQR solution in Figure 5.2. As can be seen, the upper value of the performance index is approximately equal to the maximum of the optimal value over the designed airspeed range. It is also clear that LPV performance index is quite sub-optimal over a large portion of the airspeed design range. A technique for addressing this sub-optimality is treated more thoroughly later in Chapter 6.

When the controller is reconstructed as $\mathbf{K}(U) = \mathbf{M}(U)\mathbf{Y}^{-1}(U)$ the controller gain $\mathbf{K}(U)$ is a high-order rational function of airspeed. This can be symbolically calculated off-line, but the high order of the rational function as well as the poor numerical conditioning of the function parameters render this impractical. Instead $\mathbf{K}(U)$ is numerically calculated on-line at each time step from $\mathbf{M}(U)$ and $\mathbf{Y}(U)$.
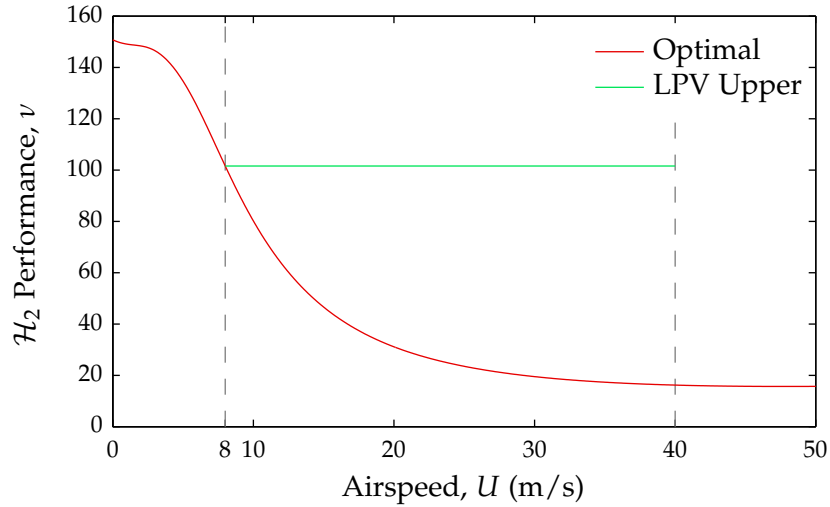
Figure 5.2: Pointwise optimal $\mathcal{H}_2$ performance at each airspeed versus the $\mathcal{H}_2$ performance achieved using the LPV LQR controller.

5.3 Results

Nyquist diagrams for the $\mathbf{K}(U)\mathbf{G}(U)$ loop at different airspeeds are shown in Figure 5.3. The Nyquist diagrams are used to illustrate how the gain and phase margins of the controlled system vary with airspeed. The extreme values of the classical robustness measures; gain margin, gain reduction margin, phase margin and sensitivity over the design airspeed range are shown in Table 5.1.

It is well known that static LQR controllers have an infinite gain margin, at least 60° phase margin and a maximum gain reduction margin of $-6.02\,\text{dB}$ (Kalman 1964, Safonov and Athans 1977, and Skogestad and

Table 5.1: Minimum robustness measures for the $\mathbf{K}(U)\mathbf{G}(U)$ loop, and the airspeeds at which these minima occur. These were calculated using the LPV model of the NATA from Section 5.2.1, not experimental data.

		Airspeed
Minimum gain margin	8.91 dB	39.1 m/s
Minimum gain reduction margin	-7.54 dB	21.1 m/s
Minimum phase margin	52.6°	29.9 m/s
Maximum sensitivity	1.56	39.1 m/s

(a) $U = 8.0 \, \text{m/s}$

(b) $U = 21.1 \, \text{m/s}$

(c) $U = 29.9 \, \text{m/s}$

(d) $U = 39.1 \, \text{m/s}$
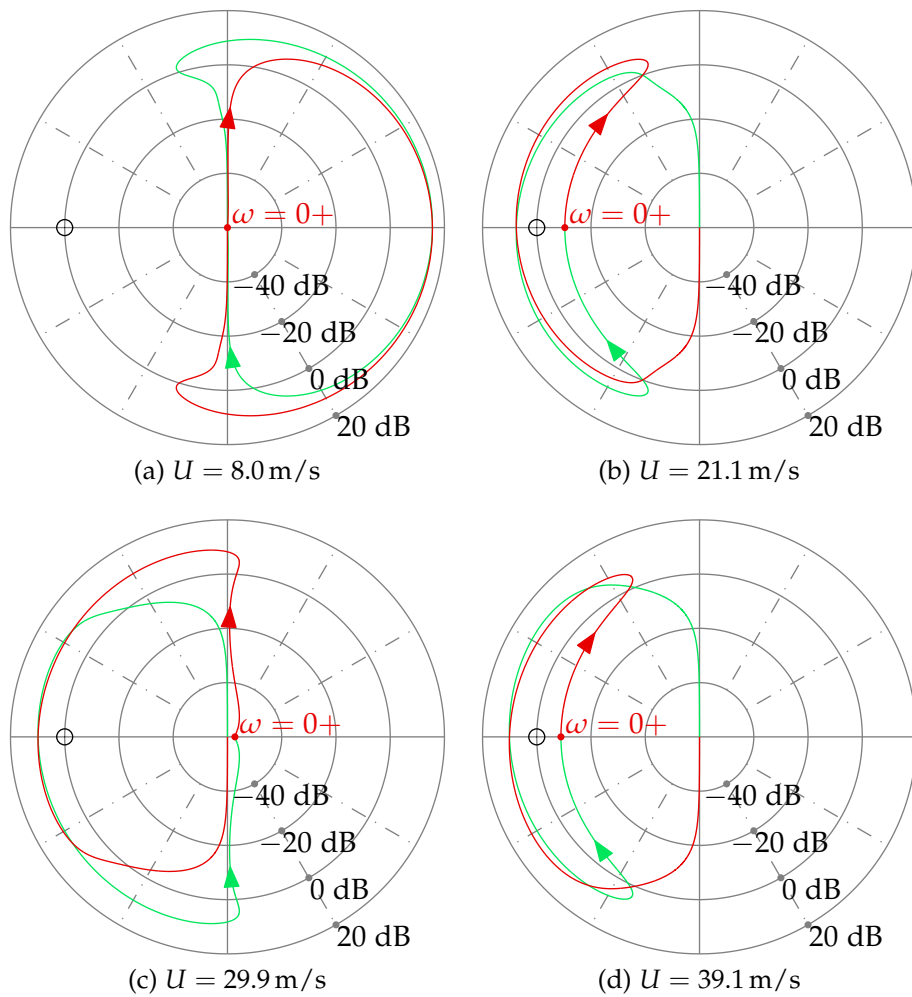
Figure 5.3: Logarithmically plotted Nyquist diagrams for the $\mathbf{K}(U)\mathbf{G}(U)$ loop at different airspeeds. The red line is $\omega > 0$, and the green line is $\omega < 0$. At $U = 8 \, \text{m/s}$ the open-loop system is stable, and goes unstable above $U = 9.6 \, \text{m/s}$. These were calculated using the LPV model of the NATA from Section 5.2.1, not experimental data.

Postlethwaite 2005). Whilst these values are not achieved at all airspeeds using the LPV LQR controller, the gain and phase margins are acceptable for all airspeeds. The reason this LPV LQR controller does not meet the gain and phase margins of a LQR controller is due to sub-optimal $\mathcal{H}_2$ performance value, as shown above in Section 5.2.3.

The synthesised controller was tested on the NATA, using the hardware and software described in Chapter 4. Though the controller was designed over the airspeed range $U \in [8\ 40]\,\text{m/s}$, experiments were only performed up to $U = 15\,\text{m/s}$ to prevent possible damage to the hardware.

In the first series of tests, the controller was disabled and limit-cycle oscillations were allowed to develop at different airspeeds, after which the controller was enabled. The results from the test at several airspeeds are shown in Figures 5.4, 5.5 and 5.6.

As can be seen, once the controller is enabled at $t = 5\,\text{s}$ the limit-cycle oscillations are suppressed and the systems settles after approximately one second without saturating the servo-motor attached to the trailing-edge control surface, which occurs at approximately $\beta = \pm 0.52\,\text{rad}$. Previous experimental attempts, such as in Platanitis and Strganac (2004), used an adaptive nonlinear controller which took longer to suppress the limit-cycle oscillations, while heavily saturating the control surfaces.

A perturbation test was also performed on the controlled system, which involved perturbing the wing in plunge by approximately $h = 0.03\,\text{m}$, and then releasing it. The results at several airspeeds are shown in Figures 5.7, 5.8 and 5.9.

The controlled system efficiently stabilises the system in approximately $t = 2.0\,\text{s}$ to $t = 2.5\,\text{s}$ at airspeeds that would cause limit-cycle oscillations if left uncontrolled. Again the controller does not saturate the servo-motor attached to the trailing-edge control surface.

Figure 5.4: Experimental results for the $\mathcal{H}_2$ LPV LQR controller at $U = 10.2\,\mathrm{m/s}$ when performing a limit-cycle oscillation test. The limit-cycle oscillations are allowed to develop with the controller turned off, then at time $t = 5\,\mathrm{s}$ the controller is enabled. Notice that during the limit-cycle oscillations β is oscillating due to its inertial coupling to the wing body and actuator dynamics.

Figure 5.5: Experimental results for the $\mathcal{H}_2$ LPV LQR controller at $U = 12.2\,\mathrm{m/s}$ when performing a limit-cycle oscillation test. The limit-cycle oscillations are allowed to develop with the controller turned off, then at time $t = 5\,\mathrm{s}$ the controller is enabled. Notice that during the limit-cycle oscillations β is oscillating due to its inertial coupling to the wing body and actuator dynamics.
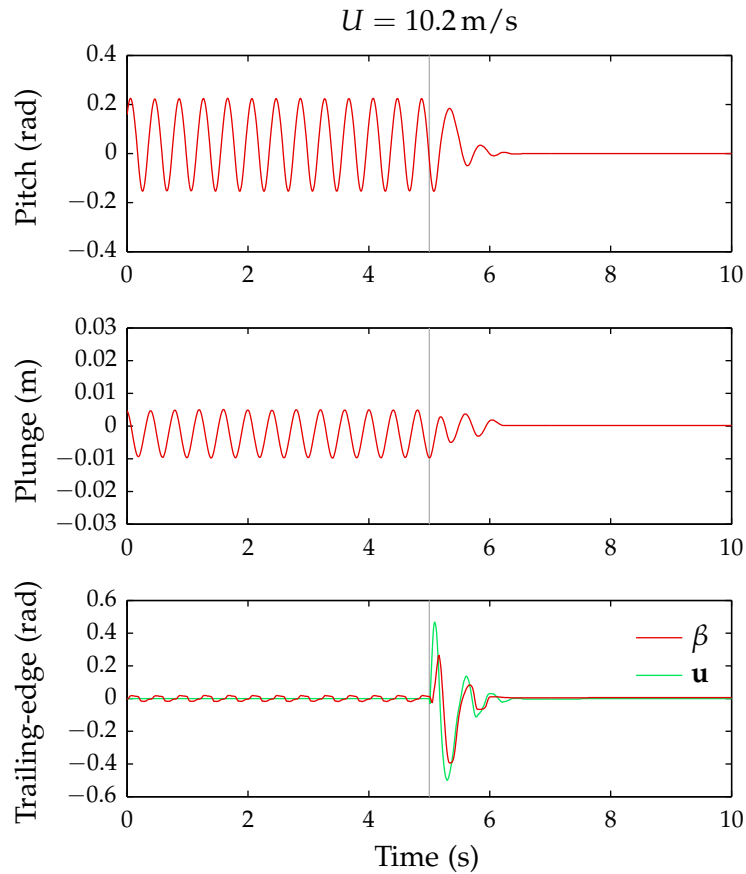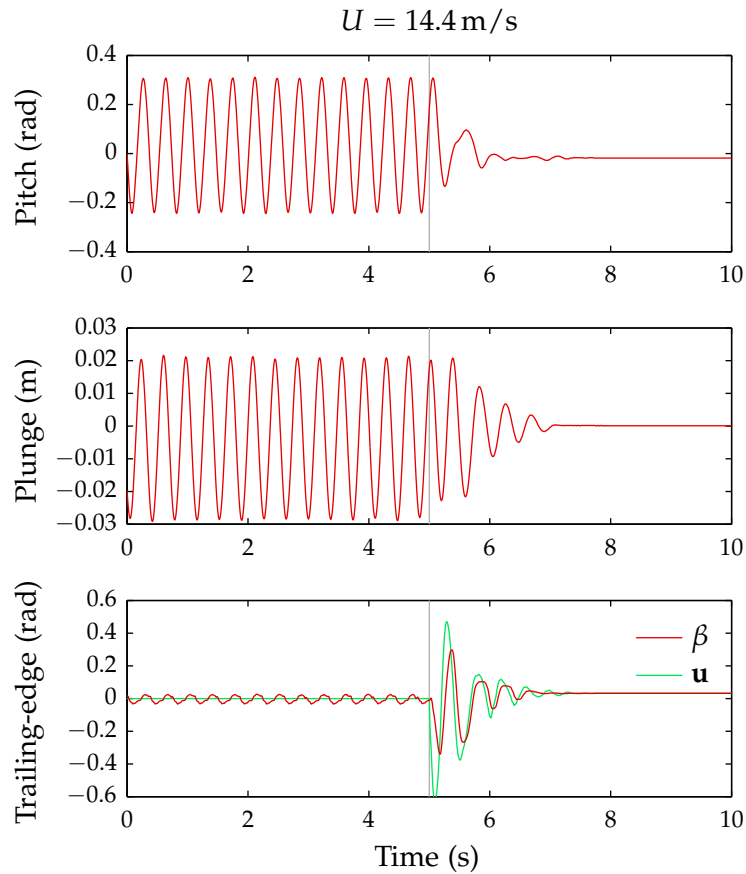
Figure 5.6: Experimental results for the $\mathcal{H}_2$ LPV LQR controller at $U = 14.4\,\text{m/s}$ when performing a limit-cycle oscillation test. The limit-cycle oscillations are allowed to develop with the controller turned off, then at time $t = 5\,\text{s}$ the controller is enabled. Notice that during the limit-cycle oscillations β is oscillating due to its inertial coupling to the wing body and actuator dynamics.
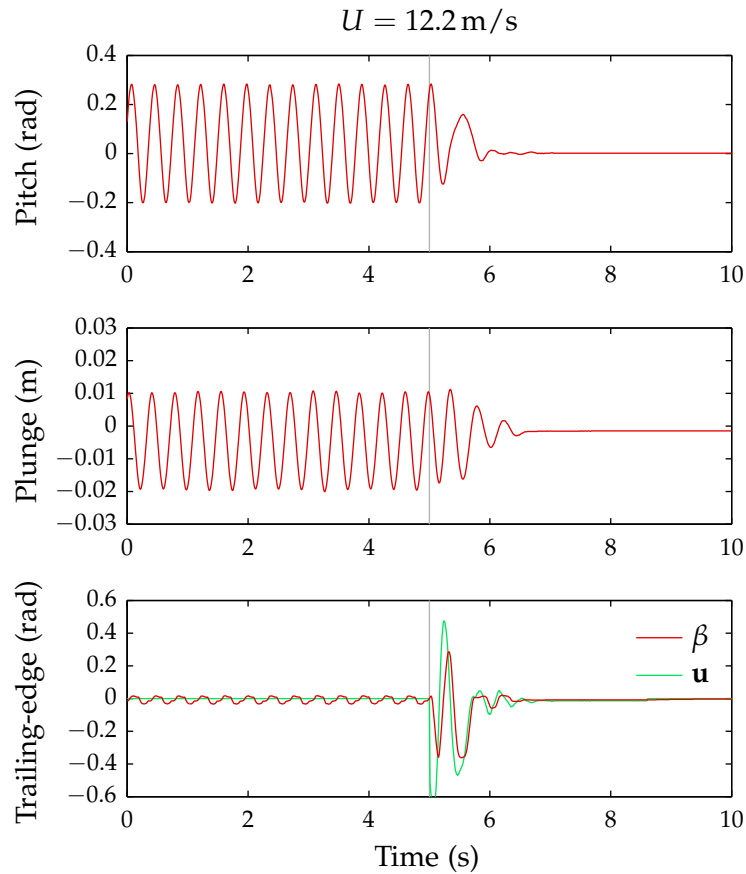
Figure 5.7: Experimental results for the $\mathcal{H}_2$ LPV LQR controller at $U = 10.2\,\text{m/s}$ when performing a perturbation test. With the controller turned on, the wing is perturbed in plunge by approximately $h = 0.03\,\text{m}$ and then released.

Figure 5.8: Experimental results for the $\mathcal{H}_2$ LPV LQR controller at $U = 12.2\,\text{m/s}$ when performing a perturbation test. With the controller turned on, the wing is perturbed in plunge by approximately $h = 0.03\,\text{m}$ and then released.
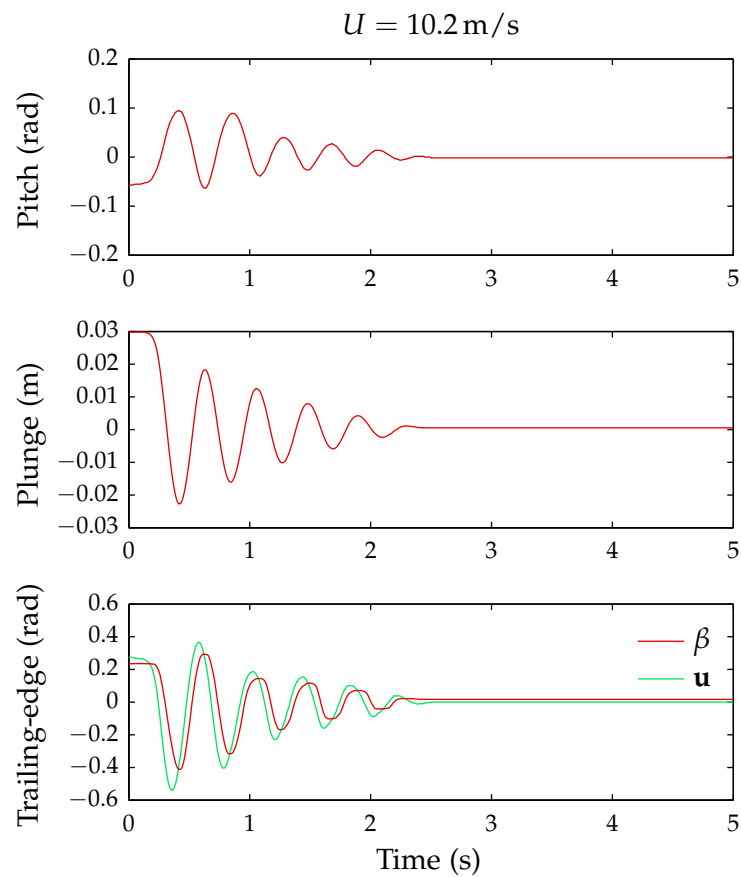
Figure 5.9: Experimental results for the $\mathcal{H}_2$ LPV LQR controller at $U = 14.5\,\text{m/s}$ when performing a perturbation test. With the controller turned on, the wing is perturbed in plunge by approximately $h = 0.03\,\text{m}$ and then released.
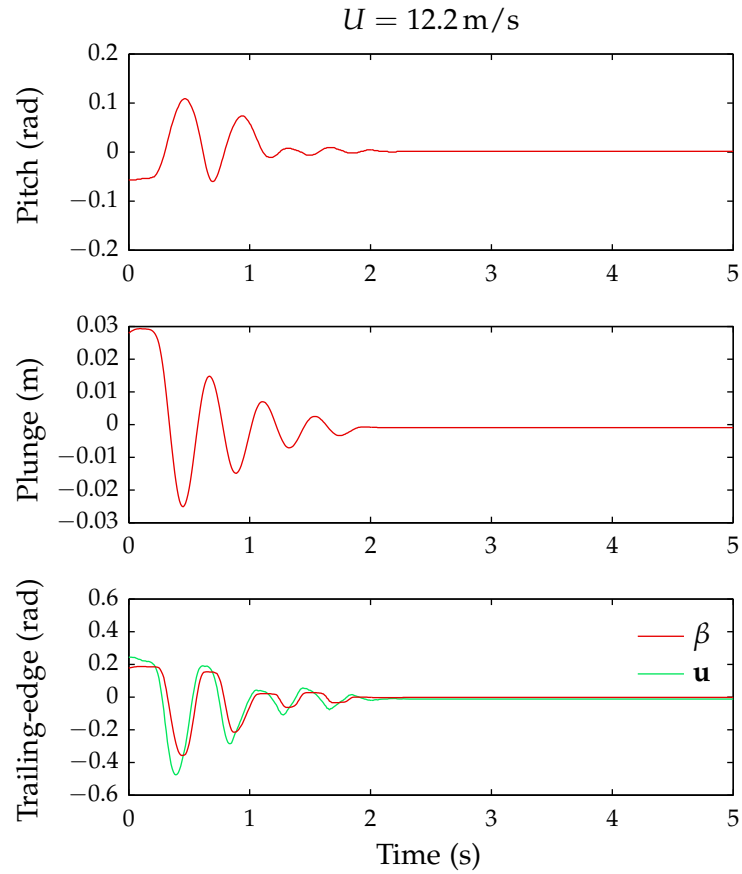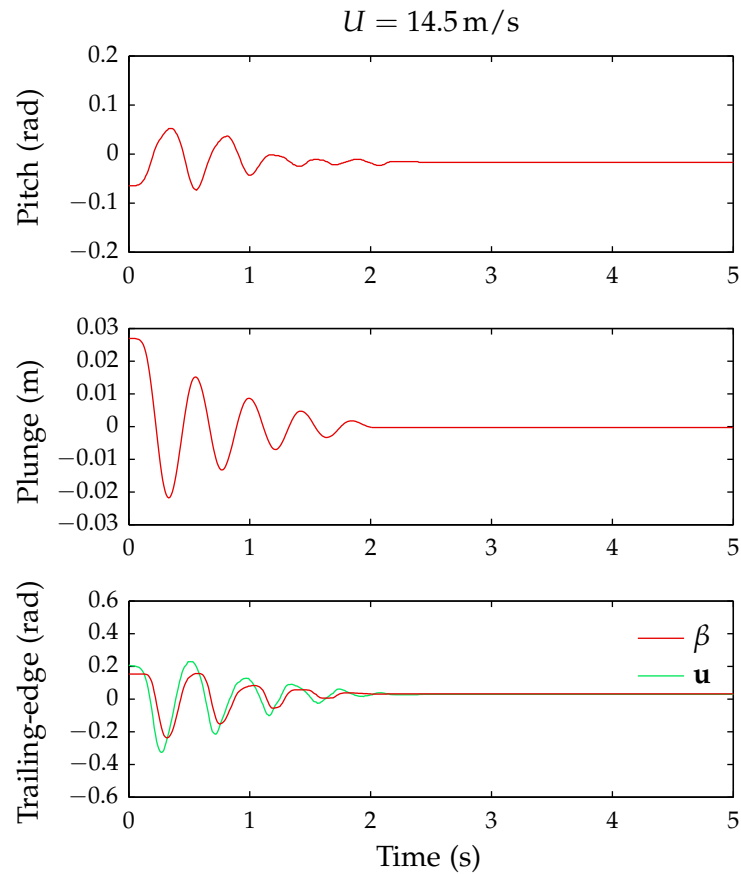
5.4 Comparison to the $\mathcal{GH}_2$ norm

It has been argued by Erwin et al. (2000) that the $\mathcal{H}_2$ norm is not an induced norm, and is inappropriate to use for certain classes of problem. They suggest it may be more appropriate to use alternatives such as the $\mathcal{L}_2$–$\mathcal{L}_\infty$ induced norm, also known as the $\mathcal{GH}_2$ norm (Wilson 1995), rather than the $\mathcal{H}_2$ norm.

Following the same process outlined for the $\mathcal{H}_2$ norm above, the synthesis $\mathcal{GH}_2$ LMIs are derived below, and the results are compared to those for the $\mathcal{H}_2$ based controller.

5.4.1 LPV $\mathcal{GH}_2$ synthesis LMIs

As previously shown in Equation (2.76), the $\mathcal{GH}_2$ norm is defined as the $\mathcal{L}_2$–$\mathcal{L}_\infty$ induced norm:

$$||\mathbf{G}||_{\mathcal{GH}_2} := \sup_{0 < ||\mathbf{w}||_2 < \infty} \frac{||\mathbf{z}||_\infty}{||\mathbf{w}||_2}, \tag{5.35}$$

which satisfies (Rotea 1993):

$$||\mathbf{G}||_{\mathcal{GH}_2}^2 = \frac{1}{2\pi} \lambda_{\max} \left(\int_{-\infty}^{\infty} \mathbf{G}(i\omega)\mathbf{G}^\dagger(i\omega) \right), \tag{5.36}$$

where $\lambda_{\max}(\cdot)$ denotes the maximum eigenvalue. At this point it is worth noting that when $\mathbf{z}$ is a scalar signal, Equation (5.36) collapses to the scalar $\mathcal{H}_2$ problem.

In a similar procedure to that presented for the $\mathcal{H}_2$ norm, a solution to the $\mathcal{GH}_2$ norm can be calculated using (Wang and Wilson 2001):

$$||\mathbf{G}||_{\mathcal{GH}_2}^2 = \lambda_{\max} \left(\mathcal{C}_1(\mathbf{p})\mathbf{S}_0(\mathbf{p})\mathcal{C}_1^\mathsf{T}(\mathbf{p}) \right) \tag{5.37}$$

where $\mathbf{S}_0(\mathbf{p})$ satisfies the Lyapunov equation:

$$\mathbf{S}_0(\mathbf{p},\mathbf{q}) = \mathcal{A}(\mathbf{p})\mathbf{S}_0(\mathbf{p}) + \mathbf{S}_0(\mathbf{p})\mathcal{A}^\mathsf{T}(\mathbf{p}) + \mathcal{B}_1(\mathbf{p})\mathcal{B}_1^\mathsf{T}(\mathbf{p}), \quad \mathbf{S}_0(0) = 0. \tag{5.38}$$

For any $\mathbf{S}(\mathbf{p}) > \mathbf{S}_0(\mathbf{p})$, it follows that:

$$- \mathbf{S}(\mathbf{p},\mathbf{q}) + \mathcal{A}(\mathbf{p})\mathbf{S}(\mathbf{p}) + \mathbf{S}(\mathbf{p})\mathcal{A}^\mathsf{T}(\mathbf{p}) + \mathcal{B}_1(\mathbf{p})\mathcal{B}_1^\mathsf{T}(\mathbf{p}) \prec 0. \tag{5.39}$$

It is then easily shown that:

$$\lambda_{\max}\left(\mathcal{C}_1(\mathbf{p})\mathbf{S}_0(\mathbf{p})\mathcal{C}_1^{\mathrm{T}}(\mathbf{p})\right) < \nu^2. \tag{5.40}$$

Notice the similarity between Equation (5.10) and Equation (5.40). It should come as no surprise that the analysis LMIs for the $\mathcal{GH}_2$ problem are very similar to those of the $\mathcal{H}_2$ problem, with the difference being the inequality for Equation (5.40) can be constructed directly using the Schur complement, without the need to introduce an auxiliary variable. Thus, by introducing the symmetric $\mathcal{X}(\mathbf{p}) := \nu^{-1}\mathbf{S}^{-1}(\mathbf{p})$, the $\mathcal{GH}_2$ analysis LMIs are:

$$\begin{bmatrix} \mathcal{X}(\mathbf{p},\mathbf{q}) + \mathcal{A}^{\mathrm{T}}(\mathbf{p})\mathcal{X}(\mathbf{p}) + \mathcal{X}(\mathbf{p})\mathcal{A}(\mathbf{p}) & \mathcal{X}(\mathbf{p})\mathcal{B}_1(\mathbf{p}) \\ \mathcal{B}_1^{\mathrm{T}}(\mathbf{p})\mathcal{X}(\mathbf{p}) & -\nu\mathbf{I} \end{bmatrix} \prec 0,$$

$$\begin{bmatrix} \mathcal{X}(\mathbf{p}) & \mathcal{C}_1^{\mathrm{T}}(\mathbf{p}) \\ \mathcal{C}_1(\mathbf{p}) & \nu\mathbf{I} \end{bmatrix} \succ 0, \quad \text{and} \quad \mathcal{D}_1 = \mathbf{0}. \tag{5.41}$$

Applying the same linearising transformation for a state feedback problem from Section 5.1.2 to the $\mathcal{GH}_2$ analysis LMIs, Equation (5.41), yields the synthesis form of the $\mathcal{GH}_2$ LMIs:

$$\begin{bmatrix} -\mathbf{Y}(\mathbf{p},\mathbf{q}) + \tilde{\mathbf{A}}(\mathbf{p}) + \tilde{\mathbf{A}}^{\mathrm{T}}(\mathbf{p}) & \tilde{\mathbf{B}}(\mathbf{p}) \\ \tilde{\mathbf{B}}^{\mathrm{T}}(\mathbf{p}) & -\nu\mathbf{I} \end{bmatrix} \prec 0,$$

$$\begin{bmatrix} \mathbf{Y}(\mathbf{p}) & \tilde{\mathbf{C}}^{\mathrm{T}}(\mathbf{p}) \\ \tilde{\mathbf{C}}(\mathbf{p}) & \nu\mathbf{I} \end{bmatrix} \succ 0, \quad \text{and} \quad \tilde{\mathbf{D}} = \mathbf{0}. \tag{5.42}$$

5.4.2 $\mathcal{GH}_2$ controller synthesis

Using the same LPV form of NATA as detailed in Section 5.2.1, the same gridding process as described in Section 5.2.2, and the same $\mathbf{Q}$, $\mathbf{R}$ and grid points from Section 5.2.3, the $\mathcal{GH}_2$ controller gains can be synthesised.

The $\mathcal{GH}_2$ LMIs were constructed in Matlab using the package YALMIP (Löfberg 2004), and solved to minimise ν using the solver SDPT3 (Toh et al. 1999). The numerical values of the resulting $\mathbf{M}$ and $\mathbf{Y}$ matrices are available on the additional materials CD, or as an attachment to the PDF version of this document.

The resulting upper bound on performance is $\nu = 77.65$, but it is important to remember that this result is not directly comparable to the performance index from the $\mathcal{H}_2$ problem.

5.4.3 Results

Nyquist diagrams for the $\mathbf{K}(U)\mathbf{G}(U)$ loop for the $\mathcal{GH}_2$ minimisation based controller are shown in Figure 5.10, and the classical measures of robustness are shown in Table 5.2. A direct comparison of the gains from the controllers synthesised using the $\mathcal{GH}_2$ and $\mathcal{H}_2$ norms is shown in Figure 5.11.

As can be seen from Table 5.2, the controller synthesised using the $\mathcal{GH}_2$ norm on the performance channel is less robust then that synthesised using the $\mathcal{H}_2$ norm. This is due to the different minimisation objectives between the two problems; Equation (5.40) for the $\mathcal{GH}_2$ problem, and Equation (5.10) for the $\mathcal{H}_2$ problem. From Figure 5.11, the biggest difference in controller gain occurs for the h state, which suggests the maximum eigenvalue occurs in this state.

A simulated limit-cycle oscillation test comparing the controllers based on $\mathcal{H}_2$ and $\mathcal{GH}_2$ minimisation is shown in Figure 5.12, and a simulated perturbation test comparison between the two controllers is shown in Figure 5.13. At the airspeed presented, $U = 13\,\text{m/s}$, which roughly corresponds to the airspeed with the maximum gain difference between controllers from Figure 5.11, it can be seen that in both tests the $\mathcal{H}_2$ controller settles the system in slightly less time than the $\mathcal{GH}_2$ based controller, however the differences are minimal.

Table 5.2: Minimum robustness measures for the $\mathbf{K}(U)\mathbf{G}(U)$ loop and the airspeeds at which they occur. The controller synthesised using the $\mathcal{GH}_2$ norm, and $\mathbf{G}$ is calculated using the model from Section 5.2.1.

		Airspeed
Minimum gain margin	7.81 dB	38.9 m/s
Minimum gain reduction margin	−7.87 dB	21.4 m/s
Minimum phase margin	49.7°	36.1 m/s
Maximum sensitivity	1.69	38.9 m/s

(a) $U = 8.0\,\text{m/s}$

(b) $U = 21.1\,\text{m/s}$

(c) $U = 29.9\,\text{m/s}$

(d) $U = 39.1\,\text{m/s}$
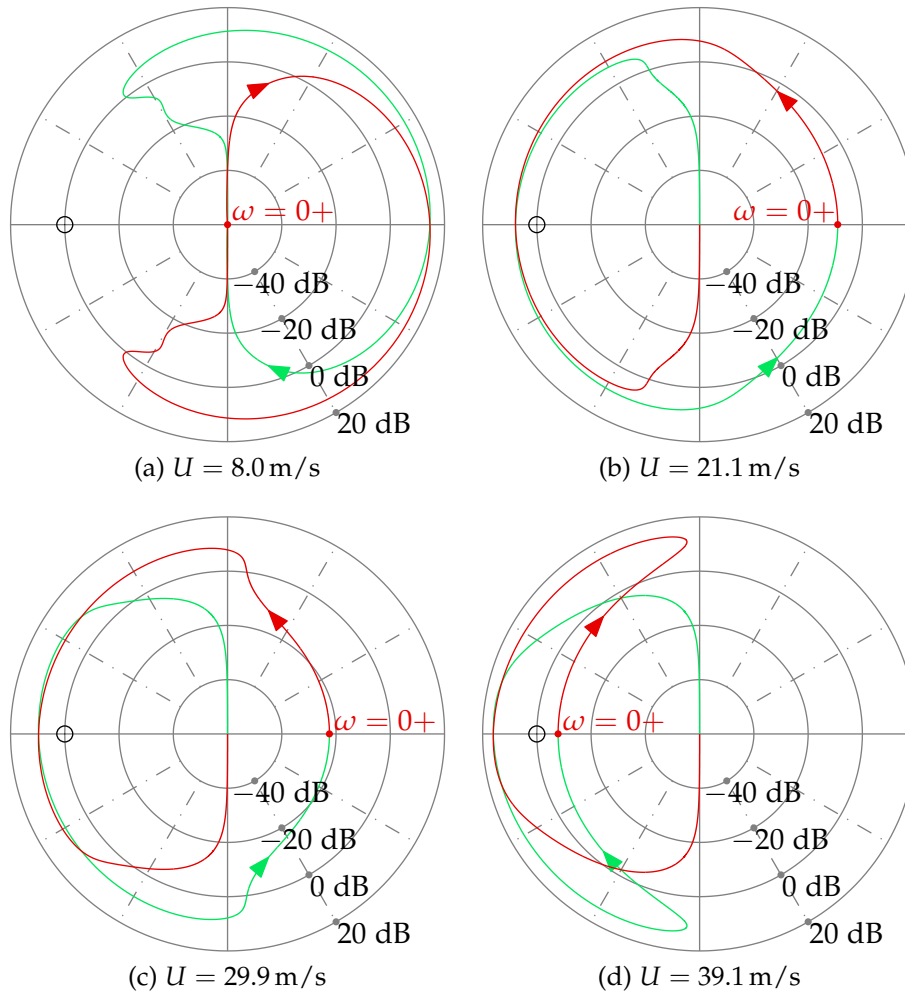
Figure 5.10: Logarithmically plotted Nyquist diagrams for the $\mathbf{K}(U)\mathbf{G}(U)$ loop, with the controller synthesised using the $\mathcal{GH}_2$ norm and $\mathbf{G}$ calculated using the model from Section 5.2.1, for different airspeeds. The red line is $\omega > 0$, and the green line is $\omega < 0$. At $U = 8\,\text{m/s}$ the open-loop system is stable, and goes unstable above $U = 9.6\,\text{m/s}$.
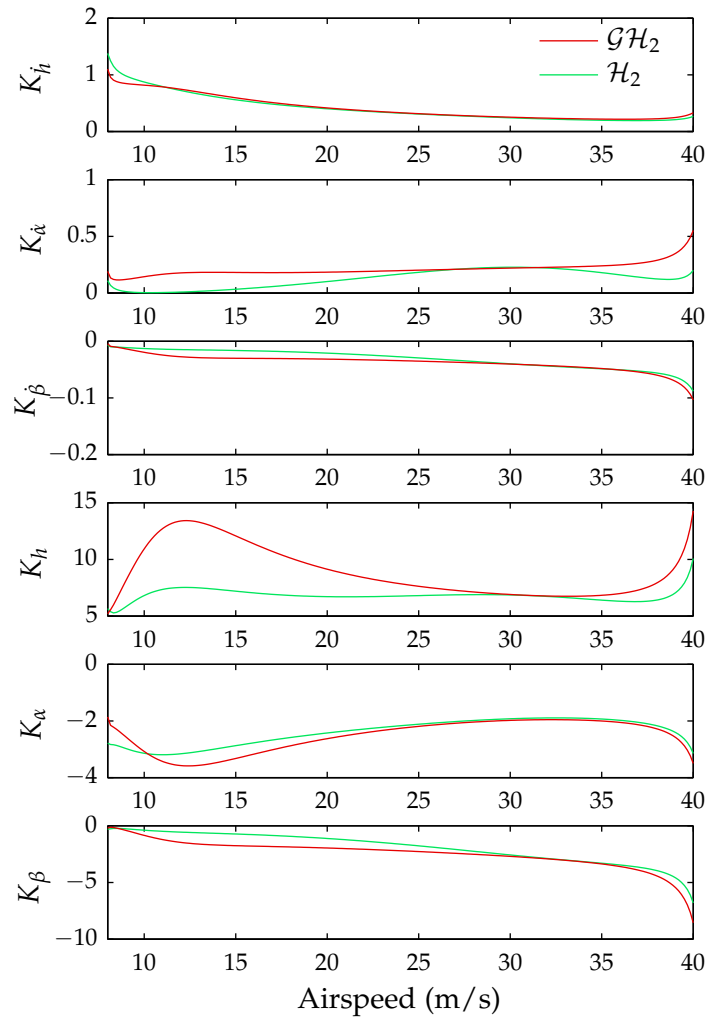
Figure 5.11: State-feedback controller gains versus airspeed for the $\mathcal{H}_2$ and $\mathcal{G}\mathcal{H}_2$ LPV LQR synthesised controllers, where the controller gains are $\mathbf{K}(U) = [K_h(U) \quad K_\alpha(U) \quad K_\beta(U) \quad K_h(U) \quad K_\alpha(U) \quad K_\beta(U)]$.
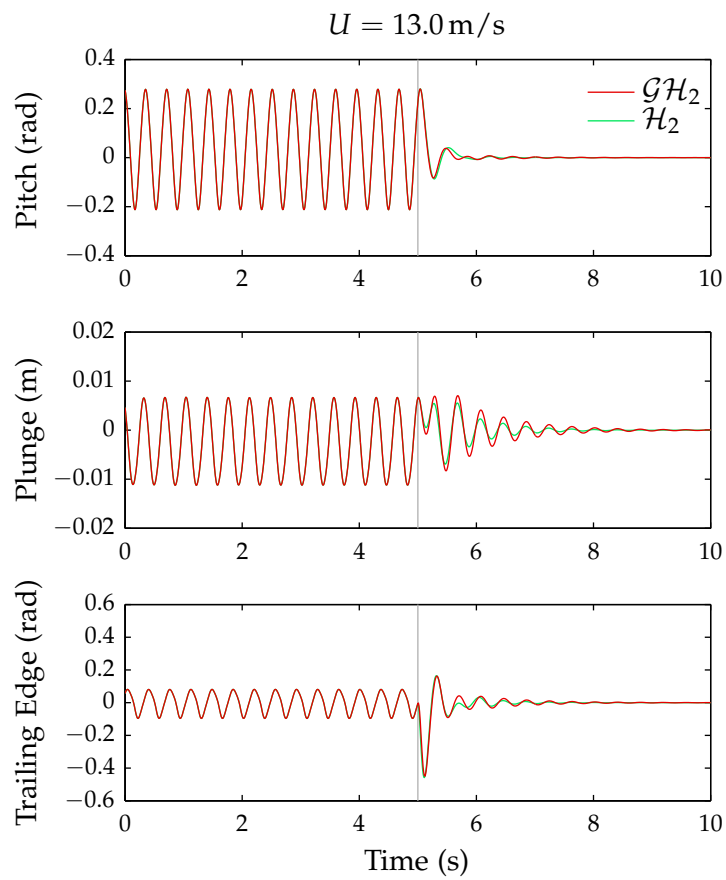
Figure 5.12: Simulated limit-cycle oscillation comparison between the $\mathcal{H}_2$ and $\mathcal{GH}_2$ based controllers.
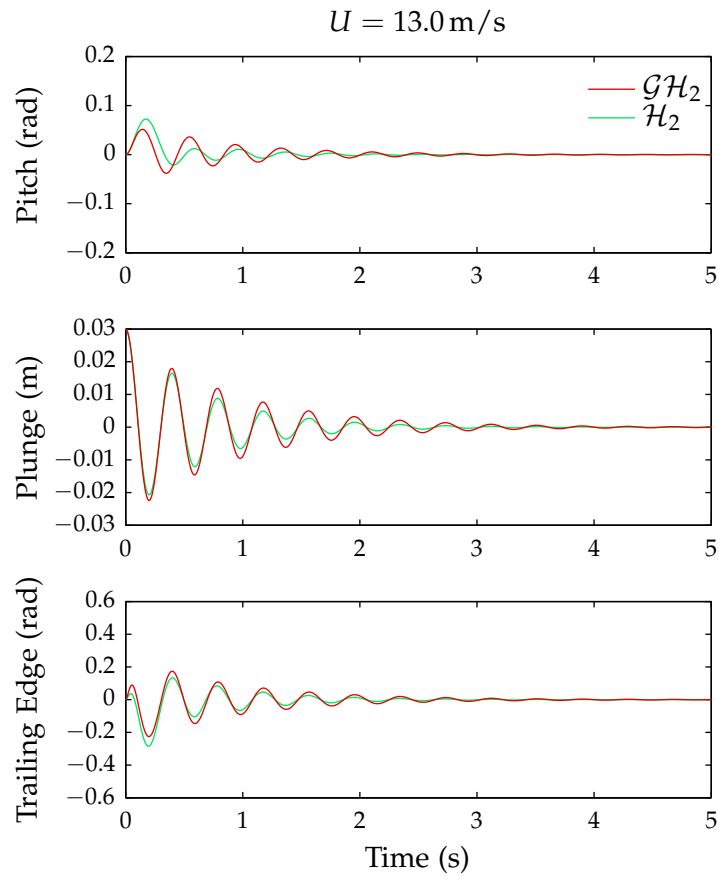
Figure 5.13: Simulated perturbation test comparison between the $\mathcal{H}_2$ and $\mathcal{GH}_2$ based controllers.

5.5 Conclusions

Using the $\mathcal{H}_2$ minimisation generalised control problem formulation of the standard LQR control problem, a LPV controller can be constructed using LMIs. The controller was experimentally shown to suppress limit-cycle oscillations and reject disturbances over a range of airspeeds when applied to the NATA.

Further to the suppression of limit-cycle oscillations and rejection of disturbances, these experimental results also show the LPV LQR controller only places moderate demands on the trailing-edge actuator unlike several previously published controllers.

The LPV LQR controller does not provide the same robustness guarantees as the standard LQR controller problem. This is due to the sub-optimal nature of the upper bound on the $\mathcal{H}_2$ norm over most of the parameter (airspeed) design range.

Although it has been argued that the $\mathcal{H}_2$ norm is not an induced norm, and hence is not appropriate for certain classes of problems (Erwin et al. 2000), it has been shown that the suggested alternative of using a $\mathcal{GH}_2$ norm results in a controller that is less robust (in the classical sense) than one synthesised using the $\mathcal{H}_2$ norm. However, the differences between controlled systems is minimal, with the $\mathcal{H}_2$ norm based controller performing slightly better.

6 Parameter Dependent Cost Functions

In this chapter, a general and simple method of reducing the performance bound of Linear Parameter Varying (LPV) controllers is described. Using the controller presented in Chapter 5 as an example, it is shown that the $\mathcal{H}_2$ norm can be reduced over much of the design airspeed using this technique.

6.1 Theory

It has been suggested by Scherer and Weiland (2004) that it is possible to allow the performance bound to vary over different optimisation points while solving control problems using LMIs. They suggest this may be useful in imposing different performance criteria over different operating conditions, but offer no solution to go about selecting the parameter dependence or optimisation criteria. Furthermore, to the author s knowledge, the results of allowing the performance index to vary with the parameter vector have not been published.

Firstly, a form with which the performance bound varies must be chosen. In the same way that the transformed controller and Lyapunov variables are given the same parameter dependence as the plant itself (refer to Section 2.3.6), the best choice for the performance bound parameter dependence is the same parameter dependence as plant. That is, let

$$\nu(\mathbf{p}) = \nu_0 + \sum_{i=1}^{m} \nu_i p_i. \tag{6.1}$$

The question is then how to minimise this parameter dependent performance bound when synthesising a controller. As the performance

index for all of the performance specifications given in Section 2.2.4 are greater or equal to zero, the simplest way of improving optimality is to set the LMI minimisation function to be the integral of the parameter dependent performance bound with respect to the parameter vector. That is, when solving the LMIs, the objective is to minimise

$$\int_\Omega \nu(\mathbf{p}) \, d\mathbf{p}. \tag{6.2}$$

where Ω is the convex hull formed by the extreme values of each parameter: $\Omega = \text{conv}\{p_1, p_2, \ldots p_n\}$. Since Equation (6.1) is affine with respect to $\mathbf{p}$, so too will the result of Equation (6.2), which allows it to be optimised using LMIs.

6.2   Example

Consider the LPV Linear Quadratic Regulator (LQR) controller from Chapter 5. Giving the performance index the same parameter dependence as the plant:

$$\nu(\mathbf{p}) = \nu_0 + \nu_1 U + \nu_2 U^2, \tag{6.3}$$

the $\mathcal{H}_2$ synthesis LMIs, originally Equation (5.22), are then:

$$\begin{bmatrix} -\mathbf{Y}(\mathbf{p}, \mathbf{q}) + \tilde{\mathbf{A}}(\mathbf{p}) + \tilde{\mathbf{A}}^{\mathsf{T}}(\mathbf{p}) & \tilde{\mathbf{B}}(\mathbf{p}) \\ \tilde{\mathbf{B}}^{\mathsf{T}}(\mathbf{p}) & -\nu(\mathbf{p})\mathbf{I} \end{bmatrix} \prec 0,$$

$$\begin{bmatrix} \mathbf{Y}(\mathbf{p}) & \tilde{\mathbf{C}}^{\mathsf{T}}(\mathbf{p}) \\ \tilde{\mathbf{C}}(\mathbf{p}) & \mathbf{Z}(\mathbf{p}) \end{bmatrix} \succ 0,$$

$$\text{Tr}(\mathbf{Z}(\mathbf{p})) < \nu(\mathbf{p}), \quad \text{and} \quad \tilde{\mathbf{D}} = \mathbf{0}, \tag{6.4}$$

with the objective of minimising

$$\int_{\underline{p_1}}^{\bar{p}_1} \int_{\underline{p_2}}^{\bar{p}_2} \nu(\mathbf{p}) \, dp_1 dp_2, \tag{6.5}$$

where in this case
    $p_1 = U$, and
    $p_2 = U^2$.

Since the parameters are clearly dependent in this case, the objective function can be improved to

$$\int_{\underline{U}}^{\bar{U}} \left(\nu_0 + \nu_1 U + \nu_2 U^2 \right) dU, \tag{6.6}$$

which will result in a lower performance bound.

Using the same numerical values, gridding process and grid points as from Section 5.2, the synthesis LMIs from Equation (6.4) were constructed in Matlab using the package YALMIP (Löfberg 2004), and solved using the SDPT3 (Toh et al. 1999) solver. The minimum upper bound on performance was found to be:

$$\nu(U) = 175.7 - 10.00U + 0.1612U^2, \tag{6.7}$$

however at this minimum performance bound the closed-loop LMIs would not verify over the finer grid due to numerical issues. Thus the parameter dependent cost function was increased and restricted to

$$\nu(U) = 175.9 - 10.00U + 0.1612U^2, \tag{6.8}$$

which passed the subsequent validation over a finer grid of 1000 points, as per Section 5.2.

The numeric values of the **M** and **Y** matrices that make up the resulting controller gains can be found on the additional materials CD, or as an attachment to the PDF version of this document. ⚑

6.2.1 Results

This performance bound, along with the several others are compared in Figure 6.1. The pointwise optimal $\mathcal{H}_2$ norms shown in the figure are calculated by assuming the plant is fixed at each airspeed and solved using a Riccati based LQR solution. The upper performance values for both the controller from this chapter, labelled as $\nu(\mathbf{p})$ Upper , and the upper performance value from Chapter 5, labelled as ν Upper , are both obtained from the LMI solutions. The actual $\mathcal{H}_2$ norm values for both controllers are calculated using $\mathrm{Tr}(\mathcal{C}_1 \mathbf{Y} \mathcal{C}_1^{\mathrm{T}})$, and are labelled $\nu(\mathbf{p})$ Actual and ν Actual for the controller from this chapter, and from Chapter 5 respectively.
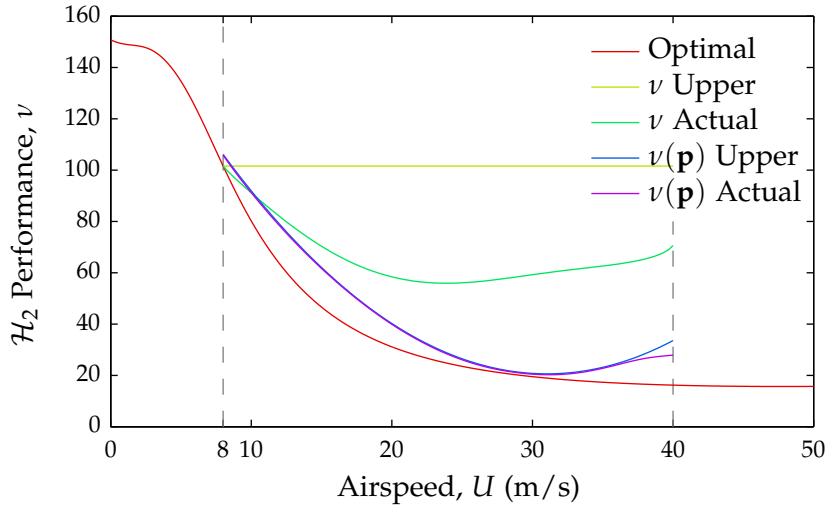
Figure 6.1: Comparison of $\mathcal{H}_2$ performance values. The LPV controller from Chapter 5 is labelled ν, while the LPV controller with parameter dependent performance value is labelled $\nu(\mathbf{p})$.

As can be seen from Figure 6.1, the $\mathcal{H}_2$ norm for the LPV LQR controller designed with the parameter dependent performance bound has increased by a small amount from approximately $U = 8\,\text{m/s}$ to $U = 11\,\text{m/s}$, but has been greatly reduced over the remaining airspeed design range. The quadratic form of the parameter dependent upper bound can also clearly be seen, and is as close to optimal as can be achieved with a quadratic function over the design range.

The minimum gain and phase margins, and the maximum sensitivity, along with the airspeeds at which they occur are shown in Table 6.1. As can be seen, compared to the controller designed in Chapter 5 (refer

Table 6.1: Minimum robustness measures for the $\mathbf{K}(U)\mathbf{G}(U)$ loop and the airspeeds at which they occur for the controller designed with a parameter dependent performance bound.

		Airspeed
Minimum gain margin	4.80 dB	25.2 m/s
Minimum gain reduction margin	−7.13 dB	40.0 m/s
Minimum phase margin	56.5°	27.1 m/s
Maximum sensitivity	2.35	25.2 m/s

to Table 5.1), the controller designed with the parameter dependent performance bound is less robust. The gain and phase margins are less than the 6 dB and 60° respectively which are generally considered desirable. Similarly the maximum sensitivity is higher than 2 which is generally considered the maximum acceptable bound.

To more clearly illustrate the reduced robustness, logarithmically plotted Nyquist diagrams are shown in Figure 6.2. It can clearly be seen that the Nyquist diagram gets quite close to the critical point in Figure 6.2c, causing the low gain margin and high sensitivity, while the minimum gain reduction margin is clearly shown in Figure 6.2d.

Once again, the LQR infinite gain margin, and at least 60° phase margin have not been met, which is due to the controller still being sub-optimal, despite being generally closer to optimal than the controller with the fixed performance bound.

6.3 Conclusions

A method of increasing the performance of a LPV control problem across the parameter range by making the performance index parameter dependent has been presented.

Using the LPV LQR controller from Chapter 5, it was shown that the performance bound was greatly reduced over most of the airspeed design range when using the parameter dependent performance bound. Though the example presented was slightly less robust than when the upper performance bound was not parameter dependent, this technique has been verified, and would be especially useful for control problems where the robustness is tied to the performance bound, such as in various types of $\mathcal{H}_\infty$ (or induced $\mathcal{L}_2$) control synthesis.

(a) $U = 8.0 \, \text{m/s}$

(b) $U = 16.0 \, \text{m/s}$

(c) $U = 25.2 \, \text{m/s}$

(d) $U = 40.0 \, \text{m/s}$
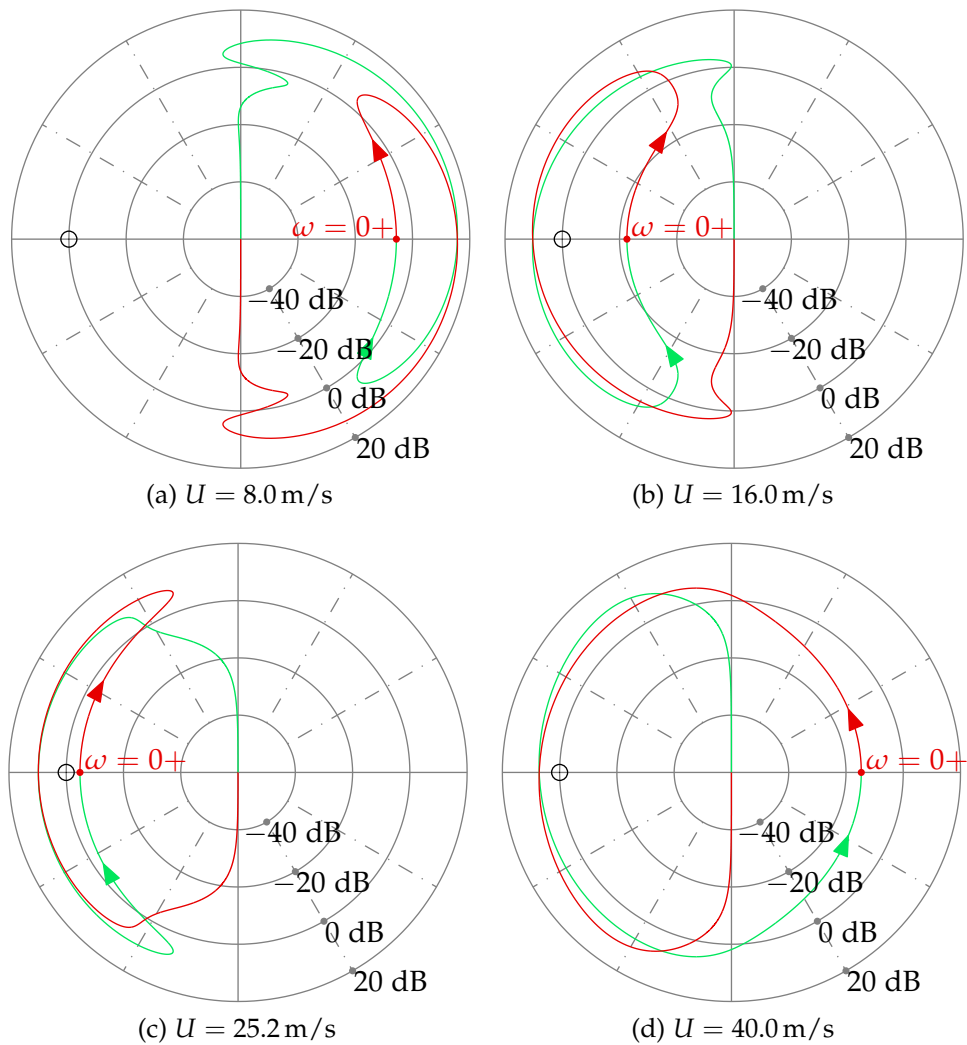
Figure 6.2: Logarithmically plotted Nyquist diagrams for the $\mathbf{K}(U)\mathbf{G}(U)$ loop with the controller designed with a parameter dependent performance bound. The red line is $\omega > 0$, and the green line is $\omega < 0$.

7 Linear Fractional Representation Induced $\mathcal{L}_2$ Control

This chapter is a reformulation of the work published by Prime et al. (2008). A Linear Fractional Transformation (LFT) is performed on the dynamics of the Nonlinear Aeroelastic Test Apparatus (NATA) to remove the quadratic dependence upon airspeed, instead representing it as linear feedback in a Linear Fractional Representation (LFR). An induced $\mathcal{L}_2$ loop-shaping controller is synthesised for this LFR of the NATA, with the controller scheduled with airspeed via being in LFR with its feedback a function of airspeed.

The significant differences between the work in this chapter and in Prime et al. (2008) are that the minimisation of $\mathcal{H}_2$ norm of the gust response has been removed, and the LFR controller is synthesised directly in the continuous domain as opposed to the discrete domain used in Prime et al. (2008).

Previous work by Barker and Balas (1999) performed LFR gain-scheduled control on the Benchmark Active Control Technologies (BACT) wing, with the controller synthesised using a weighted $\mathcal{L}_2$ minimisation framework, and a μ synthesis framework. Significant differences between the work presented in this chapter and that by Barker and Balas (1999) is the use of a different model, different feedback, the use of airspeed for scheduling, the use a $\mathcal{L}_2$ loop-shaping controller synthesis framework, and finally the use of full-block LFR multipliers which reduces conservatism versus the framework used by Barker and Balas (1999).

131

7.1 Linear Fractional Representation of the NATA

The state and input matrices for the three degree-of-freedom NATA model were previously presented in Equations (4.54) and (4.56). The output and feed-through matrices depend upon the chosen output. For the work in this chapter, output feedback is used with $\mathbf{y} = \alpha$.

Written in the compact state-space notation, the state-space model is then

$$\mathbf{G}(U, \alpha) = \left[\begin{array}{c|c} \mathbf{A}(U, \alpha) & \mathbf{B} \\ \hline \mathbf{C} & \mathbf{D} \end{array} \right], \tag{7.1}$$

with $\mathbf{C} = \begin{bmatrix} 0 & 0 & 0 & 0 & 1 & 0 \end{bmatrix}$ and $\mathbf{D} = \mathbf{0}$.

The parameter dependence of the state matrix is structured as

$$\mathbf{A}(U, \alpha) = \mathbf{A}_{p0} + \mathbf{A}_{p1}U + \mathbf{A}_{p2}U^2 + \mathbf{A}_{p3}k_\alpha(\alpha), \tag{7.2}$$

however as was previously done in Section 5.2.1, the torsional stiffness is linearised about $\alpha = 0\,\mathrm{rad}$ such that the state matrix takes the form:

$$\mathbf{A}(U) = \underbrace{\left(\mathbf{A}_{p0} + \mathbf{A}_{p3}k_\alpha(0) \right)}_{\mathbf{A}_{p\hat{0}}} + \mathbf{A}_{p1}U + \mathbf{A}_{p2}U^2. \tag{7.3}$$

This linearisation is justified in Section 5.2.1, and is based on the non-linearity being stabilising, as argued in Section 4.6, and it being more important to suppress the limit-cycle oscillations over a variety of airspeeds.

By applying an LFT, the dependence upon airspeed can be extracted from the main plant, and applied as a feedback of $\Delta(U) \in \mathbf{\Delta}$, as shown in Figure 7.1.
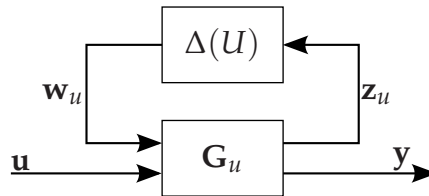

Figure 7.1: Linear Fractional Representation (LFR) of the NATA with the dynamic dependence on airspeed applied as feedback of $\Delta(U)$.

The state-space model of the NATA then takes the form

$$
\mathbf{G}_u : \quad
\left[
\begin{array}{c}
\mathbf{x} \\
\hline
\mathbf{z}_u \\
\hline
\mathbf{y}
\end{array}
\right]
=
\left[
\begin{array}{c|cc}
\hat{\mathbf{A}} & \mathbf{B}_u & \mathbf{B} \\
\hline
\mathbf{C}_u & \mathbf{D}_{uu} & \mathbf{E}_u \\
\hline
\mathbf{C} & \mathbf{F}_u & \mathbf{D}
\end{array}
\right]
\left[
\begin{array}{c}
\mathbf{x} \\
\hline
\mathbf{w}_u \\
\hline
\mathbf{u}
\end{array}
\right].
\tag{7.4}
$$

It is a requirement of the controller synthesis performed below that $\mathbf{\Delta}$ (the set of Δ) must contain $\mathbf{0}$. This can be achieved by rewriting U as

$$
U = U_0 + \delta
\tag{7.5}
$$

where

U_0 is the nominal airspeed, and

δ is the deviation from the nominal airspeed,

and making the feedback a function of δ: $\Delta(\delta)$.

In this instance, the feedback is chosen to take the form

$$
\Delta(\delta) = \delta \mathbf{I}_{6\times6},
\tag{7.6}
$$

and the output LFR vector, $\mathbf{z}_u$, is chosen to be

$$
\mathbf{z}_u = \begin{bmatrix} h & \alpha & \mathbf{w}_u(4) & \alpha & \mathbf{w}_u(6) & \beta \end{bmatrix}^{\mathrm{T}},
\tag{7.7}
$$

where

$\mathbf{w}_u(4)$ refers to the 4th element of the LFR input vector, $\mathbf{w}_u$.

These Δ and $\mathbf{z}_u$ structures were chosen such that Δ was linear in airspeed, with the quadratic airspeed dependence resulting from feeding elements of $\mathbf{w}_u$ back through Δ, resulting in a non-zero $\mathbf{D}_{uu}$.

With Δ and $\mathbf{z}_u$ defined as above, the thus far undefined matrices from the LFT state-space model of the NATA, Equation (7.4), are

$$
\hat{\mathbf{A}} = \mathbf{A}_{p\hat{0}} + \mathbf{A}_{p1} U_0 + \mathbf{A}_{p2} U_0^2,
\tag{7.8}
$$

$$
\mathbf{B}_u =
\begin{bmatrix}
\mathbf{A}_{p1}^{(1:3,1)} & \mathbf{A}_{p1}^{(1:3,2)} & \mathbf{A}_{p2}^{(1:3,5)} & 2U_0\mathbf{A}_{p2}^{(1:3,5)} & \mathbf{A}_{p2}^{(1:3,6)} & 2U_0\mathbf{A}_{p2}^{(1:3,6)} \\
\mathbf{0} & \mathbf{0} & \mathbf{0} & \mathbf{0} & \mathbf{0} & \mathbf{0}
\end{bmatrix},
\tag{7.9}
$$

where for this instance, the superscript is a matrix index, i.e. $\mathbf{A}_{p1}^{(1:3,1)}$ indicates the vector formed from rows 1 to 3 and column 1 of matrix $\mathbf{A}_{p1}$,

$$\mathbf{C}_u = \begin{bmatrix} 1 & 0 & 0 & 0 & 0 & 0 \\ 0 & 1 & 0 & 0 & 0 & 0 \\ 0 & 0 & 0 & 0 & 0 & 0 \\ 0 & 0 & 0 & 0 & 1 & 0 \\ 0 & 0 & 0 & 0 & 0 & 0 \\ 0 & 0 & 0 & 0 & 0 & 1 \end{bmatrix}, \tag{7.10}$$

$$\mathbf{D}_{uu} = \begin{bmatrix} 0 & 0 & 0 & 0 & 0 & 0 \\ 0 & 0 & 0 & 0 & 0 & 0 \\ 0 & 0 & 0 & 1 & 0 & 0 \\ 0 & 0 & 0 & 0 & 0 & 0 \\ 0 & 0 & 0 & 0 & 0 & 1 \\ 0 & 0 & 0 & 0 & 0 & 0 \end{bmatrix}, \tag{7.11}$$

$$\mathbf{E}_u = \mathbf{0}, \text{ and} \tag{7.12}$$

$$\mathbf{F}_u = \mathbf{0}. \tag{7.13}$$

It is important that the LFR be well posed, which requires

$$\mathbf{I} - \mathbf{D}_{uu}\Delta(\delta) \tag{7.14}$$

be invertible for all δ. Given the sparseness of $\mathbf{D}_{uu}$, it is trivial to show that this LFR is well posed.

7.2 Generalised LFR loop-shaping

Using the LFR form of the NATA, a generalised induced $\mathcal{L}_2$ loop-shaping control problem can be constructed as was outlined in Section 2.2.5.2.

Firstly, pre- and post-compensators must be selected to render the singular values of LFR NATA plant desirable, as outlined in Section 2.2.5.2. For the LFR NATA, only a pre-compensator was used, consisting of

- an integrator to increase the low-frequency gain and improve disturbance rejection,

- a gain of 10 to move the 0 dB crossover frequency to approximately 10 rad/s,

- two zeros at $s = 5 \pm 5i$ rad/s to reduce the magnitude roll-off at the 0 dB crossover point, and

- a poles at $s = 50$ rad/s to increase the high-frequency magnitude roll-off to improve robustness against unmodelled dynamics, and render the pre-compensator proper.

This pre-compensator has a state space realisation of

$$
\mathbf{W}_1 = \left[\begin{array}{c|c} \mathbf{A}_\mathrm{w} & \mathbf{B}_\mathrm{w} \\ \hline \mathbf{C}_\mathrm{w} & \mathbf{D}_\mathrm{w} \end{array} \right] = \left[\begin{array}{cc|c} -50 & 0 & 32 \\ 1 & 0 & 0 \\ \hline -12.500 & 15.625 & 10 \end{array} \right]. \tag{7.15}
$$

The singular values of the NATA at $U = 12.0$ m/s, along with the singular values after multiplying it by the pre-compensator are shown in Figure 7.2.
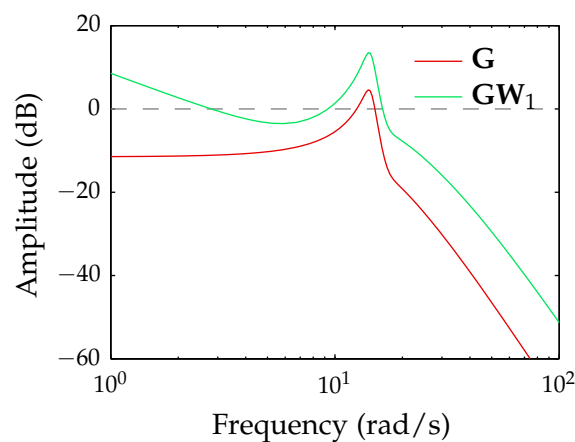

Figure 7.2: Singular values for the NATA, $\mathbf{G}$, at $U = 12.0$ m/s and $\alpha = 0$ rad, and the same NATA multiplied by the pre-compensator $\mathbf{W}_1$.

The pre-compensator can be included in the LFR NATA model to generate the scaled plant:

$$
\mathbf{G}_{us} : \quad
\begin{bmatrix} \mathbf{x} \\ \hline \mathbf{x}_W \\ \hline \mathbf{z}_u \\ \hline \mathbf{y}_s \end{bmatrix}
=
\left[\begin{array}{cc|c|c}
\hat{\mathbf{A}} & \mathbf{BC}_W & \mathbf{B}_u & \mathbf{BD}_W \\
\mathbf{0} & \mathbf{A}_W & \mathbf{0} & \mathbf{B}_W \\ \hline
\mathbf{C}_u & \mathbf{0} & \mathbf{D}_{uu} & \mathbf{E}_u \\ \hline
\mathbf{C} & \mathbf{DC}_W & \mathbf{F}_u & \mathbf{DD}_W
\end{array} \right]
\begin{bmatrix} \mathbf{x} \\ \hline \mathbf{x}_W \\ \hline \mathbf{w}_u \\ \hline \mathbf{u}_s \end{bmatrix}, \qquad (7.16)
$$

which will be denoted as

$$
\mathbf{G}_{us} : \quad
\begin{bmatrix} \mathbf{x}_s \\ \hline \mathbf{z}_u \\ \hline \mathbf{y}_s \end{bmatrix}
=
\left[\begin{array}{c|c|c}
\mathbf{A}_s & \mathbf{B}_{us} & \mathbf{B}_s \\ \hline
\mathbf{C}_{us} & \mathbf{D}_{uu} & \mathbf{E}_u \\ \hline
\mathbf{C}_s & \mathbf{F}_u & \mathbf{D}_s
\end{array} \right]
\begin{bmatrix} \mathbf{x}_s \\ \hline \mathbf{w}_u \\ \hline \mathbf{u}_s \end{bmatrix}. \qquad (7.17)
$$

By defining the performance input and output vectors as $\mathbf{w}_p = [\mathbf{u}_s \quad \mathbf{y}_s]^T$ and $\mathbf{z}_p = [\mathbf{y}_s \quad \mathbf{u}_s]^T$, as per Section 2.2.5.2, the LFR $\mathcal{H}_\infty$ loop-shaping generalised control problem is

$$
\mathbf{P} : \quad
\begin{bmatrix} \mathbf{x}_s \\ \hline \mathbf{z}_u \\ \hline \mathbf{z}_p \\ \hline \mathbf{y}_s \end{bmatrix}
=
\left[\begin{array}{c|c|c|c|c}
\mathbf{A}_s & \mathbf{B}_{us} & \mathbf{B}_s & \mathbf{0} & \mathbf{B}_s \\ \hline
\mathbf{C}_{us} & \mathbf{D}_{uu} & \mathbf{E}_u & \mathbf{0} & \mathbf{E}_u \\ \hline
\mathbf{C}_s & \mathbf{F}_u & \mathbf{0} & \mathbf{I} & \mathbf{0} \\
\mathbf{0} & \mathbf{0} & \mathbf{0} & \mathbf{0} & \mathbf{I} \\ \hline
\mathbf{C}_s & \mathbf{F}_u & \mathbf{0} & \mathbf{I} & \mathbf{D}_s
\end{array} \right]
\begin{bmatrix} \mathbf{x}_x \\ \hline \mathbf{w}_u \\ \hline \mathbf{w}_p \\ \hline \mathbf{u}_s \end{bmatrix}, \qquad (7.18)
$$

which will be denoted as

$$
\mathbf{P} =
\left[\begin{array}{c|c|c|c}
\mathbf{A}_s & \mathbf{B}_{us} & \mathbf{B}_p & \mathbf{B}_s \\ \hline
\mathbf{C}_{us} & \mathbf{D}_{uu} & \mathbf{D}_{up} & \mathbf{E}_u \\ \hline
\mathbf{C}_p & \mathbf{D}_{pu} & \mathbf{D}_{pp} & \mathbf{E}_p \\ \hline
\mathbf{C}_s & \mathbf{F}_u & \mathbf{F}_p & \mathbf{D}_s
\end{array} \right]. \qquad (7.19)
$$

This generalised form of the LFR NATA $\mathcal{H}_\infty$ loop shaping control problem will be used in synthesising a LFR controller below.

7.3 LFR Quadratic performance LMIs

This section outlines the development of the quadratic performance LMIs for use on a system in LFR from, and is based on Scherer (2000), Scherer

(2001), and Scherer and Weiland (2004), as opposed to the more restrictive framework from Apkarian et al. (2000), and Pellanda et al. (2002) that was used in Prime et al. (2008).

Consider the application of a controller, itself in LFR with its feedback dependent upon Δ:

$$
\mathbf{K}: \quad
\left[
\begin{array}{c}
\mathbf{x}_c \\
\hline
\mathbf{u}_s \\
\hline
\mathbf{z}_c
\end{array}
\right]
=
\left[
\begin{array}{c|c|c}
\mathbf{A}_c & \mathbf{B}_{c1} & \mathbf{B}_{c2} \\
\hline
\mathbf{C}_{c1} & \mathbf{D}_{c1} & \mathbf{D}_{c12} \\
\hline
\mathbf{C}_{c2} & \mathbf{D}_{c21} & \mathbf{D}_{c2}
\end{array}
\right]
\left[
\begin{array}{c}
\mathbf{x}_c \\
\hline
\mathbf{y}_s \\
\hline
\mathbf{w}_c
\end{array}
\right],
\tag{7.20}
$$

$$
\mathbf{w}_c = \Delta_c(\Delta)\mathbf{z}_c, \text{ and } \Delta_c \in \boldsymbol{\Delta}_c,
\tag{7.21}
$$

on the generalised control problem Equation (7.19), such that the closed-loop system

$$
\mathcal{G}_{cl}: \quad
\left[
\begin{array}{c}
\mathbf{x}_{cl} \\
\hline
\mathbf{z}_u \\
\hline
\mathbf{z}_c \\
\hline
\mathbf{z}_p
\end{array}
\right]
=
\left[
\begin{array}{c|ccc}
\mathcal{A} & \mathcal{B}_u & \mathcal{B}_c & \mathcal{B}_p \\
\hline
\mathcal{C}_u & \mathcal{D}_{uu} & \mathcal{D}_{uc} & \mathcal{D}_{up} \\
\hline
\mathcal{C}_c & \mathcal{D}_{cu} & \mathcal{D}_{cc} & \mathcal{D}_{cp} \\
\hline
\mathcal{C}_p & \mathcal{D}_{pu} & \mathcal{D}_{pc} & \mathcal{D}_{pp}
\end{array}
\right]
\left[
\begin{array}{c}
\mathbf{x}_{cl} \\
\hline
\mathbf{w}_u \\
\hline
\mathbf{w}_c \\
\hline
\mathbf{w}_p
\end{array}
\right], \text{ and}
\tag{7.22}
$$

$$
\left[
\begin{array}{c}
\mathbf{w}_u \\
\mathbf{w}_c
\end{array}
\right]
=
\left[
\begin{array}{cc}
\Delta & \mathbf{0} \\
\mathbf{0} & \Delta_c(\Delta)
\end{array}
\right]
\left[
\begin{array}{c}
\mathbf{z}_u \\
\mathbf{z}_c
\end{array}
\right]
\tag{7.23}
$$

achieves the quadratic performance specification, as defined in Section 2.3.3:

$$
\mathbf{P}_p =
\left[
\begin{array}{cc}
\mathbf{Q}_p & \mathbf{S}_p \\
\mathbf{S}_p^{\mathrm{T}} & \mathbf{R}_p
\end{array}
\right].
\tag{7.24}
$$

A diagram of this arrangement is shown in Figure 7.3.

When synthesising a quadratic performance controller for a LFR system, a set of extended full-block scalings (Scherer and Weiland 2004):

$$
\mathbf{P}_e =
\left[
\begin{array}{c|c}
\mathbf{Q}_e & \mathbf{S}_e \\
\hline
\mathbf{S}_e^{\mathrm{T}} & \mathbf{R}_e
\end{array}
\right]
=
\left[
\begin{array}{cc|cc}
\mathbf{Q} & \mathbf{Q}_{12} & \mathbf{S} & \mathbf{S}_{12} \\
\mathbf{Q}_{12}^{\mathrm{T}} & \mathbf{Q}_{22} & \mathbf{S}_{12}^{\mathrm{T}} & \mathbf{S}_{22} \\
\hline
\mathbf{S}^{\mathrm{T}} & \mathbf{S}_{12} & \mathbf{R} & \mathbf{R}_{12} \\
\mathbf{S}_{12}^{\mathrm{T}} & \mathbf{S}_{22}^{\mathrm{T}} & \mathbf{R}_{12}^{\mathrm{T}} & \mathbf{R}_{22}
\end{array}
\right], \text{ with } \mathbf{Q}_e \prec 0, \text{ and } \mathbf{R}_e \succ 0,
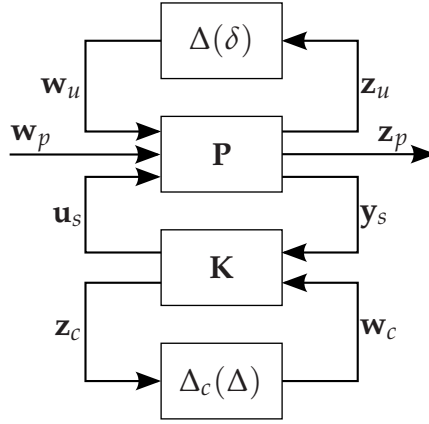\tag{7.25}
$$

Figure 7.3: Closed-loop LFR generalised plant with LFR controller.

must be found that satisfy

$$
\begin{bmatrix}
\Delta & \mathbf{0} \\
\mathbf{0} & \Delta_c(\Delta) \\
\hline
\mathbf{I} & \mathbf{0} \\
\mathbf{0} & \mathbf{I}
\end{bmatrix}^{\mathrm{T}}
\mathbf{P}_e
\begin{bmatrix}
\Delta & \mathbf{0} \\
\mathbf{0} & \Delta_c(\Delta) \\
\hline
\mathbf{I} & \mathbf{0} \\
\mathbf{0} & \mathbf{I}
\end{bmatrix}
\succ 0, \ \forall \Delta \in \mathbf{\Delta}, \ \Delta_c \in \mathbf{\Delta}_c, \tag{7.26}
$$

and

$$
\mathcal{X} \succ 0, \tag{7.27}
$$

$$
\begin{bmatrix}
\mathbf{I} & \mathbf{0} & \mathbf{0} & \mathbf{0} \\
\mathcal{A} & \mathcal{B}_u & \mathcal{B}_c & \mathcal{B}_p \\
\mathbf{0} & \mathbf{I} & \mathbf{0} & \mathbf{0} \\
\mathbf{0} & \mathbf{0} & \mathbf{I} & \mathbf{0} \\
\mathcal{C}_u & \mathcal{D}_{uu} & \mathcal{D}_{uc} & \mathcal{D}_{up} \\
\mathcal{C}_c & \mathcal{D}_{cu} & \mathcal{D}_{cc} & \mathcal{D}_{cp} \\
\mathbf{0} & \mathbf{0} & \mathbf{0} & \mathbf{I} \\
\mathcal{C}_p & \mathcal{D}_{pu} & \mathcal{D}_{pc} & \mathcal{D}_{pp}
\end{bmatrix}^{\mathrm{T}}
\begin{bmatrix}
\mathbf{0} & \mathcal{X} & \mathbf{0} & \mathbf{0} & \mathbf{0} & \mathbf{0} & \mathbf{0} & \mathbf{0} \\
\mathcal{X} & \mathbf{0} & \mathbf{0} & \mathbf{0} & \mathbf{0} & \mathbf{0} & \mathbf{0} & \mathbf{0} \\
\mathbf{0} & \mathbf{0} & \mathbf{Q} & \mathbf{Q}_{12} & \mathbf{S} & \mathbf{S}_{12} & \mathbf{0} & \mathbf{0} \\
\mathbf{0} & \mathbf{0} & \mathbf{Q}_{12}^{\mathrm{T}} & \mathbf{Q}_{22} & \mathbf{S}_{12}^{\mathrm{T}} & \mathbf{S}_{22} & \mathbf{0} & \mathbf{0} \\
\mathbf{0} & \mathbf{0} & \mathbf{S}^{\mathrm{T}} & \mathbf{S}_{12} & \mathbf{R} & \mathbf{R}_{12} & \mathbf{0} & \mathbf{0} \\
\mathbf{0} & \mathbf{0} & \mathbf{S}_{12}^{\mathrm{T}} & \mathbf{S}_{22}^{\mathrm{T}} & \mathbf{R}_{12}^{\mathrm{T}} & \mathbf{R}_{22} & \mathbf{0} & \mathbf{0} \\
\mathbf{0} & \mathbf{0} & \mathbf{0} & \mathbf{0} & \mathbf{0} & \mathbf{0} & \mathbf{Q}_p & \mathbf{S}_p \\
\mathbf{0} & \mathbf{0} & \mathbf{0} & \mathbf{0} & \mathbf{0} & \mathbf{0} & \mathbf{S}_p^{\mathrm{T}} & \mathbf{R}_p
\end{bmatrix}
\begin{bmatrix}
* \\
* \\
* \\
* \\
* \\
* \\
* \\
*
\end{bmatrix}
\prec 0,
$$

$$\tag{7.28}$$

where $*$ has been used instead of repeating the left matrix, in order to reduce the length of the expression. Note that the closed-loop Lyapunov matrix, $\mathcal{X}$, is not parameter dependent due the parameter dependence of the closed-loop system being in the LFR feedback terms.

Defining the scalings for just the plant LFR as

$$\mathbf{P} = \begin{bmatrix} \mathbf{Q} & \mathbf{S} \\ \mathbf{S}^T & \mathbf{R} \end{bmatrix}, \tag{7.29}$$

and its inverse as

$$\mathbf{P}^{-1} = \tilde{\mathbf{P}} = \begin{bmatrix} \tilde{\mathbf{Q}} & \tilde{\mathbf{S}} \\ \tilde{\mathbf{S}}^T & \tilde{\mathbf{R}} \end{bmatrix}, \tag{7.30}$$

and defining the inverse of the quadratic performance specification

$$\mathbf{P}_p^{-1} = \tilde{\mathbf{P}}_p = \begin{bmatrix} \tilde{\mathbf{Q}}_p & \tilde{\mathbf{S}}_p \\ \tilde{\mathbf{S}}_p^T & \tilde{\mathbf{R}}_p \end{bmatrix}, \tag{7.31}$$

the nonlinear (in the variables) Equation (7.28) can be linearised through Dualization (Scherer 2000), such that the synthesis problem becomes a set of LMIs in the variables $\mathbf{X}$, $\mathbf{Y}$, $\mathbf{P}$, $\tilde{\mathbf{P}}$, $\mathbf{P}_p$, and $\tilde{\mathbf{P}}_p$. Note that $\mathbf{P}_p$ and $\tilde{\mathbf{P}}_p$ are not free variables; their form is usually specified with regards to a performance index, which is the variable. For example, for induced $\mathcal{L}_2$ control the quadratic performance specification is

$$\mathbf{P}_p = \begin{bmatrix} -\gamma \mathbf{I} & \mathbf{0} \\ \mathbf{0} & \gamma^{-1} \mathbf{I} \end{bmatrix}, \tag{7.32}$$

and γ can be treated as the scalar variables for LMI optimisation.

Assuming that the full set of parameter values, $\Delta(\delta)$, are captured by the convex hull

$$\Delta := \text{conv}\{\Delta_1, \ldots, \Delta_N\}, \tag{7.33}$$

the synthesis LMI problem is (Scherer and Weiland 2004)

$$\begin{bmatrix} \Delta_j \\ \mathbf{I} \end{bmatrix}^T \mathbf{P} \begin{bmatrix} \Delta_j \\ \mathbf{I} \end{bmatrix} \succ 0, \text{ for } j = 1, \ldots, N, \tag{7.34}$$

$$\begin{bmatrix} \mathbf{I} \\ -\Delta_j^T \end{bmatrix}^T \tilde{\mathbf{P}} \begin{bmatrix} \mathbf{I} \\ -\Delta_j^T \end{bmatrix} \prec 0, \text{ for } j = 1, \ldots, N, \tag{7.35}$$

$$\begin{bmatrix} \mathbf{Y} & \mathbf{I} \\ \mathbf{I} & \mathbf{X} \end{bmatrix} \succ 0, \tag{7.36}$$

$$\psi^{\mathrm{T}} \left[\begin{array}{ccc} \mathbf{I} & \mathbf{0} & \mathbf{0} \\ \hline \mathbf{A}_s & \mathbf{B}_{us} & \mathbf{B}_p \\ \hline \mathbf{0} & \mathbf{I} & \mathbf{0} \\ \mathbf{C}_{us} & \mathbf{D}_{uu} & \mathbf{D}_{up} \\ \hline \mathbf{0} & \mathbf{0} & \mathbf{I} \\ \mathbf{C}_p & \mathbf{D}_{pu} & \mathbf{D}_{pp} \end{array}\right]^{\mathrm{T}} \left[\begin{array}{cc|cc|cc} \mathbf{0} & \mathbf{X} & \mathbf{0} & \mathbf{0} & \mathbf{0} & \mathbf{0} \\ \mathbf{X} & \mathbf{0} & \mathbf{0} & \mathbf{0} & \mathbf{0} & \mathbf{0} \\ \hline \mathbf{0} & \mathbf{0} & \mathbf{Q} & \mathbf{S} & \mathbf{0} & \mathbf{0} \\ \mathbf{0} & \mathbf{0} & \mathbf{S}^{\mathrm{T}} & \mathbf{R} & \mathbf{0} & \mathbf{0} \\ \hline \mathbf{0} & \mathbf{0} & \mathbf{0} & \mathbf{0} & \mathbf{Q}_p & \mathbf{S}_p \\ \mathbf{0} & \mathbf{0} & \mathbf{0} & \mathbf{0} & \mathbf{S}_p^{\mathrm{T}} & \mathbf{R}_p \end{array}\right] \left[\begin{array}{c} * \\ * \\ \hline * \\ * \\ \hline * \\ * \end{array}\right] \psi \prec 0,$$

$$(7.37)$$

again using $*$ to denote the repeated matrix, and

$$\phi^{\mathrm{T}} \left[\begin{array}{ccc} -\mathbf{A}_s^{\mathrm{T}} & -\mathbf{C}_{us}^{\mathrm{T}} & -\mathbf{C}_p^{\mathrm{T}} \\ \hline \mathbf{I} & \mathbf{0} & \mathbf{0} \\ \hline -\mathbf{B}_{us}^{\mathrm{T}} & -\mathbf{D}_{uu}^{\mathrm{T}} & -\mathbf{D}_{pu}^{\mathrm{T}} \\ \mathbf{0} & \mathbf{I} & \mathbf{0} \\ \hline -\mathbf{B}_p^{\mathrm{T}} & -\mathbf{D}_{pu}^{\mathrm{T}} & -\mathbf{D}_{pp}^{\mathrm{T}} \\ \mathbf{0} & \mathbf{0} & \mathbf{I} \end{array}\right]^{\mathrm{T}} \left[\begin{array}{cc|cc|cc} \mathbf{0} & \mathbf{Y} & \mathbf{0} & \mathbf{0} & \mathbf{0} & \mathbf{0} \\ \mathbf{Y} & \mathbf{0} & \mathbf{0} & \mathbf{0} & \mathbf{0} & \mathbf{0} \\ \hline \mathbf{0} & \mathbf{0} & \tilde{\mathbf{Q}} & \tilde{\mathbf{S}} & \mathbf{0} & \mathbf{0} \\ \mathbf{0} & \mathbf{0} & \tilde{\mathbf{S}}^{\mathrm{T}} & \tilde{\mathbf{R}} & \mathbf{0} & \mathbf{0} \\ \hline \mathbf{0} & \mathbf{0} & \mathbf{0} & \mathbf{0} & \tilde{\mathbf{Q}}_p & \tilde{\mathbf{S}}_p \\ \mathbf{0} & \mathbf{0} & \mathbf{0} & \mathbf{0} & \tilde{\mathbf{S}}_p^{\mathrm{T}} & \tilde{\mathbf{R}}_p \end{array}\right] \left[\begin{array}{c} * \\ * \\ \hline * \\ * \\ \hline * \\ * \end{array}\right] \phi \succ 0,$$

$$(7.38)$$

where

ψ is the nullspace of $[\mathbf{C}_s \quad \mathbf{F}_u \quad \mathbf{F}_p]$, and

ϕ is the nullspace of $[\mathbf{B}_s^{\mathrm{T}} \quad \mathbf{E}_u^{\mathrm{T}} \quad \mathbf{E}_p^{\mathrm{T}}]$.

Once these LMIs have been solved for $\mathbf{X}$, $\mathbf{Y}$, $\mathbf{P}$, $\tilde{\mathbf{P}}$, $\mathbf{P}_p$, and $\tilde{\mathbf{P}}_p$, the extended scalings, $\mathbf{P}_e$ must be reconstructed. A method for doing this is given in Scherer (2000), where the extended scalings are partitioned as

$$\mathbf{P}_e = \mathbf{Z}^{\mathrm{T}} \begin{bmatrix} \mathbf{P} & \mathbf{T} \\ \mathbf{T}^{\mathrm{T}} & \mathbf{T}^{\mathrm{T}}\mathbf{N}\mathbf{T} \end{bmatrix} \mathbf{Z}, \qquad (7.39)$$

where

$\mathbf{N} = (\mathbf{P} - \tilde{\mathbf{P}}^{-1})^{-1}$,

$\mathbf{T}$ must be constructed to satisfy the positivity/negativity constraints $\mathbf{Q}_e \prec 0$ and $\mathbf{R}_e \succ 0$, and

$\mathbf{Z}$ is the permutation matrix

$$\mathbf{Z} = \begin{bmatrix} \mathbf{I} & \mathbf{0} & \mathbf{0} & \mathbf{0} \\ \mathbf{0} & \mathbf{0} & \mathbf{I} & \mathbf{0} \\ \mathbf{0} & \mathbf{I} & \mathbf{0} & \mathbf{0} \\ \mathbf{0} & \mathbf{0} & \mathbf{0} & \mathbf{I} \end{bmatrix}, \qquad (7.40)$$

One method of constructing $\mathbf{T}$ is to partition it as $\mathbf{T} = \begin{bmatrix} \mathbf{T}_1 & \mathbf{T}_2 \end{bmatrix}$, where $\mathbf{T}_1$ and $\mathbf{T}_2$ have the same number of columns as there are negative and positive eigenvalues of $\mathbf{N}$ respectively, and find values for each that satisfy (Scherer 2000)

$$\mathbf{T}_1^{\mathsf{T}} \left(\mathbf{N} - \begin{bmatrix} \mathbf{Q}^{-1} & \mathbf{0} \\ \mathbf{0} & \mathbf{0} \end{bmatrix} \right) \mathbf{T}_1 \prec 0, \text{ and} \tag{7.41}$$

$$\mathbf{T}_2^{\mathsf{T}} \left(\mathbf{N} - \begin{bmatrix} \mathbf{0} & \mathbf{0} \\ \mathbf{0} & \mathbf{R}^{-1} \end{bmatrix} \right) \mathbf{T}_2 \succ 0. \tag{7.42}$$

This can be satisfied by selecting $\mathbf{T}_1$ and $\mathbf{T}_2$ to be the eigenvectors that correspond to the negative and positive eigenvalues respectively of

$$\left(\mathbf{N} - \begin{bmatrix} \mathbf{Q}^{-1} & \mathbf{0} \\ \mathbf{0} & \mathbf{0} \end{bmatrix} \right) \text{ and } \left(\mathbf{N} - \begin{bmatrix} \mathbf{0} & \mathbf{0} \\ \mathbf{0} & \mathbf{R}^{-1} \end{bmatrix} \right)$$

respectively.

The controller scheduling function, $\Delta_c(\Delta)$, can then be calculated using (Scherer 2000)

$$\mathbf{U} = \mathbf{R}_e - \mathbf{S}_e^{\mathsf{T}} \mathbf{Q}_e^{-1} \mathbf{S}_e \succ 0, \ \mathbf{V} = -\mathbf{Q}_e^{-1} \succ 0, \text{ and } \mathbf{W} = \mathbf{Q}_e^{-1} \mathbf{S}_e, \tag{7.43}$$

with $\mathbf{U}$, $\mathbf{V}$, and $\mathbf{W}$ all partitioned as

$$\mathbf{U} = \begin{bmatrix} \mathbf{U}_{11} & \mathbf{U}_{12} \\ \mathbf{U}_{21} & \mathbf{U}_{22} \end{bmatrix}, \tag{7.44}$$

where

$\mathbf{U}_{11}$ has the same dimensions as Δ. Correspondingly, $\mathbf{U}_{22}$ has the same dimensions as $\Delta_c(\Delta)$.

The controller scheduling function is then

$$\Delta_c(\Delta) = -\mathbf{W}_{22} + \begin{bmatrix} \mathbf{W}_{21} & \mathbf{V}_{21} \end{bmatrix} \begin{bmatrix} \mathbf{U}_{11} & \mathbf{W}_{11}^{\mathsf{T}} + \Delta^{\mathsf{T}} \\ \mathbf{W}_{11} + \Delta & \mathbf{V}_{11} \end{bmatrix}^{-1} \begin{bmatrix} \mathbf{U}_{12} \\ \mathbf{W}_{12} \end{bmatrix}.$$
$$\tag{7.45}$$

Finally, the controller variables can be reconstructed by directly solving the closed-loop quadratic performance LMI Equation (7.28) with the controller variables as the LMI variables, and with the closed-loop Lyapunov matrix, Equation (7.27), reconstructed as per Section 2.3.4.

7.4   Induced $\mathcal{L}_2$ LFR controller construction

Using the theory outlined above in Section 7.3, a controller can be constructed based on the induced $\mathcal{L}_2$ ($\mathcal{H}_\infty$) loop-shaping generalised control problem from Section 7.2. For induced $\mathcal{L}_2$ control, the quadratic performance index is

$$\mathbf{P}_p = \begin{bmatrix} -\gamma\mathbf{I} & \mathbf{0} \\ \mathbf{0} & \gamma^{-1}\mathbf{I} \end{bmatrix}, \tag{7.46}$$

as per Equation (2.73), and applying a Schur complement transformation (Section 2.3.3) to the expanded forms of Equations (7.37) and (7.38) to linearise the LMIs with respect to γ. Note that with the NATA dynamics represented in LFR, the airspeed dependence is entirely contained in the feedback term, hence the performance index, γ, can not be made parameter dependent, and thus cannot use the work from Chapter 6.

For a nominal airspeed of $U_0 = 12.0\,\text{m/s}$, the synthesis LMIs were solved for varying deviation ranges by equally varying the upper and lower values of δ, $\bar{\delta}$ and $\underline{\delta}$ respectively, such that $\bar{\delta} = -\underline{\delta}$. The resulting values of γ are plotted in Figure 7.4.

Skogestad and Postlethwaite (2005) state that during $\mathcal{H}_\infty$ (induced $\mathcal{L}_2$) loop-shaping, the $\mathcal{H}_\infty$ (induced $\mathcal{L}_2$) performance, γ, should be kept below a value of 4. Thus, an airspeed deviation of $\bar{\delta} = -\underline{\delta} = 2.2\,\text{m/s}$ was selected based on the results from Figure 7.4, which resulted in an optimum induced $\mathcal{L}_2$ performance value of $\gamma = 3.91$. It is well known
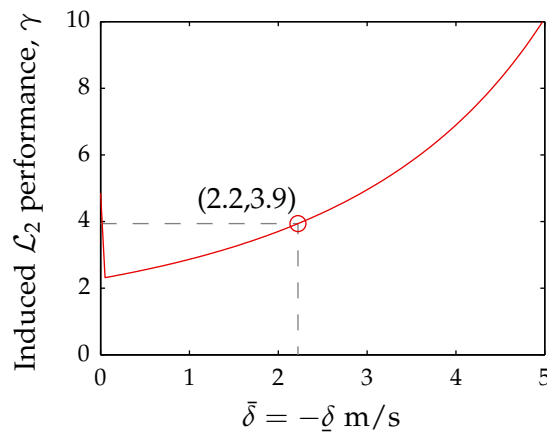

Figure 7.4: Induced $\mathcal{L}_2$ performance values, γ, for varying airspeed deviations about the nominal airspeed of $U_0 = 12.0\,\text{m/s}$.

that induced $\mathcal{L}_2$ control problems often have poor numerical conditioning around optimality, hence the induced $\mathcal{L}_2$ performance value was relaxed to $\gamma = 3.99$, before solving the LMIs again.

The controller was then reconstructed using the method described in Section 7.3. The controller scheduling function, $\Delta_c(\Delta)$ can be symbolically calculated as a function of δ, however it becomes a large and poorly conditioned rational function of δ due to the matrix inversion. It is therefore more computationally efficient to calculate Equation (7.45) numerically at each time step.

The numeric values of the controller matrices, Equation (7.20), and the scheduling matrices, Equation (7.45), can be found on the additional materials CD, or as an attachment to the PDF version of this document.

7.5   Results

After applying the synthesised controller to the generalised plant, the frequency response of the induced $\mathcal{L}_2$ performance channel is plotted in Figure 7.5 for the minimum, maximum and nominal airspeed design range. The maximum gain in each performance channel does not exceed 12.0 dB ($\gamma = 3.99$), which is expected from the controller design.

A perturbation test for the NATA, with the plunge initially perturbed to 0.03 m, controlled by the induced $\mathcal{L}_2$ loop-shaping LFR controller was simulated while the airspeed changed from $U = U_0 + \underline{\delta}$ to $U = U_0 + \bar{\delta}$. The results of this test are shown in Figure 7.6, and show that the controller is able to settle the system in approximately 2.5 s, and keep the NATA stable while the airspeed is varying without saturating the servo-motor attached to the trailing-edge control surface. These results are similar in both settling time and actuator demands to those presented for the $\mathcal{H}_2$ based LPV LQR controller in Figures 5.7, 5.8 and 5.9, and the $\mathcal{GH}_2$ based LPV LQR controller in Figure 5.13, despite the differences in control structure.

A limit-cycle oscillation test was also simulated while the airspeed changed from $U = U_0 + \underline{\delta}$ to $U = U_0 + \bar{\delta}$. The NATA output, **y**, was disconnected from the controller to prevent the controller dynamics becoming excited while the limit-cycle oscillations were allowed to grow. At $t = 5$ s the NATA output was reconnected to the controller. The
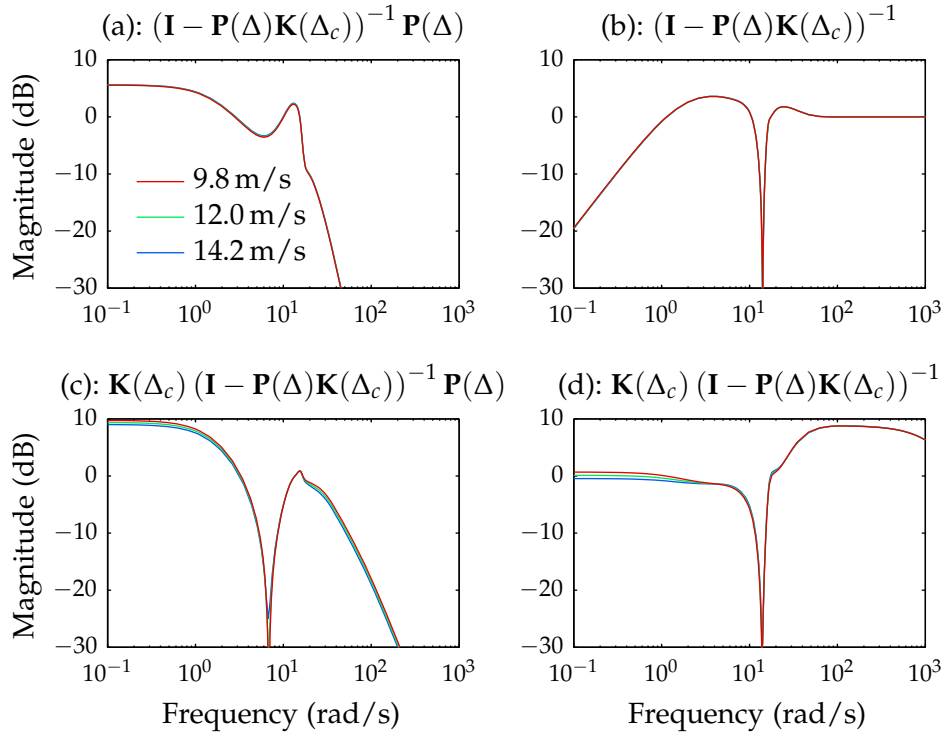
Figure 7.5: Closed-loop performance channel gains for different airspeeds. Notice the maximum gain (induced $\mathcal{L}_2$ norm) does not exceed $12.0\,\mathrm{dB}$ ($\gamma = 3.99$). Transfer functions (b) and (c) are more commonly known as the Sensitivity and Complementary Sensitivity transfer functions respectively. Transfer functions (a) and (d) are from $\mathbf{u}_s$ to $\mathbf{y}_s$ and from $\mathbf{y}_s$ to $\mathbf{u}_s$ respectively.

results of this test are shown in Figure 7.7, and show that when first activated, there is a large jump in the control signal, which is due to the sudden activation of the output, equivalent to a step input into the controller dynamics. Despite this, the controller is able to suppress the limit-cycle oscillations in pitch after approximately one second, while small oscillations persist in plunge for another two seconds. This pitch settling time is similar to those results presented earlier for the $\mathcal{H}_2$ based LPV LQR controller in Figures 5.4, 5.5 and 5.6, and the $\mathcal{GH}_2$ based LPV LQR controller in Figure 5.13, however the plunge settling time and actuator demands when first activated for the loop-shaping LFR controller presented here are worse than those presented earlier. The increased plunge settling time for the loop-shaping LFR controller is due
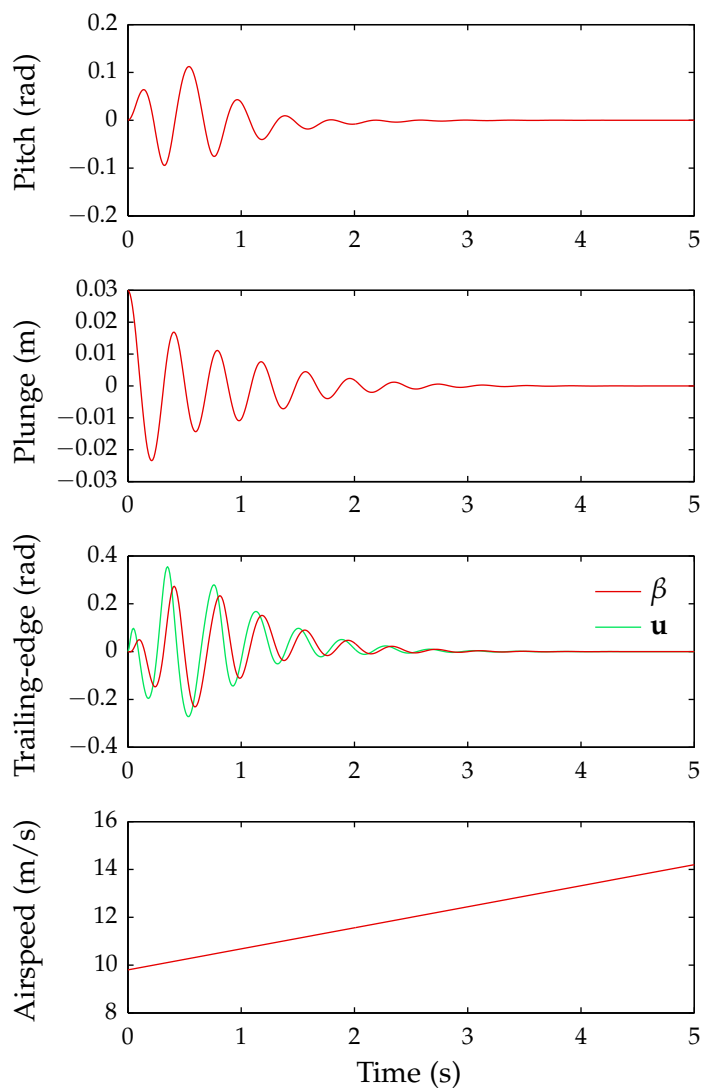
Figure 7.6: Results of a perturbation simulation performed on the NATA controlled by the induced $\mathcal{L}_2$ loop-shaping LFR controller while the airspeed is linearly increasing from 9.8 m/s to 14.2 m/s over a 5 s period. The plunge was initially perturbed to 0.03 m at the start of the simulation.

to the controller only acting on pitch output, as opposed to the full-state feedback that was used for the LPV LQR based controllers.

Similar simulations were performed for the NATA operating at fixed airspeeds within the airspeed design range, however the results show little difference to those presented above and have not been included. This is to be expected, due to the similarity in singular values of the closed-loop systems, as shown in Figure 7.5.

7.6   Comparisons to LPV LQR control

One of the primary motivations in representing the NATA as an LFR was to remove the quadratic dependence upon airspeed from the model. As a result of this, during controller synthesis it is no longer necessary to grid the parameter space as was done in Chapter 5. This resulted in shorter LMI solving times. While the controller itself remains fixed using this LFR approach, its scheduling function, Δ_c, becomes a complicated function of the plant scheduling, Δ, resulting in little computational benefit when doing real-time control compared to the LPV LQR approach.

The approach presented in Chapter 5 utilised a parameter dependent Lyapunov matrix which enabled the NATA to be scheduled over a large range of airspeeds. The LFR approach in this chapter only uses a fixed Lyapunov matrix, hence the range of airspeeds that the NATA can be controlled is more restricted, although they cover most of the unstable operating range of the real NATA.

A fixed Lyapunov matrix requires no restriction on the parameter variation rate, so the controller presented in this chapter requires neither a measure of the parameter derivative, which is usually hard to measure, nor a requirement that $U \approx 0$ as was required for the LPV LQR approach presented in Chapter 5.
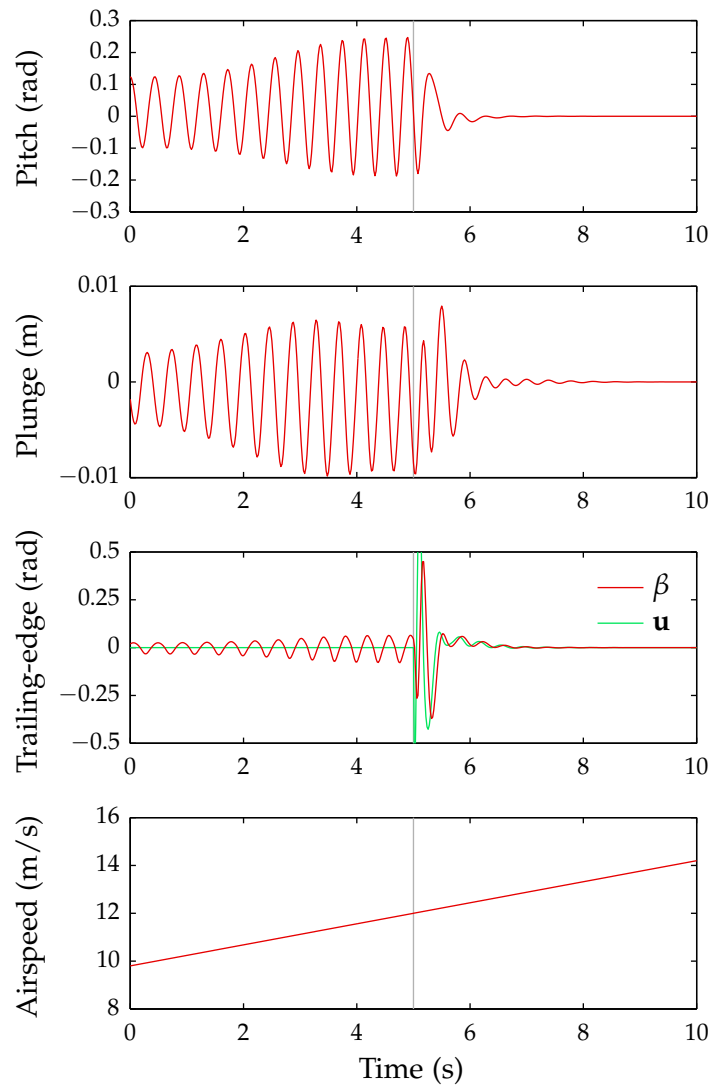
Figure 7.7: Results of a limit-cycle oscillation simulation performed on the NATA controlled by the induced $\mathcal{L}_2$ loop-shaping LFR controller while the airspeed is linearly increasing from $9.8\,\mathrm{m/s}$ to $14.2\,\mathrm{m/s}$ over a $10\,\mathrm{s}$ period.

7.7 Conclusions

Using the generalised control problem form for induced $\mathcal{L}_2$ loop-shaping controller synthesis, a controller which is robust against coprime uncertainty can be synthesised. Additionally, when the plant is in LFR, the controller can be synthesised such that it too is in LFR, scheduled as a function of the plant LFR feedback.

Applying a LFT to a parameter dependent plant is an effective method of linearising rational parameter dependent nonlinear systems. This removes the need for parameter space gridding, which greatly decreases the time required for controller synthesis.

The LFR quadratic performance control synthesis presented utilises a fixed closed-loop Lyapunov matrix, which results in a limited range over which the controller can schedule and provide acceptable performance bounds. Similarly, the performance index cannot be made parameter dependent, and thus the work from Chapter 6 can not be used for LFR control.

8 Conclusions and Future Work

The aim of this research was to create and implement novel aeroelasticity control schemes to robustly suppress undesirable aeroelastic phenomena such as utter and limit-cycle oscillations. The following section summarises and draws conclusions from the work presented in this thesis, while possible future work is outlined in Section 8.2.

8.1 Conclusions

To address the lack of actuator dynamics found in many examples of aeroelasticity control work, new three and four degree-of-freedom dynamic models were derived for the Nonlinear Aeroelastic Test Apparatus (NATA) when considering only trailing-edge, as well as leading- and trailing-edge control respectively. Using a variety of methods the parameters of the new dynamic models were identified, and using the new dynamic models it was shown that the torsional stiffness nonlinearity prevents instability, and thus the focus of the work would be to schedule the controller with airspeed.

A Linear Parameter Varying (LPV) controller was designed to suppress limit-cycle oscillations on the three degree-of-freedom NATA. The LPV synthesis method utilised a parameter dependent transformed Lyapunov matrix, which allowed the controller to schedule over a larger range of airspeeds than is achievable with a fixed transformed Lyapunov matrix.

This controller was based on the Linear Quadratic Regulator (LQR) framework, which was represented as a $\mathcal{H}_2$ minimisation generalised control problem. Experimental results show that this control method achieves effective limit-cycle oscillation suppression and disturbance rejection at a variety of airspeeds while only placing moderate demands

149

on the trailing-edge actuator. In particular, the moderate actuator demands are far more acceptable than many results published that use high-gain backstepping derived controllers, especially in the presence of unmodelled dynamics.

Although this LPV LQR controller did not achieve the classical robustness measures of a normal LQR controller, it was shown to be have acceptable robustness across the airspeed design range. Futhermore, as this control scheme is based on the popular optimal control framework, and provides performance guarantees across the design range, it fits in well with traditional forms of aerospace control.

During the control synthesis, it was found that the upper performance bound, ν, was limited by the worst point-wise optimal performance bound in the airspeed design range. Thus, a new technique of allowing the performance bound to be parameter dependent was introduced, and solved by minimising the integral of the performance.

Using the same LPV LQR controller, it was shown that with a parameter dependent performance bound significantly reduced the upper performance bound, hence increasing performance, across most of the design airspeed.

The resulting LPV LQR controller with parameter dependent performance bound was shown to be slightly less robust than the LPV LQR controller with a fixed performance bound. However this technique would still be especially useful for control problems where the robustness is tied to the performance bound, such as in various types of $\mathcal{H}_\infty$ or induced $\mathcal{L}_2$ control synthesis.

The dynamics of the NATA were then transformed into Linear Fractional Representation (LFR), with the airspeed dependence being linearly contained within the feedback term. Using the generalised control problem form for induced $\mathcal{L}_2$ loop-shaping controller synthesis, a controller, itself in LFR as a function of the NATA LFR feedback, which is robust against coprime uncertainty, was synthesised for the NATA in LFR.

Due to the feedback term being linear in the parameter, it was no longer necessary to grid the parameter space during controller synthesis, requiring the Linear Matrix Inequalities (LMIs) only be solved at the vertices of the linearised parameter space. Thus, applying a Linear Fractional Transformation (LFT) to a parameter dependent plant is an effective method of linearising rational parameter dependence and

reducing the size of the controller synthesis problem.

Unfortunately, performing the LFT on the NATA dynamics removes the parameter dependence from the controller synthesis matrices, hence only a fixed transformed Lyapunov matrix and fixed performance bound can be used for LFR controller synthesis. This results in a reduced scheduling range, and the performance bound is limited by the worst-case over the design range. However, the fixed transformed Lyapunov matrix requires no restriction on the rate of parameter variation, and hence requires neither a measure of the parameter derivative, which is usually hard to measure, nor a requirement that the parameter derivative approximately equals zeros.

8.2 Future work

As possible future work, the control frameworks outlined in this thesis could be applied to the BACT system, which operates at transonic speeds. Given the fidelity of LPV models for the BACT which schedule with Mach number and dynamic pressure, it is expected that this application of these control schemes would be straight forward.

As the LPV LQR control scheme presented in this thesis is based on state-feedback control, the synthesis LMIs should be scalable, and hence as future work could be applied to higher-order aeroelastic models, such as modal models. However, the LMIs solutions become poorly conditioned when the problems become too large, which is often due to a large number of scheduling parameters or grid synthesis points. As the LFR control methodology presented in this thesis avoid the use of gridding a non-affine parameter space, it is expected that this would scale well to higher-order models, with the downside being that it uses a parameter independent transformed Lyapunov matrix, which restricts the available scheduling range.

Other possible future work could include applying the method of reducing the performance bound to robust control problems where the robustness is tied to the performance bound, such as induced $\mathcal{L}_2$ loop-shaping control.

Acknowledgement and Disclaimer

THE SIR ROSS & SIR KEITH SMITH FUND

References

Anderson, B. D. and J. B. Moore (1989). *Optimal control: linear quadratic methods*. Englewood Cliffs, N.J.: Prentice-Hall. See pp. 22, 39.

Apkarian, P. and R. J. Adams (1998). "Advanced gain-scheduling techniques for uncertain systems". In: *IEEE Transactions on Control System Technology* Vol. 6, No. 1, pp. 21–32. See pp. xiv, 31, 41.

Apkarian, P. and H. D. Tuan (2000). "Parameterized LMIs in control theory". In: *SIAM Journal on Control and Optimization* Vol. 38, No. 4, pp. 1241–1264. DOI: 10.1137/S036301299732612X. See p. 41.

Apkarian, P., P. Gahinet, and G. Becker (1995). "Self-scheduled $\mathcal{H}_\infty$ control of linear parameter-varying systems: a design example". In: *Automatica* Vol. 31, No. 9, pp. 1251–1261. See pp. 28, 40.

Apkarian, P., P. C. Pellanda, and H. D. Tuan (2000). "Mixed $\mathcal{H}_2/\mathcal{H}_\infty$ multi-channel linear parameter-varying control in discrete time". In: *Systems & Control Letters* Vol. 41, pp. 333–346. DOI: 10.1016/S0167-6911(00)00076-1. See pp. 42, 137.

Baldelli, D. H., R. Lind, and M. Brenner (2008). "Control-oriented utter/limit-cycle-oscillation prediction framework". In: *AIAA Journal of Guidance, Control and Dynamics* Vol. 31, No. 6, pp. 1634–1643. DOI: 10.2514/1.36117. See p. 45.

Barker, J. M. and G. J. Balas (1999). "Gain-scheduled linear fractional control for active utter suppression". In: *AIAA Journal of Guidance, Control and Dynamics* Vol. 22, No. 4, pp. 507–512. DOI: 10.2514/2.4418. See pp. 44, 47, 48, 131.

— (2000). "Comparing linear parameter-varying gain-scheduled control techniques for active utter suppression". In: *AIAA Journal of Guidance, Control and Dynamics* Vol. 23, No. 5, pp. 948–955. DOI: 10.2514/2.4637. See pp. 44, 48, 53.

Bhoir, N. and S. N. Singh (2004). "Output feedback nonlinear control of an aeroelastic system with unsteady aerodynamics". In: *Aerospace Science and Technology* Vol. 8, No. 3, pp. 195–205. DOI: 10.1016/j.ast.2003.10.009. See p. 50.

Block, J. J. (1996). "Active control of an aeroelastic structure". MA thesis. Texas A&M University. See p. 48.

Block, J. J. and T. W. Strganac (1998). "Applied active control for a nonlinear aeroelastic structure". In: *AIAA Journal of Guidance, Control and Dynamics* Vol. 21, No. 6, pp. 838–845. DOI: 10.2514/2.4346. See pp. 45, 48, 55.

Blue, P. A. and G. J. Balas (1997). *Linear parameter varying control for active utter suppression*. AIAA Paper 97-3640. Aug. 1997. See pp. 44, 47.

Bourn, S. (2000). *Hydrofoil Sail Craft*. International Patent Number: WO 00/26083. See p. 3.

— (2001). *A Fundamental Theory of Sailing and its application to the design of a Hydrofoil Sail Craft*. Unpublished. See p. 3.

Boyd, S. and L. Vandenberghe (2004). *Convex optimization*. Cambridge: Cambridge University Press. See p. 18.

Boyd, S., L. El Ghaoui, E. Feron, and V. Balakrishnan (1994). *Linear matrix inequalities in system and control theory*. Philadelphia: Society for Industrial and Applied Mathematics. See pp. 14, 20, 22, 23, 40.

Collar, A. R. (1946). "The expanding domain of aeroelasticity". In: *Journal of the Royal Aeronautical Society* Vol. 50, No. 428, pp. 613–636. See p. 43.

Cox, D. E. (2003). "Control design for parameter dependent aeroelastic systems". PhD thesis. Duke University. See pp. 31, 44, 51, 68, 69.

Craig, J. J. (2005). *Introduction to robotics: mechanics and control*. 3rd. Upper Saddle River, NJ: Pearson Education. See p. 69.

De Marqui Jr, C., E. M. Belo, and F. D. Marques (2005). "A utter suppression active controller". In: *Proc. IMechE Part G: J. Aerospace Engineering* Vol. 219, No. 3, pp. 19–33. See p. 51.

Dowell, E. H., R. Clark, D. Cox, H. Curtiss Jr., J. W. Edwards, K. H. Hall, D. A. Peters, R. Scanlan, E. Simiu, F. Sisto, and T. W. Strganac (2004). *A modern course in aeroelasticity*. Kluwer Academic Publishers. See pp. 31, 36, 44.

Erwin, R., D. Bernstein, and D. Wilson (2000). "Fixed-structure synthesis of induced-norm controllers". In: *International Journal of Control* Vol. 73,

No. 16, pp. 1437–1448. DOI: 10.1080/00207170050163314. See pp. 116, 123.

Feron, E., V. Balakrishnan, S. Boyd, and L. E. Ghaoui (1992). "Numerical methods for $\mathcal{H}_2$ related problems". In: *Proceedings American Control Conference*. American Automatic Control Council, Evanston, IL, pp. 2921–2922. See pp. 15, 100.

Franklin, G. G., J. D. Powell, and A. Emami-Naeini (1994). *Feedback control of dynamic systems*. Ed. by Horesta, G. J. 3rd. Reading, Mass.: Addison-Wesley. See p. 8.

Fung, Y. C. (1955). *An introduction to the theory of aeroelasticity*. Ed. by Millikan, C. B. NY: John Wiley & Sons. See pp. 36, 37, 43.

Gahinet, P. and P. Apkarian (1994). "A linear matrix inequality approach to $\mathcal{H}_\infty$ control". In: *International Journal of Robust and Nonlinear Control* Vol. 4, No. 4, pp. 421–448. See pp. 23, 40.

Gahinet, P., P. Apkarian, and M. Chilali (1996). "Affine parameter-dependent Lyapunov functions for real parametric uncertainty". In: *IEEE Transactions on Automatic Control* Vol. 41, No. 3, pp. 436–442. DOI: 10.1109/9.486646. See p. 40.

Glover, K. and D. McFarlane (1989). "Robust stabilization of normalised coprime factor plant descriptions with $\mathcal{H}_\infty$-bounded uncertainty". In: *IEEE Transactions on Automatic Control* Vol. 34, No. 8, pp. 821–830. See p. 16.

Hiret, A., G. Duc, J. P. Friang, and D. Farret (2001). "Linear-parameter varying/loop-shaping $\mathcal{H}_\infty$ synthesis for a missile autopilot". In: *AIAA Journal of Guidance, Control and Dynamics* Vol. 24, No. 5, pp. 879–886. See p. 42.

Kalman, R. E. (1964). "When is a linear control system optimal". In: *Journal of Basic Engineering—Transactions of the ASME—Series D* Vol. 86, No. 1, pp. 51–60. See p. 107.

Karpel, M. (1982). "Design for active flutter suppression and gust alleviation using state-space aeroelastic modeling". In: *AIAA Journal of Aircraft* Vol. 19, No. 3, pp. 221–227. DOI: 10.2514/3.57379. See p. 46.

Khalil, H. K. (1996). *Nonlinear systems*. Ed. by Vitrano, S. 2nd. Upper Saddle River, NJ: Prentice-Hall. See p. 20.

Ko, J. and T. W. Strganac (1998). "Stability and control of a structurally nonlinear aeroelastic system". In: *AIAA Journal of Guidance, Control*

and Dynamics Vol. 21, No. 5, pp. 718–725. DOI: 10.2514/2.4317. See pp. 48, 55, 81.

Ko, J., T. Strganac, and A. Kurdila (1999). "Adaptive feedback linearization for the control of a typical wing section with structural nonlinearity". In: *Nonlinear Dynamics* Vol. 18, No. 3, pp. 289–301. DOI: 10.1023/A:1008323629064. See p. 48.

Lee, K. W. and S. N. Singh (2007). "Global robust control of an aeroelastic system using output feedback". In: *AIAA Journal of Guidance, Control and Dynamics* Vol. 30, No. 1, pp. 271–275. DOI: 10.2514/1.22940. See pp. 50, 51.

— (2009). "Immersion- and invariance-based adaptive control of a nonlinear aeroelastic system". In: *AIAA Journal of Guidance, Control and Dynamics* Vol. 32, No. 4, pp. 1100–1110. DOI: 10.2514/1.42475. See p. 50.

Löfberg, J. (2004). "Yalmip: A toolbox for modeling and optimization in Matlab". In: *IEEE International Symposium on Computer Aided Control Systems Design*. Taipei, Taiwan, September 2–4. DOI: 10.1109/CACSD.2004.1393890. See pp. 43, 106, 117, 127.

Majumder, R., B. Chaudhuri, H. El-Zobaidi, B. Pal, and I. Jaimoukha (2005). "LMI approach to normalised $\mathcal{H}_\infty$ loop-shaping diesign of power system damping controllers". In: *IEE Proceedings - Generation Transmission and Distribution* Vol. 152, No. 6, pp. 952–960. DOI: 10.1049/ip-gtd:20045175. See p. 17.

Masubuchi, I., A. Ohara, and N. Suda (1998). "LMI-based controller synthesis: a unified formulation and solution". In: *International Journal of Robust and Nonlinear Control* Vol. 8, No. 8, pp. 669–686. DOI: 10.1002/(SICI)1099-1239(19980715)8:8<669::AID-RNC337>3.0.CO;2-W. See pp. 25, 41.

McEver, M. A., E. V. Ardelean, D. G. Cole, and R. L. Clark (2007). "Active control and closed-loop identification of flutter instability in typical section airfoil". In: *AIAA Journal of Guidance, Control and Dynamics* Vol. 30, No. 3, pp. 733–740. See p. 51.

Mukhopadhyay, V. (2000). "Transonic flutter suppression control law design and wind-tunnel results". In: *AIAA Journal of Guidance, Control and Dynamics* Vol. 23, No. 5, pp. 930–937. DOI: 10.2514/2.4635. See pp. 44, 47.

— (2003). "Historical perspective on analysis and control of aeroelastic responses". In: *AIAA Journal of Guidance, Control and Dynamics* Vol. 26, No. 5, pp. 673–684. DOI: 10.2514/2.5108. See pp. 1, 2, 35, 44, 46.

Olds, S. D. (1997). "Modeling and LQR control of a two-dimensional airfoil". MA thesis. Blacksburg, VA: Virginia Polytechnic Institute and State University. See pp. 68, 69.

O Neil, T. and T. W. Strganac (1998). "Aeroelastic response of a rigid wing supported by nonlinear springs". In: *AIAA Journal of Aircraft* Vol. 35, No. 4, pp. 616–622. DOI: 10.2514/2.2345. See pp. 45, 55.

Orsi, R., U. Helmke, and J. B. Moore (2006). "A Newton-like method for solving rank constrained linear matrix inequalities". In: *Automatica* Vol. 42, No. 11, pp. 1875–1882. See pp. 27, 43.

Özbay, H. and G. R. Bachmann (1994). "$\mathcal{H}_2/\mathcal{H}_\infty$ Controller design for a two-dimensional thin airfoil utter suppression". In: *AIAA Journal of Guidance, Control and Dynamics* Vol. 17, No. 4, pp. 722–728. See p. 46.

Pellanda, P. C., P. Apkarian, and H. D. Tuan (2002). "Missile autopilot design via a multi-channel LFT/LPV control method". In: *International Journal of Robust and Nonlinear Control* Vol. 12, pp. 1–20. DOI: 10.1002/rnc.612. See p. 137.

Pendleton, E. W., D. Bessette, P. B. Field, G. D. Miller, and K. E. Friffin (2000). "Active Aeroelastic Wing ight research program: technical program and model analytical development". In: *AIAA Journal of Aircraft* Vol. 37, No. 4, pp. 554–561. DOI: 10.2514/2.2654. See p. 2.

Platanitis, G. and T. W. Strganac (2004). "Control of a nonlinear wing section using leading- and trailing-edge surfaces". In: *AIAA Journal of Guidance, Control and Dynamics* Vol. 27, No. 1, pp. 52–58. DOI: 10.2514/1.9284. See pp. 45, 49, 50, 52, 55, 56, 63, 69, 73, 80, 82, 83, 88, 109.

— (2005). "Suppression of control reversal using leading- and trailing-edge control surfaces". In: *AIAA Journal of Guidance, Control and Dynamics* Vol. 28, No. 3, pp. 452–460. DOI: 10.2514/1.6692. See pp. 49, 55, 56, 80.

Prime, Z., B. Cazzolato, and C. Doolan (2008). "A mixed $\mathcal{H}_2/\mathcal{H}_\infty$ scheduling control scheme for a two degree-of-freedom aeroelastic system under varying airspeed and gust conditions". In: *AIAA Guidance, Navigation and Control Conference*. Honolulu, Hawaii, USA. 18–21 August. See pp. iii, 131, 137.

Prime, Z., B. Cazzolato, C. Doolan, and T. Strganac (2010). "Linear-parameter-varying control of an improved three-degree-of-freedom aeroelastic model". In: *AIAA Journal of Guidance, Control and Dynamics* Vol. 33, No. 2, pp. 615–619. DOI: 10.2514/1.45657. See pp. ii, 99.

Reddy, K. K., J. Chen, A. Behal, and P. Marzocca (2007). "Multi-input/multi-output adaptive output feedback control design for aeroelastic vibration suppression". In: *AIAA Journal of Guidance, Control and Dynamics* Vol. 30, No. 4, pp. 1040–1048. DOI: 10.2514/1.27684. See p. 50.

Rotea, M. A. (1993). "The generalized $\mathcal{H}_2$ control problem". In: *Automatica* Vol. 29, No. 2, pp. 373–385. See pp. 14, 116.

Safonov, M. G. and M. Athans (1977). "Gain and phase margin for multiloop LQG regulators". In: *IEEE Transactions on Automatic Control* Vol. 22, No. 2, pp. 173–179. See p. 107.

Scherer, C. W. (2001). "LPV control and full block multipliers". In: *Automatica* Vol. 37, No. 3, pp. 361–375. See pp. 42, 136.

Scherer, C., P. Gahinet, and M. Chilali (1997). "Multiobjective output-feedback control via LMI optimization". In: *IEEE Transactions on Automatic Control* Vol. 42, No. 7, pp. 896–911. DOI: 10.1109/9.599969. See pp. 24, 40, 101.

Scherer, C. W. (1996). "Mixed $\mathcal{H}_2/\mathcal{H}_\infty$ control for time-varying and linear parametrically-varying systems". In: *International Journal of Robust and Nonlinear Control* Vol. 6, No. 9, pp. 929–952. DOI: 10.1002/(SICI)1099-1239(199611)6:9/10<929::AID-RNC260>3.0.CO;2-9. See p. 40.

— (2000). "Robust mixed control and linear parameter-varying control with full block scalings". In: *Advances in linear matrix inequality methods in control*. Ed. by El Ghaoui, L. and Niculescu, S.-I. University City Science Center, PA: Society for Industrial and Applied Mathematics. Chap. 10, pp. 187–208. See pp. 25–27, 42, 136, 139–141.

Scherer, C. and S. Weiland (2004). "Linear matrix inequalities in control". URL: http://www.cs.ele.tue.nl/sweiland/lmi.html (visited on July 17, 2007). See pp. 21, 22, 25, 30, 31, 125, 137, 139.

Sheta, E. F., V. J. Harrand, D. E. Thompson, and T. W. Strganac (2002). "Computational and experimental investigation of limit cycle oscillations of nonlinear aeroelastic systems". In: *AIAA Journal of Aircraft* Vol. 39, No. 1, pp. 133–141. DOI: 10.2514/2.2907. See pp. 45, 55.

Silva, S. da and V. L. Júnior (2006). "Active flutter supression in a 2-D airfoil using linear matrix inequalities techniques". In: *Journal of the Brazilian Society of Mechanical Sciences & Engineering* Vol. 28, No. 1, pp. 84–93. DOI: 10.1590/S1678-58782006000100009. See pp. 52, 68, 69.

Singh, S. N. and M. Brenner (2003*a*). "Limit cycle oscillation and orbital stability in aeroelastic systems with torsional nonlinearity". In: *Nonlinear Dynamics* Vol. 31, No. 4, pp. 435–450. DOI: 10.1023/A: 1023264319167. See p. 45.

— (2003*b*). "Modular adaptive control of a nonlinear aeroelastic system". In: *AIAA Journal of Guidance, Control and Dynamics* Vol. 26, No. 3, pp. 443–451. DOI: 10.2514/2.5082. See p. 50.

Singh, S. N. and L. Wang (2002). "Output feedback form and adaptive stabilisation of a nonlinear aeroelastic system". In: *AIAA Journal of Guidance, Control and Dynamics* Vol. 25, No. 4, pp. 725–732. DOI: 10.2514/2.4939. See p. 50.

Singh, S. N. and W. Yim (2003). "State feedback control of an aeroelastic system with structural nonlinearity". In: *Aerospace Science and Technology* Vol. 7, No. 1, pp. 23–31. DOI: 10.1016/S1270-9638(02)00004-4. See p. 50.

Skogestad, S. and I. Postlethwaite (2005). *Multivariable Feedback Control: Analysis and Design*. 2nd. Hoboken, NJ: John Wiley & Sons. See pp. 10, 15, 16, 39, 107, 142.

Souza, C. E. de, A. Trofino, and J. de Oliveira (2003). "Parametric Lyapunov function approach to $\mathcal{H}_2$ analysis and control of linear parameter-dependent systems". In: *IEE Proceedings Control Theory & Applications*. DOI: 10.1049/ip-cta:20030709. See p. 100.

Strganac, T. W., J. Ko, and D. E. Thompson (2000). "Identification and control of limit cycle oscillations in aeroelastic systems". In: *AIAA Journal of Guidance, Control and Dynamics* Vol. 23, No. 6, pp. 1127–1133. DOI: 10.2514/2.4664. See pp. 45, 48, 49, 55, 63, 69, 73, 80, 81.

Sturm, J. (1999). "Using SeDuMi 1.02, a Matlab toolbox for optimization over symmetric cones". In: *Optimization Methods and Software* Vol. 11–12. Version 1.05 available from `http://fewcal.kub.nl/sturm`, pp. 625–653. DOI: 10.1080/10556789908805766. See p. 43.

Symon, K. (1960). *Mechanics*. 2nd. MA: Addison-Wesley. See p. 65.

Tadi, M (2003). "State-dependent Riccati equation for control of aeroelastic utter". In: *AIAA Journal of Guidance, Control and Dynamics* Vol. 26, No. 6, pp. 914–917. DOI: 10.2514/2.6918. See p. 50.

Taylor, N. V., A. L. Gaitonde, D. P. Jones, and C. B. Allen (2007). "Modeling the benchmark active controls wing through linear and computational aeroelastic analyses". In: *AIAA Journal of Aircraft* Vol. 44, No. 4, pp. 1383–1388. DOI: 10.2514/1.22959. See p. 44.

Theodorsen, T. (1934). *General theory of aerodynamic instability and the mechanism of utter*. Tech. rep. Report No. 496. NACA. See p. 43.

Theodorsen, T. and I. Garrick (1940). *Mechanism of utter: a theoretical and experimental investigation of the utter problem*. Tech. rep. Report No. 685. NACA. See p. 43.

— (1941). *Flutter calculations in three degrees of freedom*. Tech. rep. Report No. 741. NACA. See p. 43.

Toh, K. C., M. J. Todd, and R. H. Tutuncu (1999). "SDPT3—a Matlab software package for semidefinite programming". In: *Optimization Methods and Software* Vol. 11, pp. 545–581. DOI: 10.1080/10556789908 805762. See pp. 43, 106, 117, 127.

VanAntwerp, J. G. and R. D. Braatz (2000). "A tutorial on linear and bilinear matrix inequalities". In: *Journal of Process Control* Vol. 10, No. 4, pp. 363–385. DOI: 10.1016/S0959-1524(99)00056-6. See pp. 19, 20, 42.

Vepa, R. (2007). "Active utter suppression by feedback compensation of transport lags". In: *AIAA Journal of Guidance, Control and Dynamics* Vol. 30, No. 3, pp. 879–881. See pp. 52, 77.

Wang, J. and D. A. Wilson (2001). "Mixed $\mathcal{GL}_2/\mathcal{H}_2/\mathcal{GH}_2$ control with pole placement and its application to vehicle suspension systems". In: *International Journal of Control* Vol. 74, No. 13, pp. 1353–1369. DOI: 10.1080/00207170110070554. See pp. 24, 116.

Waszak, M. (1996). "Modeling the benchmark active control technology wind-tunnel model for application to utter suppression". In: *AIAA Atmospheric Flight Mechanics Conference*. also AIAA Paper 96-3437. San Diego, CA, July 29–31. See p. 44.

Waszak, M. R. (2001). "Robust multivariable utter suppression for benchmark active control technology wind-tunnel model". In: *AIAA Journal of Guidance, Control and Dynamics* Vol. 24, No. 1, pp. 147–153. DOI: 10.2514/2.4694. See p. 47.

Wilson, D. A. (1995). "Induced norms for mixed $\mathcal{H}_2/\mathcal{H}_\infty$ and $\mathcal{H}_2/\mathcal{H}_\infty/\mathcal{L}_\infty$ control". In: *Conference of Decision & Control*, pp. 3164–3169. DOI: 10.1109/CDC.1995.478634. See p. 116.

Xie, W (2005). "$\mathcal{H}_2$ gain scheduled state feedback for LPV system with new LMI formulation". In: *IEE Proceedings Control Theory & Applications* Vol. 152, No. 6, pp. 693–697. DOI: 10.1049/ip-cta:20050052. See p. 101.

Xing, W. and S. N. Singh (2000). "Adaptive output feedback control of a nonlinear aeroelastic structure". In: *AIAA Journal of Guidance, Control and Dynamics* Vol. 23, No. 6, pp. 1109–1116. DOI: 10.2514/2.4662. See pp. 49, 50.

Zhou, K., J. C. Doyle, and K. Glover (1996). *Robust and optimal control*. Upper Saddle River, NJ: Prentice Hall. See pp. 10–16, 39, 100.